PARTICLE AGGLOMERATED 3-D NANOSTRUCTURES

FOR PHOTON ABSORPTION

by

Mugunthan Sivayoganathan, B.Sc.Eng., M.Eng.

University of Peradeniya, Sri Lanka, 2001

University of Moratuwa, Sri Lanka, 2007

A dissertation presented to Ryerson University

in partial fulfilment of the requirement for the degree of

Doctor of Philosophy in the Program of

Aerospace Engineering

Toronto, Ontario, Canada, 2013

Author's Declaration

I hereby declare that I am the sole author of this dissertation. This is a true copy of the dissertation, including any required final revisions as accepted by my examiners.

I authorize Ryerson University to lend this dissertation to other institutions or individuals for the purpose of scholarly research.

I further authorize Ryerson University to reproduce this dissertation by photocopying or by other means, in total or in part, at the request of other institutions or individuals for the purpose of scholarly research.

I understand that my dissertation may be made electronically available to the public.

Signature

Abstract

Particle agglomerated 3-D nanostructures for photon absorption

Doctor of Philosophy, 2013

Mugunthan Sivayoganathan

Aerospace Engineering

Ryerson University

The main objective of this thesis is to investigate the photon absorption properties of particle agglomerated 3-D structures that are synthesized through femtosecond laser ablation of solids. The size and morphology of these particle agglomerated 3-D structures, which can be tailored through adjusting laser parameters, determine the photon absorption property.

A systematic theoretical and experimental study was performed to identify the effect of lasers on the size of the formed particles. The literature survey showed that the amount of supersaturation influences the growth rate as well as the nucleation rate of vapour condensed nanoparticles. Based on this theory, a mechanism was formed to explain the control of laser parameters over the size of formed particles. Further, a theoretical explanation was proposed from the experimental results for the transition of particle size distribution modals. These proposed mechanisms and explanations show the variation in particle size in the particle agglomerated 3-D nanostructures with laser parameters.

The effect of laser parameters on the formed ring size was studied. Based on the previous studies, a mechanism was proposed for the formation of ring nanoclusters. The laser pulse intensity dependent ponderomotive force was the key force to define the formation of ring nanoclusters. Then the effect of laser parameters on ring size was studied. Structures fabricated on several materials such as graphite, aluminosilicate ceramic, zinc ingot, gold, and titanium were analyzed to show the influence of material properties, laser parameters, and the environmental conditions on the size of ring formed.

The studies performed on the structures showed a minimum absorption of 0.75 A.U. in the bandwidth from UV to IR. The absorption spectrum is much wider compared to existing nanomaterials, such as silicon nanostructures and titanium dioxide nanostructures. To the best of the author's knowledge, it is a very competitive absorption rate when compared with the previous nanostructures used in photovoltaic conversion. Several features of nanostructures contribute to the enhancement of this light absorption. The special feature of the structure is that ease to fabricate and modify the properties by varying the laser parameters could make it competitive among other nanostructures available for solar cells.

Acknowledgements

My deepest gratitude is to my advisors, Dr. Bo Tan and Dr. Krishnan Venkatakrishnan. I have been amazingly fortunate to have advisors who gave me full freedom to explore on my own, and at the same time offering guidance to recover from my missteps. A special thanks to Dr. Bo Tan, who taught me how to question my thoughts and express ideas. Her mentoring and guidance helped me to become a disciplined researcher. I would like to thank my advisor Dr. Krishnan Venkatakrishan, for being a great motivator and friend. Over the years I have come to admire his humility, sense of humour, and generosity. He inspired me with his innovative ideas and encouragement.

I thank my loving parents, whose intentions have always been for my happiness and fulfillment in life. Their sacrifices are unmatched. I also thank my father-in-law and mother-in-law for their kind assistance during the course of my study.

Most importantly, none of this would have been possible without the love, patience and inspiration from my family: my wife and kids. I would like to express my heart-felt gratitude to my family. My wife, Komathy shared all the stress and tension with me at difficult stages throughout this endeavor. She showed utmost patience at times when frustrations gripped me. I am indebted to her for her support and continuous encouragement. I would also thank my kids, Vaamanan and Yaathavan for giving me relaxing interludes during my tough times.

I am grateful to my committee members Dr. Jason Lassaline, Dr. Jeffrey Yokota, Dr. Fengfeng (Jeff) Xi, Dr. Hua Lu from Ryerson university, and Dr. Sivakumar Narayanswamy from Concordia university for their advices to improve my thesis. I would like to thank to Dr. Jason Lassaline, for his encouraging words and caring advices since I have started my studies in Ryerson University.

I would like to thank my colleagues and friends from the "Laser micro/nano fabrication laboratory" (Ryerson University) for their continuous encouragements. A special thanks for my friend Dr. Balasubramaneyam Maniymaran of Amazon Canada Fulfillment for his assistance and informative discussions.

At last but not least, I would like to remember Dr. M. A. R. V. Fernando and the late Dr. G. K. Watugala of Department of Mechanical Engineering, University of Moratuwa, for their kind support and guidance at the beginning of my studies. Though Dr. G. K. Watugala is no longer with us, his thoughts will remain forever.

Finally, I would like to thank The God Almighty for all the success in my efforts.

Dedication

To my parents, for sowing the seeds of my education, for guiding me through the hard times of my early life, and for showing me the path of spirituality.

To my wife, for paving my success through her sacrifices, kindness, and nurturing.

And to The God I see in the magnificence of Mother Nature.

Table of Contents

List of Tables

List of Figures

Chapter 1 Introduction

Nanostructures have been extensively used in third generation solar cells to enhance the photon absorption. Several semiconductors and metals are used in the synthesis of nanostructures for the development of new generation solar cells. Silicon and titanium are extensively used in those structures. Other materials include zinc (Zn), gold (Au), cadmium selenide (CdSe) alloys, gallium arsenide (GaAs) alloys, aluminum (Al), and silver (Ag) [1–14].

Silicon nanostructures improve photon absorption efficiency in the visible wavelength, whereas titanium nanostructures significantly enhance absorptance in the UV range. This chapter provides a survey of these nanostructures. The description focuses on morphology, the characteristics of photon absorption, as well as the fabrication methods used to create those nanostructures. Finally, the motivation of this research thesis and the research objectives will be discussed.

1.1 Silicon nanostructures for enhanced absorption efficiency

Silicon has been extensively used in the manufacture of solar cells [15–20]. The solar cells made of crystalline silicon (single crystal and poly-crystal) are the first generation cells. They have conversion efficiency in the range of 25%–29%. The second generation cells are made out of amorphous silicon films and have conversion efficiency around 10%. The third generation cells adopt nanometre structures and conversion efficiency reaches 10%–16%) [21]. The conversion efficiency is the percentage of solar energy converted into electrical energy. Although the second and third generation cells cannot compete with the first generation ones in terms of efficiency at the moment, they have attracted research interest because they can be mass-produced at a much lower cost.

Silicon solar cells typically operate in the wavelength range of 400 to 1100 nm. Silicon nanostructures of various morphologies such as nanotubes, nanowires, nanofunnels, nanoholes, nanowells, nanocones, and nanorods have been synthesized [22–30]. Most of these nanostructures are used to prototype dye sensitive solar cells. The unique optical properties of these nanostructures increase photon absorption and light trapping, therefore, harvest light more effectively. Furthermore, the architecture of these nanostructures promotes electron transport and electron collection, which leads to better conversion efficiency. Thus, they promise solar cells of better performance. The following few sections present a literature survey of several types of silicon nanostructures.

1.1.1 Silicon nanowire

Silicon nanowire is the most researched silicon-based nanostructures for solar cell application. Vapour depositions is the most commonly used method for the production of silicon nanowires. Benedict O'Donnell grew silicon nanowires by vapour deposition, followed by a catalytic treatment of Sn droplets [24]. Figure 1.1 shows the fabricated nanowire arrays and their absorption spectrum.

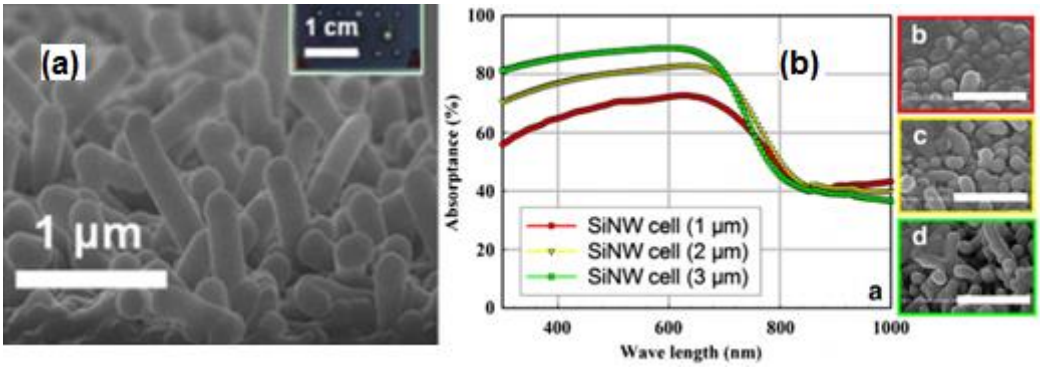

Figure 1.1: (a) Nanowire (b) Absorption curve for varying length [24]

The vapor condensation method generates randomly orientated silicon nanowires. Jia Zhu et al. proposed sphere lithography to fabricate orderly aligned silicon nanowire forest. First, hot wire chemical vapor deposition (HWCVD) was used to grow a thick (1 µm) Si:H film on an indium-tin-oxide coated glass substrate. Then the Langmuir-Blodgett method [23] was used to assemble silica nanoparticles (NPs) into a close-packed monolayer on the top of the Si-H thin film. The sample then went through a chlorine-based reactive ion etching (RIE). Those silica nanoparticles functioned as etch-masks. Depending on the etching conditions and etching rates, Si-H nanowires or Si-H nanocones could be fabricated [23].

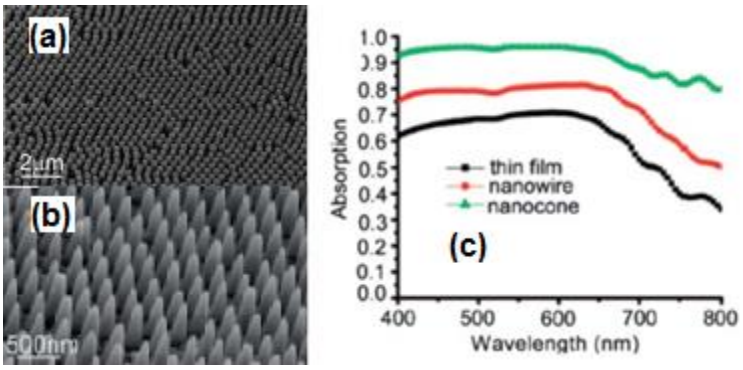

Figure 1.2: (a) Silicon nanowire (b) Silicon cone (c) Absorption curves [23]

Figure 1.2 shows the nanowire array and their photon absorption (refer absorptance) spectrum. Generally, compared to randomly orientated nanowires, nanowire array demonstrated higher absorption efficiency. This could be due to an increase in interaction of light rays with organized array structures. Studies show that the length of the nanowire determines the absorption efficiency. An increase in the length of nanowire increases the amount of photon trapping, thus, higher absorption efficiency [24]. The typical length of silicon nanowires is in the range of 2 - 3 μm [24].

1.1.2 Silicon nanocone

The above described sphere lithography method was also used to fabricate silicon nanocone arrays [23] (shown in Figure 1.2(b)). Figure 1.3 shows a model of nanocones and the photon absorption spectrum obtained by simulation studies. Their photon absorption properties could be enhanced in the future by the deposition of an anti-reflection coating [31].

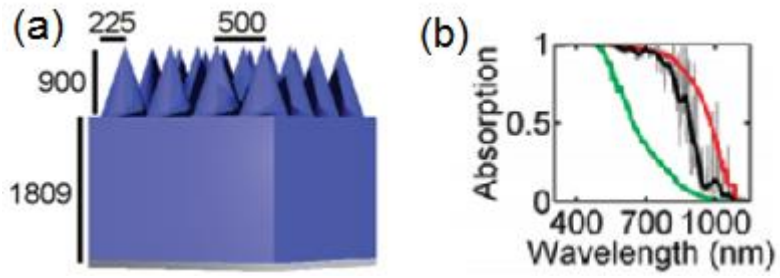

Figure 1.3: (a) nanocones (b) absorption properties [31]

Compared to silicon nanowires, silicon nanocone arrays showed much higher absorption efficiency (refer absorptance) in the wavelength range of 400 and 650 nm (nanocone 93%, nanowires 75% and thin film 64% [23] in Figure 1.2). The conical surface of nanocones has an added advantage. Along the outer line of the nanocone, absorption efficiency increases through secondary absorption of scattered light. The significant advantage of nanocones is that they broadened the absorption spectrum of silicon [31].

1.1.3 Silicon nanopyramids

Anastassios Mavrokefalos et al. used standard scalable micro fabrication techniques to create inverted nanopyramids, as shown in Figure 1.4 [32]. The fabrication began with a silicon-on-insulator wafer with the desired Si and SiO2 thicknesses. Then, interference lithography was used to create arrays of holes on the Si-SiO2 layer. Finally, wet etching was carried out to produce inverted nanopyramid arrays [32].

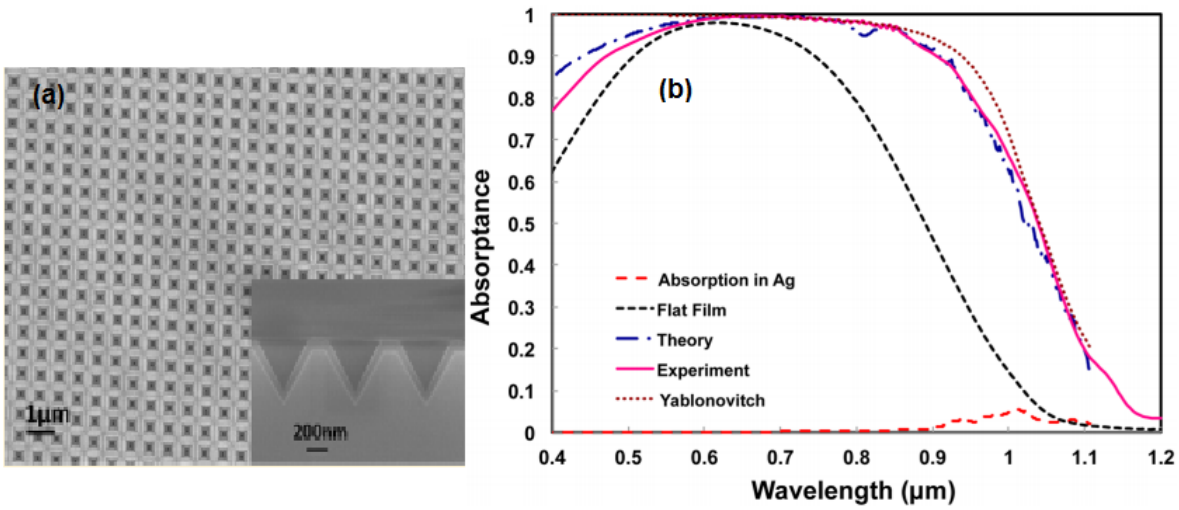

Figure 1.4: (a) Nanopyramids (b) Absorption curve [32]

The final product is a silicon substrate with arrays of craters that the bottoms are in the shape of a pyramid. An experimental study showed that inverted nanopyramids of less than 10 μm depth can absorb as well as 300m thick flat crystalline silicon substrates [32]. Further, experimental and simulation studies performed on nanopyramids showed an expansion in the absorption spectrum, compared to crystalline silicon [32], [33] .

1.2 Titanium oxide nanostructures

Today, roughly 90% of the photovoltaic market is dominated by single-junction solar cells constructed with silicon wafers. The drawbacks of these cells are the cost of silicon and the difficulties in the manufacturing processes. The invention of a new type of solar cell called Dye Sensitive Solar Cell (DSSC) has started to play an important role in photovoltaic applications. These cells are made with low-cost materials and formed on top of flexible sheets.

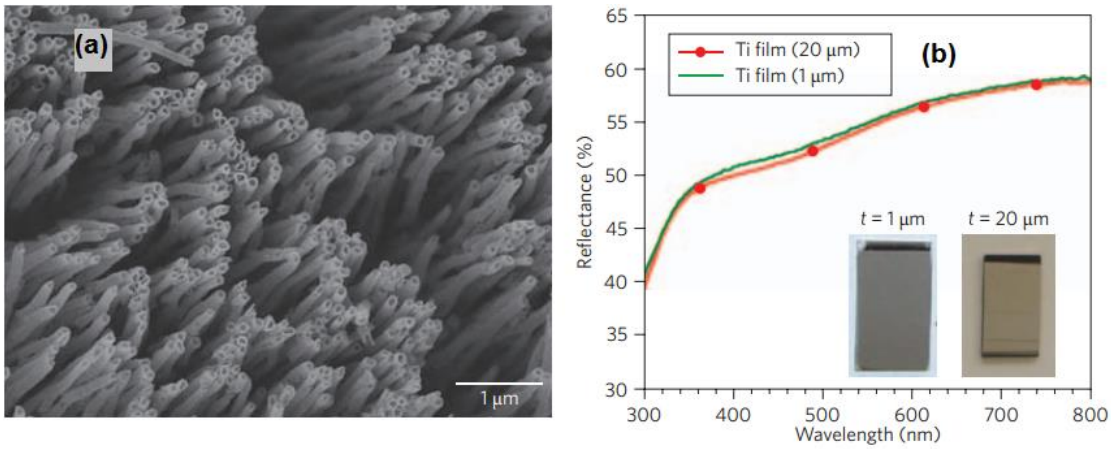

Figure 1.5: (a) Nanotubes, (b) absorption property [34]

Nanostructures of titanium oxides have been extensively used in DSSCs, therefore it is also called as nano solar cells. The absorption property of titanium oxide nanostructures is determined by its phases, which can be controlled through thermal treatment. Further, Titanium oxides can be formed into nanostructures with different morphologies, which also varies their absorption properties [35].

Among all titanium oxide nanostructures that have been investigated for the purpose of photon absorption, nanotube is the most studied. Several studies have been performed on the synthesis of titanium oxide nanotubes and their optical properties were characterized [34], [35]. Figure 1.5 shows an example of the titanium oxide nanotubes fabricated by Oomman et al. [34] and their reflectance spectrum. Titanium oxide nanotubes show a decrease in absorptance with an increase in visible wavelength range.

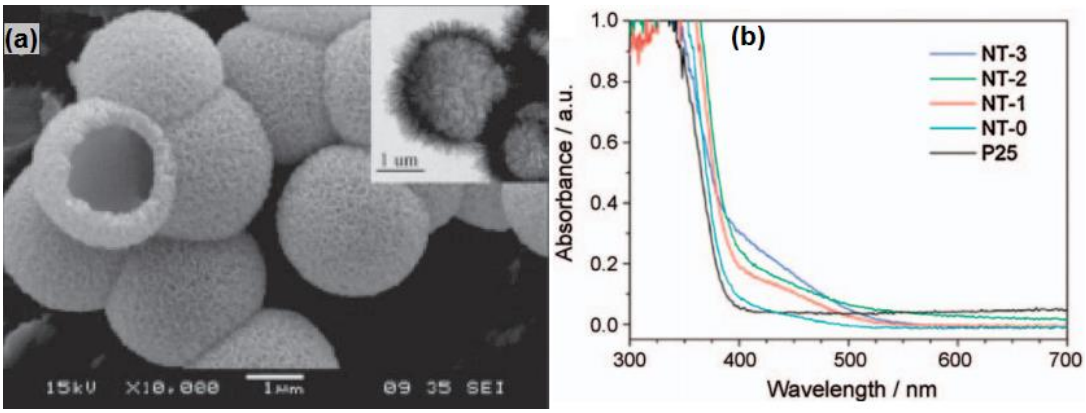

Figure 1.6: (a) Mesoporous titanium oxide spheres, (b) Absorption curve [36]

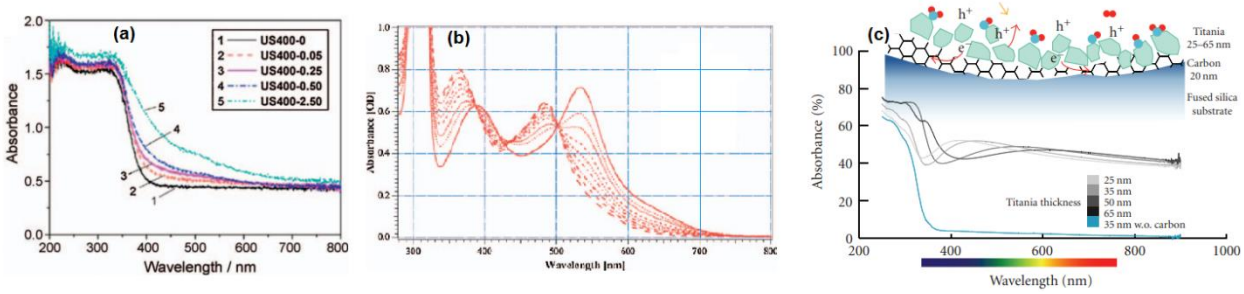

Figure 1.7: Absorption curves for (a) doped TiO_2 powders, (b) mesoporous TiO_2 film, (c) titanium oxide particles [36], [37]

Other than nanotubes, mesoporous titanium oxide spheres, TiO_2 powders, mesoporous TiO_2 film, and titanium oxide particles have been studied for photovoltaic applications [36], [37]. Figure 1.6 - 1.7 give examples of absorption spectrum of such titanium oxide nanostructures. Compared to other nanostructures, these structures do not have advantage in visible wavelength range. But, they demonstrated a sharp increase in UV range. This character can be used to expand the bandwidth of absorption spectrum of a solar cell.

1.3 Nanostructures made of other materials

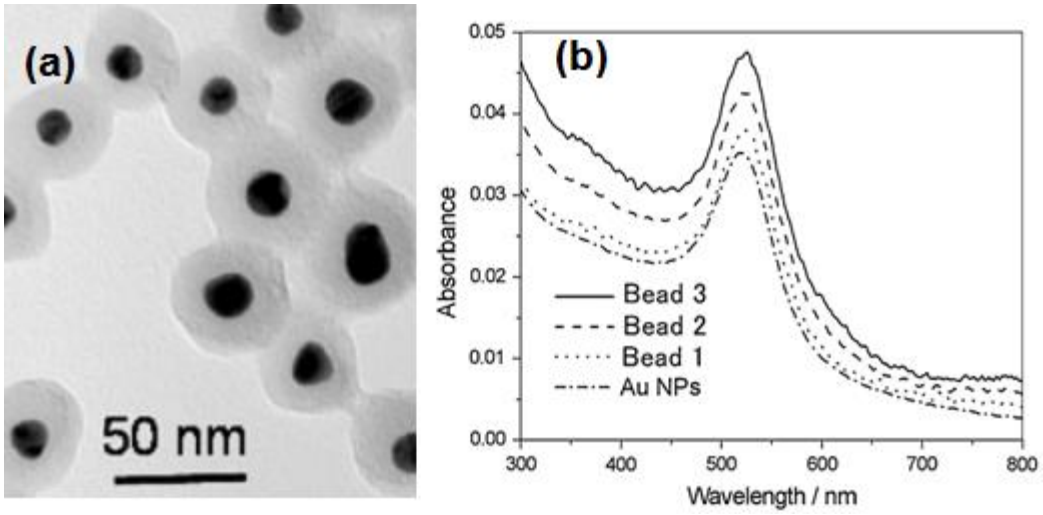

Figure 1.8: (a) SiO2 coated Au NP (b) Absorbance spectra of Au NPs and SiO2 - coated Au NP [1]

Other than silicon and titanium oxide nanostructures, nanostructures of other material were also researched either to increase the absorbance efficiency or to extend the bandwidth of absorbance spectrum. Examples include metal nanoshells (GaAs, Ag, Au/SiO2) on different substrates, SiO_2-doped gold nanoparticles (Figure 1.8), supramolecular dye nanotubes, metal sulfide nanotips (Figure 1.9), 3-D nanospike arrays, Au–CdSe nanorods, and dendritic and hierarchically branched nanostructures (Figure 1.10) [1, 2, 21–23].

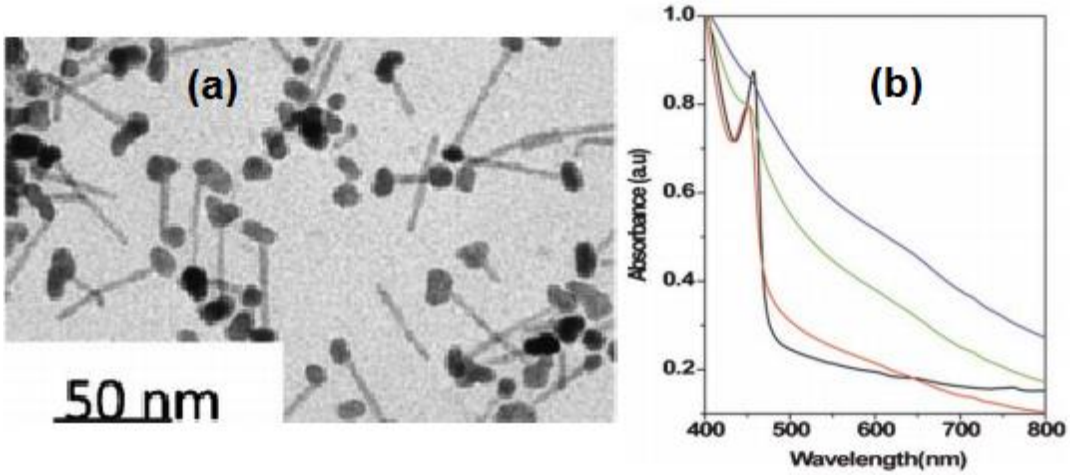

Figure 1.9: (a) TEM images of CdS with PbS tip (b) absorption spectra of three sizes of PbS-CdS (black line), 10 nm (red line), 12 nm (green line) and 17 nm (blue line) [39]

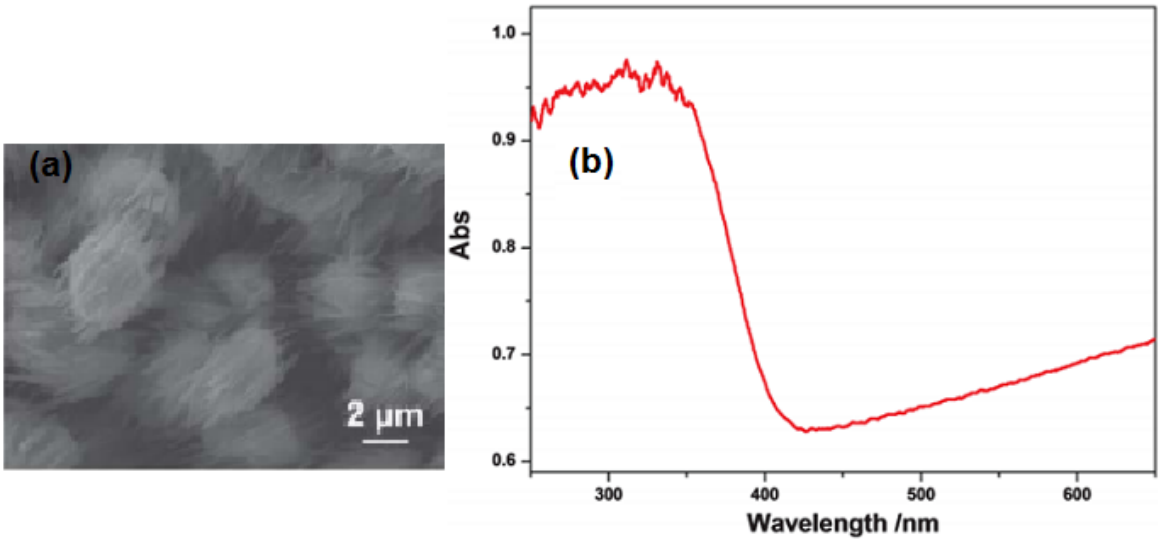

Figure 1.10: (a) Hierarchically branched MoO3 nanostructures (b) Absorption spectrum [38]

These examples show that the light absorption property of metal nanostructures is highly depend on spectrum of light. They produced strong absorption in UV range and weak absorption in the visible range.

1.4 Remarks on literature survey

The previous survey reveals that the bandwidth of photon absorption of existing nanostructures is limited to either UV or visual spectrum. Silicon nanostructures improve the photon absorptance in the visible wavelength range. Nanostructures of other materials including titanium nanostructures do not significantly improve absorptance in the visible spectrum, but expand the absorption spectrum to UV range. None of these structures demonstrated strong absorption in IR range.

1.5 Research Motivation and Objectives

The Laser Micro Nano Fabrication Laboratory at Ryerson University demonstrated that 3-D nanoparticle network can be fabricated by a MHz frequency ultrafast laser ablation of solids. The 3-D nanoparticles network consists of many rings that interconnected by nanoparticles chains. These nanostructures can be generated from almost all kinds of targets such as metals, alloys, semiconductors, ceramics, glasses and polymer resin [41–44]. The silicon 3-D nanoparticle network showed strong absorptance upon illumination [45]. A prototype nano solar cell fabricated by colleagues using the same nanostructure reported a cell efficiency of 12% [46]. These previous research results indicated the potentials of using the 3-D nanoparticle networks for light harvest.

The nanoparicle network has two main elements: particles and rings. Prior study indicates that vapour condensation is the main mechanism of particle formation [47]. However, there is no understanding on the mechanism of ring structure formation and the influence of laser

parameters on the ring size and particle diameter. This knowledge can be used to optimize the morphology of the 3-D nanoparticles networks, which may lead to the increase in photon absorptance. Hence, this research aims to identify the structure formation mechanism and to apply the findings to increase the efficiency of light absorptance. The main objectives of this research are given below.

- Theoretical and experimental analysis of particle forming mechanism and the identification of relationship between particle sizes with laser parameters through fundamental analysis of plume properties.
- Understand the ring formation mechanism. Identify laser parameters and process parameters that alter ring size.
- Find the relation between photon absorptance efficiency and the morphologies of the particle-agglomerated 3-D nanostructures.

Chapter 2 Literature survey on laser ablative particle synthesis

The morphology of the nanostructures determines their properties, thus, performance in potential applications. This chapter explains the mechanisms that are involved in the formation of particles by femtosecond laser ablation of solid targets. The relevant knowledge shall be used to identify the mechanisms involved in the generation of particle-agglomerated 3-D nanostructures; hence providing guidelines in tailoring their morphologies.

The extreme short duration of femtosecond laser pulses drastically reduces heat loss due to conduction. Therefore, material is heated to a very high temperature rapidly. This characteristic of the femtosecond laser enables it to heat any material to a high-density plasma state with temperature and pressure above the critical point [48] . The high-density plasma is favorable for the synthesis of fine particles, especially nanoscale particles. In fact, femtosecond lasers have been used in low-volume synthesis of nanostructures of different morphologies for research purposes [24, 25, 34–36].

Many studies were performed on particle forming mechanisms. There are many publications dedicated to in-depth analysis of particle size and particle structure [54–56]. These studies have shown that many forming mechanisms could be involved during pulsed laser ablation, including vapour condensation, sputtering, spallation, phase explosion, and solid exfoliation. The particle size produced from the above given mechanisms vary from nanometer to micrometer. In actual laser ablation, several mechanisms could be involved simultaneously. In addition, a few secondary mechanisms are responsible for the growth of particles, such as coalescence and fragmentation. Laser parameters such as fluence, repetition rate, wavelength, and pulse duration determine the particle size and the size distribution.

2.1 Vapour condensation

During vapour condensation, particles are formed from the vapour plume species. Studies have shown that this process takes place in nanoseconds. This time is much shorter than the plume formation time (in 10^{-7}seconds) [57]. The time difference between the plume existence and the particle formation ensures vapour-particle transformation.

The vapour phase of material can be formed through two routes. Normally an intermediate transient liquid phase is present during phase transformation, but this is not always true. There could be a possibility of direct vapour formation during pulsed laser ablation (i.e. solid material directly transforms into vapour phase without an intermediate liquid phase), which is called direct vapourization. It occurs (without spallation and forms vapour plume) when laser fluence exceeds the evaporation threshold. The chances of melt ejection are rare during direct evaporation.

There are 4 stages involved in vapour condensation: cluster nucleation, growth, cooling, and deposition. The species within a vapour plasma collide with the ambient gas molecules frequently. The collisions lead to aggregation of tens to thousands of atoms or molecules, forming nanoclusters. The formation of nanoclusters is governed by the plume expansion dynamics.

Nanoclusters grow into nuclei by continuously colliding with species within an ablated vapour. Cluster nucleation occurs when barrier energy due to surface tension is overcome by the surface energy. Formation of the nucleus or stable cluster is governed by the temperature and the concentration of the nucleating species (atoms, molecules, ions, and clusters), as well as the properties of the ablated material [58] . The stable clusters further grow and form nanoparticles. The size of nuclei and their consequent growth determine the size of the final nanoparticles. Therefore, the starting point of nucleation and the plume existence time are of great importance [59], [60].

The newly formed nanoparticles grow continuously by agglomeration. The growth of nanoparticles continues until nanoparticles cool down and reach melting point. The cooling process is governed by the ambient gas conditions.

The laser-material interaction involves highly dynamic, nonlinear plume expansion, condensation, and nucleation processes. For example, the expansion velocity of a plume produced by an intensity of 10^9 W/cm^2 would easily reach 10^7 cm/s, with more than 1 keV directed kinetic energy [61]. The laser parameters and the properties of material being ablated determine the plume properties, as well as the size of fabricated nanoclusters / structures. Studies have shown that laser fluence, wavelength, repetition rate, and pulse duration played critical roles in controlling the size of the nanoclusters [62]. Pinon et al. performed optical emission

studies on femtosecond laser ablated plume. They showed that the plasma temperature increased with the increasing laser fluence until it reached saturation. The intensity of the species ejected also increased with laser fluence [63]. In another study, Eliezer et al. showed an increase in plume species temperature with increasing laser irradiance [56].

Studies have shown that the particles formed by vapour condensation are much smaller than 100 nanometres. Presence of coalescence during vapour condensation may result in the formation of micro-sized particles. Particles greater than 100 nm are normally generated by mechanisms other than vapour condensation [57]. If long pulses (e.g. nanosecond pulses) are used for ablation, the particles produced by vaporization may account for a small portion of the total mass removal when compared to other mechanisms. The advantage of using femtosecond laser ablation is that the majority of heated material can be converted into vapor instantly. Most of the particles formed by femtosecond laser ablation grow from vapour. This guarantees that the synthesized particles are in nanoscale.

2.2 Solid exfoliation

Solid exfoliation is the removal of material in solid state due to laser induced stresses. These stresses increase with a decrease in the pulse duration or an increase in the pulse intensity. A previous study shows possible occurrence of solid exfoliation in brittle or refractory materials, e.g. ceramics [64]. The expelled particles are in irregular shapes. The irregular fractured morphology is characteristics to this mechanism.

2.3 Hydrodynamic sputtering

Hydrodynamic sputtering is a liquid ejection mechanism that occurs to pulsed laser ablation of solids. The cyclic heating and cooling of the laser ablated surface results a pool of melted material on the top surface. This liquid pool ejects fine liquid droplets. The spherical morphology of the ejected particles, which is caused by the surface tension, confirms their initial form of liquid phase. Transient melting and motion of melt liquid by steep thermal gradients and the relaxation of the laser-induced pressure lead to the ejection of large droplets. The occurrence of this mechanism could be identified from the size and the shape of the particles formed. Studies have shown that the size of the particles formed is in the range of 100-200 nm [57] . The size of the formed particles depends on density, surface tension, and the thermal coefficient of the ablated material. The particles formed by this mechanism are smaller compared with those formed by spallation and phase explosion.

The hydrodynamic sputtering shows a similar mechanism to exfoliation where instead of liquid, solid is ejected. The hydrodynamic sputtering due to cyclic heating and cooling of laser ablated surface cannot be used to explain particles bigger than 200 nm. A different mechanism, called spallation, which takes place inside the melt pool could be used to explain the formation of micron-sized spherical particles.

2.4 Spallation

Pulsed laser irradiation of solid induces rapid thermal expansion of ablated material. The impact or stresses caused by the rapid expansion generate fragments. Spallation is the process of

ejection of these fragments. It occurs when the laser fluence falls between the ablation threshold and evaporation threshold of the material.

The mechanism for the formation of spallation is as follows. Fast energy deposition by short pulse laser leads to a sharp temperature rise and the development of strong compressive-thermoelastic stresses in the target material. These stresses generate tensile stresses, which form voids in the melted zone. The evolution of voids occurs in two stages: (a) nucleation and growth and (b) coarsening and coalescence. The number of voids and their sizes increase during nucleation and growth, while small voids combine into large voids during coalescence. The eventual percolation of voids through the melt leads to ejection of liquid layers of approximately 25 nm thickness and large droplets from irradiated spot [65].

In contrast to nanoscale particles formed by vapour condensation, the clusters formed by melt ejections are in the range of 0.1 to 10 μm. Since the fragments are ejected directly from the surface of the solid, ambient gas pressure does not affect the fabricated particle size [62]. The formed particles are in a spherical shape.

Vapour condensation account for very small portion of the mass removal during laser ablation. However, spallation account for most of the mass removed from target material during ablation.

2.5 Phase explosion

As spallation, phase explosion or explosive boiling also causes a large amount of material removal. A steep increase of the ablation rate at high irradiance is the evidence of the occurrence of phase explosion. The threshold irradiance for the phase explosion showed a dependence to laser spot size and the wavelength. A laser with larger beam size and longer incident wavelength

needs higher laser irradiance for the occurrence of phase explosion. A study showed phase explosion occurred on silicon for an irradiance greater than 10^{10} W/cm^2 [66].

Laser pulses of high fluency (much higher than ablation threshold) create a crater on the ablated surface. The super-heated liquid formed on top of the surface is transformed into a mixture of vapour and liquid droplets. Due to the high pressure and temperature of the plume, liquid melt is pushed from center of the target spot and forms a raised rim around the crater, similar to a volcano crater. When the pressure is sufficiently large, the resulting momentum surpasses the surface tension and ejects droplets around the rim. These particles are usually several microns in diameter and are reported to be formed by the back coil or recoil pressure.

A study performed by Kelly and Miotello [67–69] with different heating sources claimed that explosive boiling is the most efficient mechanism for material removal in nanosecond pulse duration, but produced a poor quality of the ablated area. These mechanisms have been used to synthesize micron sized glass fibers, which have great potentials in photo optics.

2.6 Coulomb Explosion

All previously discussed mechanisms regards laser as a high intense heat source, these mechanisms are thermal processes. The Coulomb explosion is quite different. It is an electrostatic effect induced by laser-matter interaction. The laser irradiation of surface leads to the emission of electrons, which leaves positive holes on the surface. At high laser intensities, a huge number of electrons emits from the surface and generates the same amount of positive holes on the surface. Accumulation of positive holes leads to an unstable state of material electrostatically. At one stage, materials fracture and emit positive ions and clusters from the surface. This electrostatic repulsion is called a Coulomb explosion. A possible occurrence of this

electrostatic repulsion could be prevented by the return of the emitted electrons to fill the positive gaps. For some materials, especially dielectrics and semiconductors, this filling time is in picoseconds, which is enough for the repulsion to take place. The emitted species travel in the direction of the residual field [70], [71].

2.7 Other particle forming mechanisms

There are mechanisms involved in laser ablation that will not generate particles but may alter the particle size distribution and the number of particles formed. These processes can occur from several nanoseconds to several milliseconds after the laser pulse. There are three main mechanisms: coagulation, fragmentation, and agglomeration.

Particles formed during ablation collide with each other and coalesce to form new large particles. This process is called coagulation. It takes place if the momentum of the particles formed is high enough or the particles formed are in liquid state. Coagulation normally occurs in the later stages of particle formation.

The charging of particles through photoelectron emission and consequent explosive breaking up due to accumulation of charges or heat during laser irradiation is called fragmentation [72]. It involves a gradual decrease in the average particle size with an increase in laser fluence [73]. For brittle materials, chances of brittle failure increase with laser induced stresses, which can lead to form irregular shaped particles during fragmentation [64].

The particles formed during laser ablation are highly charged with electrons in the plasma. These particles fuse and form strong bonds in the shape of a chain or web. Similar to coagulation,

particles formed by agglomeration also increase in size. Agglomerates start to form as soon as the condensation starts.

2.8 Summary

The above literature provides a survey on particle forming mechanisms that take place during laser ablation of solid targets. These mechanisms mostly take place simultaneously. Dependent on the laser intensity and other conditions, one or two mechanisms dominate. This is because the intensity distribution within a laser spot is not uniform (in Gaussian profiles). The peak power along the radial direction decreases from terawatt to zero. If the maximum fluency of a laser spot exceeds the evaporation threshold, it produces more than one type of particles [74].

Even though many theories exist to explain the formation of particle produced by laser ablation, these theories are far from completion. Experimental results obtained by different research teams did not show consistency in outputs. This inconsistency is due to the varying nature of the experimental setup and lack of capable detection and process analyzing tools.

Normally, hydrodynamic sputtering, spallation, and phase explosion produce micro-sized particle. Solid exfoliation can be identified by the irregular morphology of the fabricated particles. The difference between the Coulomb explosion and solid exfoliation are that the former mechanism occurs by accumulation of electrostatic energy, while the latter by the accumulation of thermal stresses. Coagulation, fragmentation, and agglomeration are the secondary particle forming mechanisms. These mechanisms do not involve in the fabrication of particles directly, but vary the size of particles that already formed.

Among the above discussed particle forming mechanisms, vapour condensation is the only one that produces nanoparticles and it is the main mechanism responsible for the formation of particle agglomerated 3-D nanostructures.

Chapter 3 Experimental Setup and Procedure

This chapter explains the experimental setup adopted and the procedures followed. The main piece of equipment used for this research study is a femtosecond laser system with megahertz repetition rate. The system is located in the Micro and Nano Fabrication Research Laboratory at Ryerson University, Toronto, Canada.

3.1 Laser micro nano fabrication workstation

An in-house built laser micro nano fabrication workstation was employed for this study. The laser system is a diode-pumped Yb-doped fiber oscillator / amplifier system. It produces an average power of 12 W with repetition rates at 200 kHz, 2, 4, 8, 13 and 26MHz. Pulse duration can be set at 10 ps, 300 fs, 700 fs and 200 fs.

Two sets of experiments were performed. One optical configuration was designed to perform nanostructure fabrication with laser beam of double wavelengths (1030 nm and 515 nm). This

setup was used to investigate the relation between wavelength and ring size. The other optical configuration was used to fabricate nanostructures by a laser beam of a single wavelength (1030 nm). This setup was used to study all laser parameters other than wavelength and their influence on the size and morphology of created particle-agglomerated nanostructures.

3.1.1 Optical setup used for wavelength study

Figure 3.1 gives the optical setup used to generate laser beams of double wavelength. The $\lambda/2$ wave plate is used to rotate the polarization direction of linear polarized laser radiation. A beta barium borate (BBO) crystal is used for second harmonic generation (SHG). The output consists of two femtosecond laser pulses of wavelengths 515 and 1030 nm with a pulse width of 214 fs. The time delay between the two pulses is calculated to be ~ 1 ps.

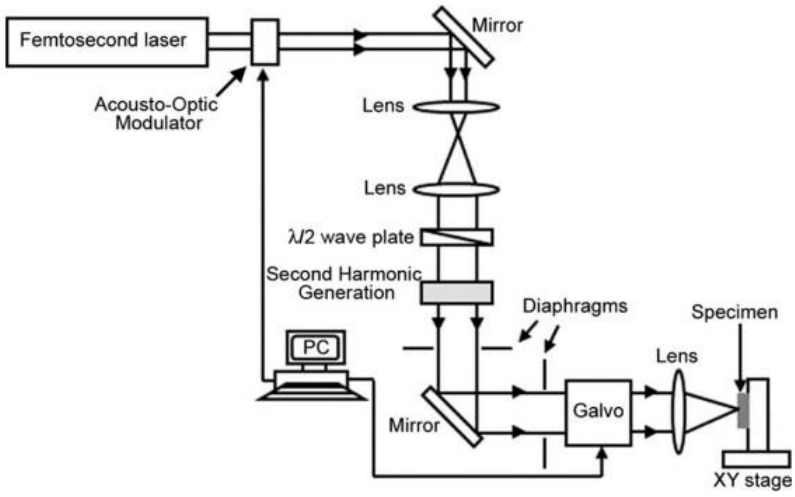

Figure 3.1: Experimental setup for wavelength study

As pulse repetition rate increases, the efficiency of SHG reduces significantly. In the absence of BBO crystal the output consists of only 1030 nm laser pulses.

3.1.2 Optical setup used for other laser parameters study

The schematic drawing of the laser setup used to study laser parameters other than wavelength is given in Figure 3.2. The output diameter of laser beam was 4.5 mm then expanded to 9 mm using a combination of UV fused silica plano-convex (F' = 100) and a plano-convex (F' = 200) lenses. A polarizer and analyzer are used to rotate and analyze the beam polarization. A shutter is used for pulse number control.

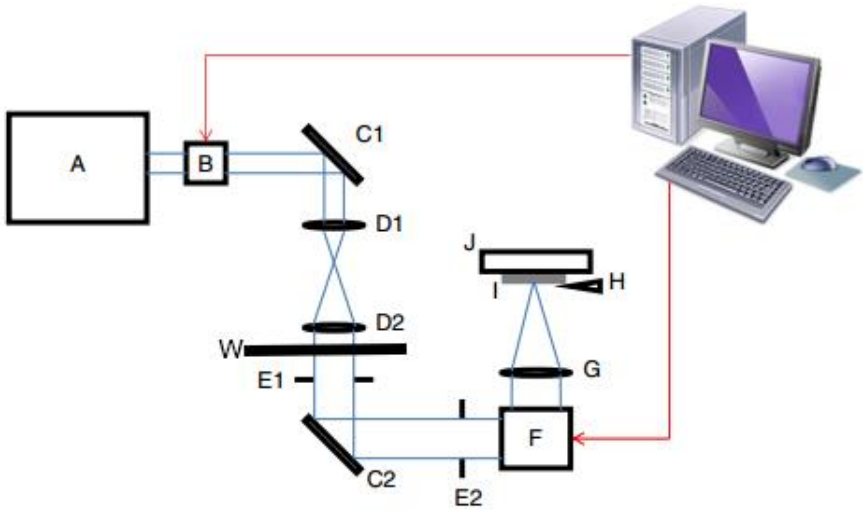

Figure 3.2: Experimental setup for polarization (A, ultrafast laser source; B, acousto-optic modulator; C1 and C2, mirrors; D1 and D2, beam expander; E1 and E2, diaphragms; F, galvoscanner; G, telecentric lens; H, nitrogen nozzle; I, sample; J, 3-axis stage; and W, wave plate)

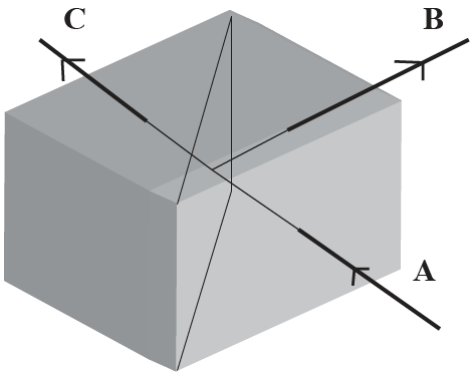

Figure 3.3: Wallaston prism to manipulate laser polarization

For polarization studies, a Wollaston prism was kept in between mirror “C2” and diaphragm “E2” as shown in Figure 3.3. Rays marked as “A” in Figure 3.3 represents the reflected laser waves from mirror “C2” towards galvoscanner “F”. To produce circular polarization, λ/4 wave plate was kept in between lens “D2” and diaphragm “E1”. The wave plate was adjusted until equal intensity laser lights were obtained after Wollaston prism, i.e. “B” and “C”. The intensity of the laser was confirmed by placing a IR viewing card, which lights up with respect to laser intensity, across “B” and “C”.

Same procedure was repeated for other two polarized lasers. However instead of λ/4 wave plate, λ/2 wave plate was used. For elliptical polarized laser, wave plate was rotated until unequal laser intensities were obtained, across “B” and “C”. For linear polarized laser, wave plate was rotated until maximum laser intensity obtained in “C”.

3.2 Irradiation and specimens

The spot size of the beam at the sample is calculated to be 10.38 μm. Due to optical errors and distortion, the actual laser spot is estimated to be around 20 μm. The laser radiation is focused onto the specimen surface to drill arrays of microvias. The computer connected to the laser system will control the laser beam to hit the sample surface 40 spots in sequence. The experiments were carried out in air at atmospheric pressure.

Figure 3.4: Array of micro-via [75]

The galvoscanner was used to scan in the x–y axes using EZCAD software, in a predetermined scan pattern: an array of points with a center-to-center distance of 100 μm. Figure 3.4 shows an array of micro-via obtained.

The crystalline silicon wafers with an orientation of (100) and slabs (of aluminosilicate, aluminum, glass, titanium, slide glass, zinc ingot, graphite, and nickel) are used as target materials.

3.3 Characterization studies

The physiochemical properties of fabricated structures are analyzed by several techniques, such as optical absorption, morphology identification (nanotracing, Scanning Electron Microscopy, and Transmission Electron Microscopy), and phase and element analysis (X-ray Diffractor, Energy Dispersive X-ray Spectroscopy). Below sections showed the setup and the procedure followed during experiments.

3.3.1 Optical absorption

Optical absorption studies on fabricated nanostructures were performed using two spectrometers. Visible-spectrum spectrometer produced reflection spectrums for visible lights only, whereas

UV-IR spectrometer produced spectrums from UV to IR, i.e. wavelength in between 200 nm and 1100 nm.

3.3.1.1 Visible-spectrum spectrometer

The nanostructures fabricated by laser system were studied for photon absorption under this spectrometer. A sample of silicon wafer with a minimum of 10 mm^2 area was prepared for irradiation using femtosecond laser. The reflection spectrum on fibrous nanostructure layer was measured using USB2000+RAD spectroradiometer, Ocean Optics, USA. The reflectance was measured for wavelengths in the range of 550–1000 nm, with 1 nm increments. This spectrometer provides a resolution of 0.35 nm and capture and store a full spectrum into memory every millisecond (1000 full spectra every second).

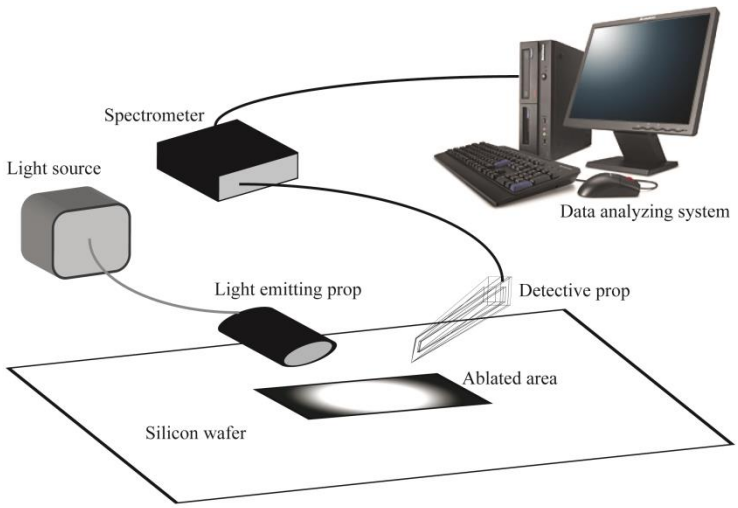

Figure 3.5: Setup of visible-spectrum Spectrometer

Figure 3.5 shows the schematic of visible-spectrum spectrometer used for the study. In this system, two different probes were used for light source and detect and measure the reflected light. This set up possibly increases the error in spectrum study.

3.3.1.2 UV-IR spectrometer

A UV-IR spectrometer (AvaSpec-2048 Fiber Optic Spectrometer) was used to study the reflected spectrum in the range of 200 nm to 1100 nm. The system was fixed with a 2048 pixel CCD Detector Array. The spectrometer has a fiber optic entrance connector, collimating and focusing mirror and diffractional grating. Presence of a focusing mirror increased the intensity of light on the sample. This spectrometer is especially suitable for low light level and high resolution applications. It was calibrated for stray light condition with off-focus light.

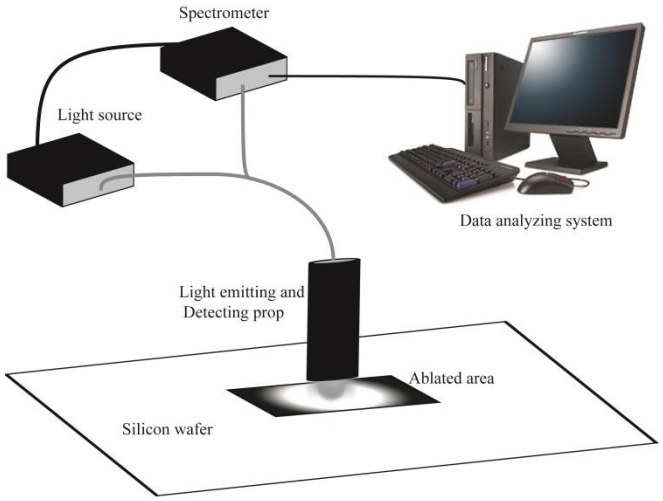

Figure 3.6: Setup of UV-IR Spectrometer

Figure 3.6 shows a schematic diagram of the setup of UV-IR spectrometer. The presence of single probe for both light emitting and light detecting functions increases the accuracy of this system than previous spectrometer.

3.3.2 Size measurement

Two different types of sizes were studied on the particle agglomerated 3-D nanostructures: the size of the nanocluster and the size of the agglomerated particles in the nanocluster. Nano-

tracking method was used to study the size of the nanocluster, whereas a manual measurement was performed on the Transmission Electron Microscope (TEM) images to identify the size of the agglomerated particles in nanocluster.

3.3.2.1 Nanocluster size by nano-tracking method

The size of the nanocluster in the 3-D nanostructure and their concentration was identified by a nano-tracking method. Size of the nanocluster plays a key role in photon absorption.

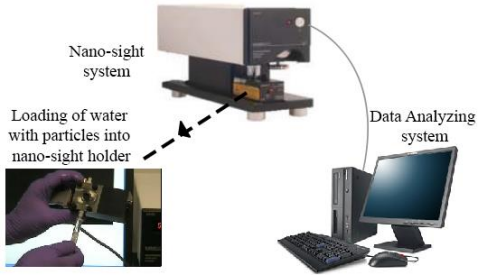

Figure 3.7: Nano-sight system

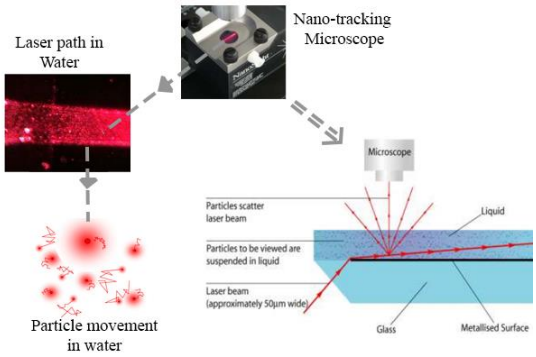

Figure 3.8: Functioning of nano-sight system

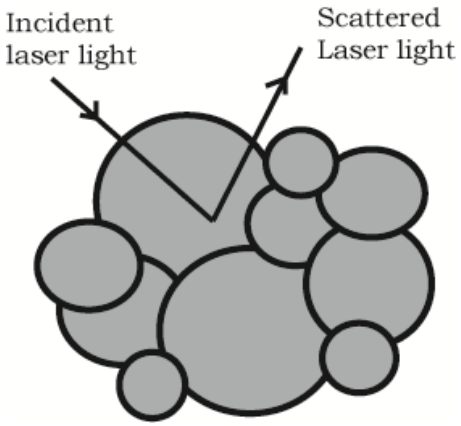

Figure 3.9: Nanocluster size study

Figure 3.7 shows the nano-sight system used to study the nanoparticle tracking. The nanostructure was separated from the silicon wafer into water as agglomerated particles by ultrasonic vibration. For this procedure, a small amount of prepared water (with the nanostructure) was injected into nano-sight holder. As shown in Figure 3.8, the scattered laser beam was studied and the nanocluster size concentration was obtained. Figure 3.9 shows the schematic of nanocluster size measured using above technique. It shows scattering of laser light on a broken piece from ring nanocluster, which is made of agglomerated nanoparticles.

3.3.2.2 Agglomerated particle size by manual measurement

Individual agglomerated particles were measured manually using “Image J” software on TEM image of the particle agglomerated 3-D nanostructures.

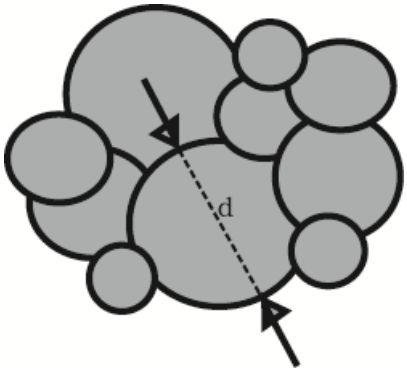

Figure 3.10: Manual measurement of agglomerated particle size using Image J software

The schematic in Figure 3.10 shows manual measurement of agglomerated particle size carried out using this software.

3.3.3 Physiochemical Analysis

The morphology of the generated nanostructures was examined under a scanning electron microscope (SEM) and a transmission electron microscope (TEM). An energy dispersive x-ray spectroscopy (EDX) and x-ray powder diffraction (XRD) were used to analyze material phases and element ratios.

3.3.3.1 Scanning Electron Microscope and Energy Dispersive X-ray spectroscopy (SEM - EDX)

Fabricated nanostructures were studied using a medium size chamber, variable pressure SEM (Model: SU1510 Hitachi). Morphologies such as top surface view and cross sectional view were performed with the SEM and the chemical element analysis was performed using EDX of the system.

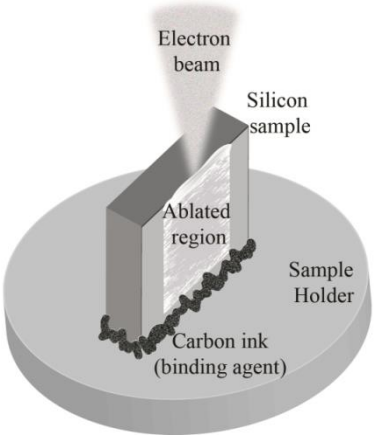

Figure 3.11: Cross section study on SEM

The system has quad bias gun electronics, which greatly improves the low voltage performance and increases beam current well suited for EDX measurements. Figure 3.11 shows a schematic of experimental setup used to study the cross sectional view of the nanostructure fabricated on a silicon wafer. The schematic in Figure 3.12 shows the processes involved in the preparation of cross sections of the silicon wafer. Silicon wafer was scratched by diamond cutter as shown in Figure 3.12. One side of the wafer was held firmly on a stable surface by a holding force and a finger force was applied on the other side of the wafer to break it along the scratch. Several sets of studies performed until a stable cross sectional view was obtained.

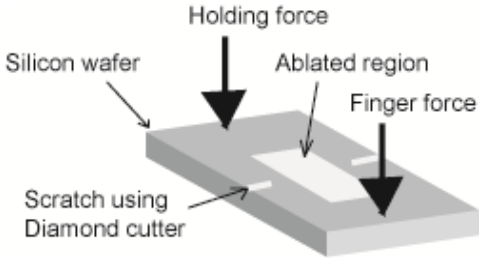

Figure 3.12: Preparation of cross sectioned sample

The cross sectioned sample was fixed on top of a sample holder using an adhesive, conductive carbon ink. The conductance of the silicon wafer was increased through gold spatter coating to improve the quality of the SEM image obtained.

3.3.3.2 X-ray Diffraction analysis (XRD)

The X-ray diffraction analysis was used to identify the phases of chemical compounds in fabricated nanostructures. The x-ray powder diffraction patterns were collected on Bruker AXS D8 Discovery GADDS diffraction system. Bruker AXS D8 Discovery Diffraction System was equipped with: high-power point focus from Cu-kα target, operating at 40 kV and 40 mA, small local beam spot (0.5 mm) allow micro-diffraction from different locations on the sample, high accuracy laser beam video camera for alignment of the selected area, Graphite monochromator (26.53^{o}) for elimination of Cu-kβ lines, and Hi-Star GADDS area detector for 2-D images.

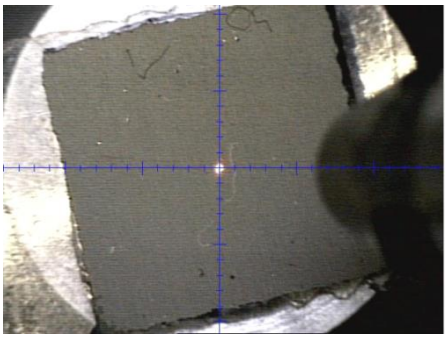

Figure 3.13 Mounting of sample on XRD sample holder

Figure 3.13 shows the mounting of a sample and its alignment with the laser beam. The central spot was the beam size. The diffraction pattern is collected as 2-3 high-resolution 2-D frames

(1024x1024 pixels). Each one of them covers a certain range (approx. 20^{o} 2-theta). After an accurate integration of the whole areas of the diffraction images they were converted to the common Intensity vs. 2-theta diffraction graph. The ranges were then combined into one diffraction pattern.

3.4 Summary

This chapter shows the experimental set up and the instruments used in the synthesis and the characterization of nanostructures. An in-house built, diode-pumped Yb-doped fiber oscillator / amplifier femtosecond laser system was used to synthesize nanostructures. Two different optical set-ups were used in the studies. The morphologies of the fabricated nanostructures were studied by TEM and SEM, where the elements and the phases in the structures were identified using SEM-EDX and XRD respectively. Size of the particles and clusters in the nanostructures were studied from TEM images and nano-tracking method. The optical absorption studies were performed using two different spectrometers with two different radiation spectrums.

Chapter 4 Particle size of the particle-agglomerated 3-D nanostructure

This chapter studies the influence of laser parameters on the size of 3-D nanoparticles networks. Size of nanostructures plays a key role in controlling the property of photon absorption of the fabricated 3-D nanostructures.

4.1 Formation of particle-agglomerated 3-D nanostructure

Figure 4.1 shows the processes involved in the formation of particle agglomerated 3-D nanostructures. The interaction of pulsed laser on target leads to material evaporation. The evaporated vapour condenses and forms nanoparticles. These particles agglomerate to each other and forms 3-D nanostructures. The TEM image on Figure 4.1 shows how particles agglomerated in 3-D nanostructures.

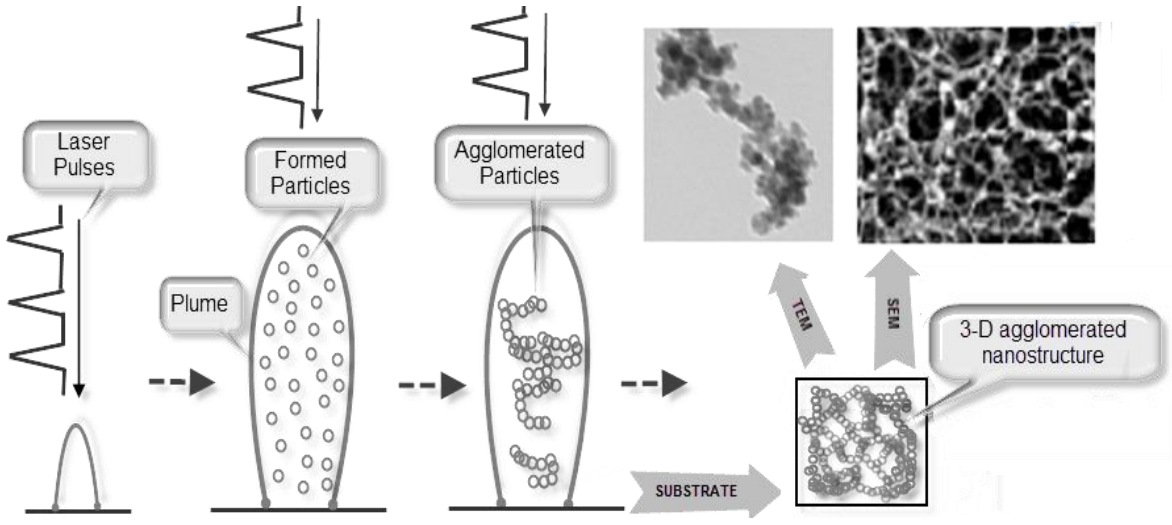

Figure 4.1: Evolution of laser plume, formation of nanoparticles, agglomeration of nanoparticles in the plume, and the formed 3-D particle agglomerated nanostructures

Experimental studies revealed that the agglomeration of particles normally occurs at high repetition rates, which is due to the increased interaction of laser pulse on the formed particles in the plume. The structures were formed with irregular ring morphology as shown in the SEM image in Figure 4.1.

4.2 Experimental studies on particle size of 3-D nanostructures

A better understanding of laser parameters and how they affect the particle size distributions are important to improve the properties of particle agglomerated 3-D nanostructures and their performance in intended applications. Three different studies were performed to analyze the particle size distributions with laser parameters: varying repetition rate at constant power,

varying repetition rate at constant fluence ratio, and varying fluence ratio at constant repetition rate. Equation 4.1 was used to calculate the fluence ratio.

$$\text{Fluence ratio} = \frac{\text{Applied fluence (J}cm^{-2}\text{)}}{\text{Threshold fluence (J}cm^{-2}\text{)}} \tag{4.1}$$

In equation (4.1), threshold fluence is the minimum laser fluence needed to initiate the ablation, which was calculated using equation 4.2.

$$\text{Threshold fluence (Jcm}^{-2}\text{)} = \frac{\text{Threshold power (W)}}{\text{Repetition rate (Hz)} \times \text{Laser spot area (cm}^2\text{)}} \tag{4.2}$$

In equation 4.2, the power that initiates ablation (at threshold fluence) is called threshold power, which was experimentally identified and the repetition rate is the number of laser pulses delivered per second. The size of the laser spot area is calculated using equation 4.3.

$$\text{Laser spot area} = \frac{\pi \, {d_1}^2}{4} \tag{4.3}$$

where, d_1 is the laser spot diameter, which is calculated with equation 4.4 [76].

$$d_1 = \frac{1.27 \, \lambda \, F_0}{D} \tag{4.4}$$

where, λ is the wave length of the laser, D is the laser beam diameter at the input of galvo-scanner, and F_0 is the effective focal length of scanner lens.

From the above mentioned three experimental studies, an explanation to relate the variation in particle size distribution with laser parameters and the plume properties is suggested. Further, the effects of laser parameters on the particle size distribution, the average particle size of the agglomerated particles in 3-D nanostructures as well as the modal transition laser fluence are explained.

4.2.1 Effects of fluence ratio on particle size distribution at a constant repetition rate

The TEM images of 3-D nanostructures obtained during experiments were made of fused nanoparticles as shown in Figure 4.1. The spherical nanoparticles were joined to form 3-D nanostructures.

Initially, experiments were performed to study the threshold fluence of aluminosilicate ceramic at different repetition rates. The study was performed with laser parameters of 200 fs pulse duration and 0.1 ms dwell time as shown in Figure 4.2. At each repetition rate, samples were ablated in atmosphere with increasing laser power until the initial ablation point was obtained. The initial ablation point was confirmed using SEM. Both threshold fluence and threshold power versus repetition rate are shown in Figure 4.2. Experiments were performed with varying fluence ratio. The maximum fluence ratio was taken as 3.2, which is the ratio between the laser power and the maximum threshold power at 25.2 MHz repetition rate.

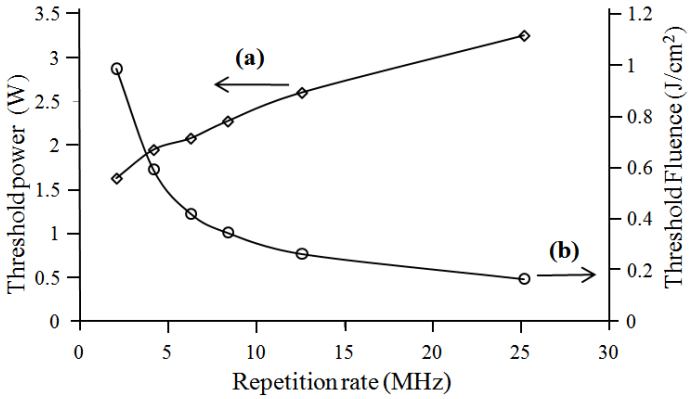

Figure 4.2: (a) Threshold power and (b) Threshold fluence of aluminosilicate ceramic. The experiments were performed at 0.1 ms dwell time and 200 fs pulse duration

A decrease in threshold fluence was obtained with the increase in the repetition rate. At high repetition rates, ablation efficiency increases due to the hypothesis of heat accumulation on the surface of material with the number of pulses. It tends to decrease the ablation threshold [77]. When the repetition rate was increased from 12.6 MHz to 25.2 MHz, the curve becomes saturated. It shows the existence of a minimum threshold fluence to start the ablation [78].

The particle size characterization studies showed that the range of particles in the 3-D nanostructure was from 7 to 31 nm. The procedure followed to measure agglomerated particle size was provided in section 3.3.2.2. This range indicates that the particles in the structures were made by vapour-condensation [62]. The particle size distributions in 3-D nanostructures (shown in Figures 4.3a - 4.3e), their averages, and their dispersions (shown in Figures 4.4a - 4.4b) were studied. A mathematical modal study of laser-induced particle formation showed that the nanoparticle sizes formed by vapor condensation fit within a bimodal distribution curve [58]. The results showed unimodal distribution rather than bimodal distribution. The possible reason could be the difference in the ablated material in our studies and the presence of species in the formed plume.

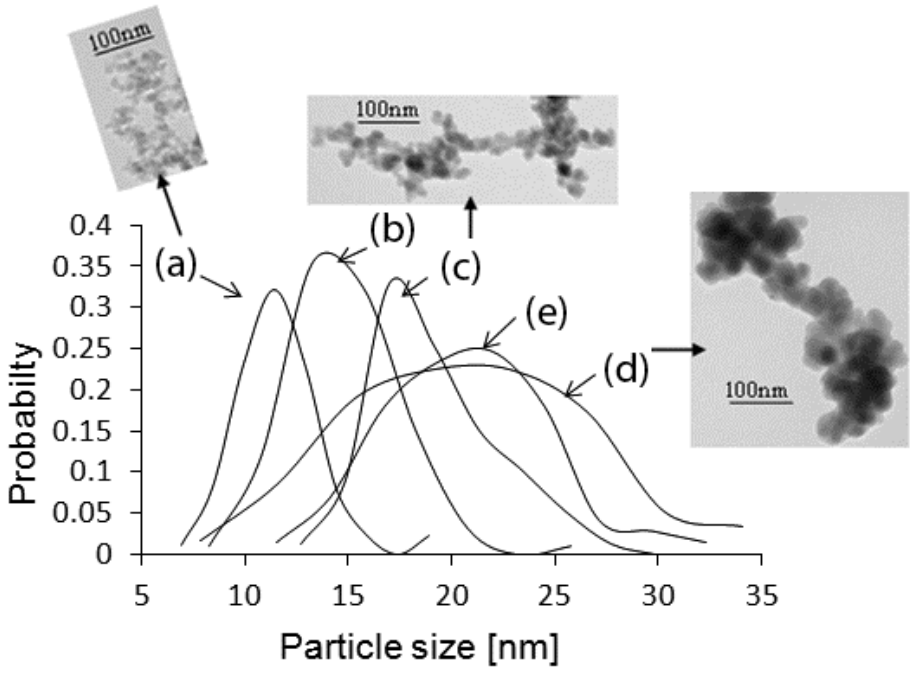

Figure 4.3: Particle size distribution curves, when the fluence ratio was (a) 1.6, (b) 2.0, (c) 2.4, (d) 2.8, and (e) 3.2 for constant repetition rate of 25.2 MHz. The sample of TEM images obtained at (a) 1.6, (c) 2.4, and (d) 2.8 fluence ratios

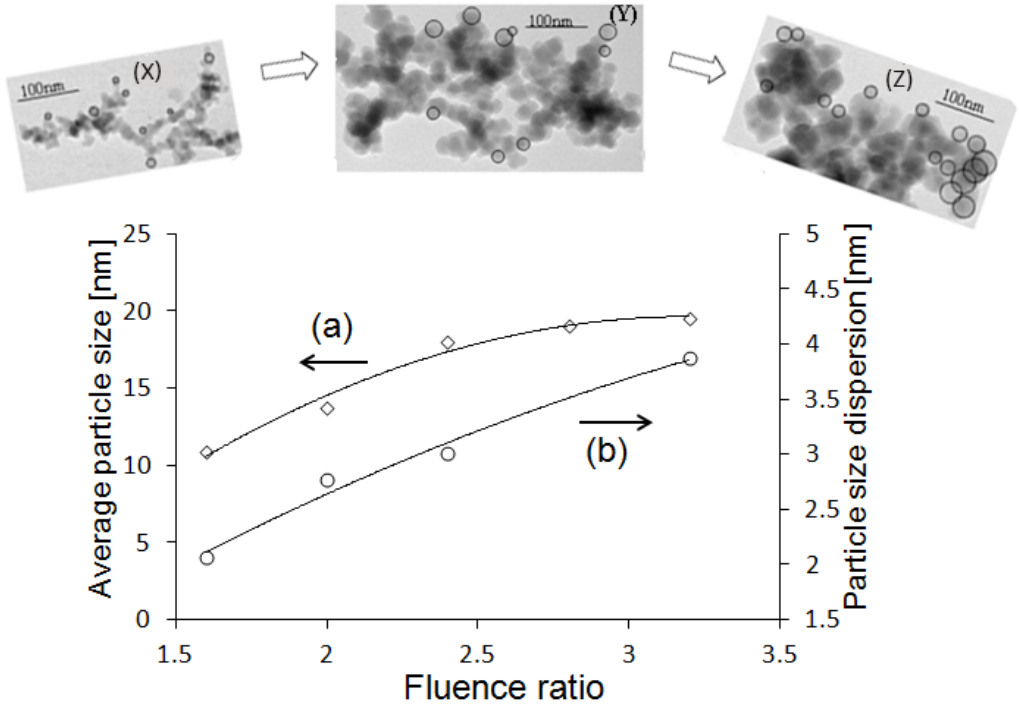

Figure 4.4: (a) average particle sizes (b) particle size dispersions obtained in the 3-D nanostructures for different fluence ratios at constant repetition rate of 25.2 MHz. TEM images with increasing fluence ratio given in X-Y-Z

TEM images in Figures 4.3 - 4.4 show an increase in the average particle sizes and their dispersions with increasing fluence ratio. The size of the 3-D nanostructure varies with the size of joined particles. This study shows that the laser fluence played an important role in determining the size of joined particles and thus the size of the nanostructures. Approximately 150 particle sizes were measured from each sample and 10 samples were studied to obtain each average particle size. The average particle sizes in 3-D nanostructures increased from 10 to 20 nm when the fluence ratio was increased from 1.6 to 2.4. The average particle size remained at an approximately constant diameter of 20 nm when the fluence ratio was increased beyond 2.4 to 3.2. The corresponding changes in laser intensities and laser fluences were $3x10^{10}$ to $6x10^{10}$ W/cm^2 and of 0.37 to 0.84 J/cm^2, respectively.

Even though it is not accurate to compare the values obtained from different studies due to the varying nature of the devices, ambient conditions, and material properties, the value varying trends in the obtained results could be. The obtained results have a good agreement with those obtained previously by different researchers for the size variation of singly distributed particles. Vitiello et al. have shown the same trends in the averages and the dispersions of gold nanoparticle sizes produced using laser fluence and laser intensity values from 0.3 to 1.1 J/cm^2 and $3x10^{12}$ to $1.1x10^{13}$ W/cm^2, respectively [54]. Another study of fabricated nickel and silicon nanoparticles showed similar trends in the range of particle sizes with laser intensity [55]. The important difference between the current study and already performed studies by other researchers is that the effects of laser parameters on the joined particles of the 3-D nanostructures were analyzed, instead of singly distributed. The joined particles control the size of nanostructures as well as their properties.

Laser-material interaction studies have shown that the laser plume temperature increases with the increase in laser energy and intensity [56], [63]; also the amount of supersaturation and the nucleation rate decrease with the increase in the plume temperature [58], [79–81]. Vapour condensation theories showed that the rate of nucleation increases faster than linear with the amount of supersaturation. However, the rate of condensational growth of particles is approximately linear with the supersaturation. Hence, the average sizes of formed particles decrease with an increase in the supersaturation [82]. By considering all those previous research results, an explanation is formed to predict the formed particle sizes. The variation in average particle sizes in Figure 4.4 could be explained as follows. Increasing (plume) temperature leads to a chain of effects: an increase in (plume) pressure, a decrease in the amount of supersaturation, and a decrease in nucleation rate as well as the growth rate. Though both nucleation rate and the growth rate decrease with an increase in plume temperature, the effect of the decrease in nucleation rate overcomes the growth rate, which results in the increase of average particle sizes formed [61], [79–83].

At very high fluence ratio (between 2.4 to 3.2), the plume temperature becomes saturated, which could be reflected by the saturation in the average particle size in Figure 4.4 (a) [84]. Though plume temperature is saturated at high fluences, the amount of material ablation continuously increases. This leads again to an increase in saturation of plume, which reduces the size of particles formed. This change could be observed in Figure 4.3 [between (d) and (e)], where the maximum particle size decreases when the laser fluence increased from 2.4 to 3.2. The range of particle sizes increases with fluence ratio because the nucleation of particles occurs until the final constant condensation temperature is reached [62]. Figure 4.4 (b) shows an increase in particle

size dispersion from 2 to 4 nm with the increase in fluence ratio. This may be due to the change in plume size and the particle cooling rate through the plume with the increase in laser fluence. The effect of changes in laser fluence along with the used Gaussian laser pulse could be reflected by the particle size distribution obtained in Figure 4.3 (a) - 4.3 (e). Fewer large sized particles represent the possible peak fluence, fewer small sized particles represent the possible low edge fluence, and high number of average size particles represents the possible average fluence portions of the laser profile. Further, the Gaussian profile pulse is a combination of laser waves with different energy levels. There is a high possibility that more than one mechanism take place during particle formation [74]. However, previous particle characterization studies confirmed the presence of only vapour condensed particles. The possible reason could be the direct evaporation of species during laser ablation without an intermediate melt zone due to ultra-short femtosecond pulse duration.

Disagreements may exist in applying nucleation theory for nano-scaled structures. But the studies in aerosol particle formation performed by previous researchers confirmed the likelihood of this theory [85]. Another study showed that the nucleation theories could be applied when the critical size is greater than 16 to 20 molecular formulas [86]. For different gas–liquid nucleation conditions, a consistent underestimation in the nucleation rates for different temperatures and super-saturations were recorded. However, the trends in changes of averages and dispersions of particle size presented agreed well with nucleation theories [87].

4.2.2 Effects of repetition rate on the particle size distribution at a constant laser power

TEM images obtained at different repetition rates are shown in Figure 4.5. At each repetition rate, the sizes of agglomerated particles were measured from these images, and the particle size distribution curves were obtained, which are shown in Figure 4.6.

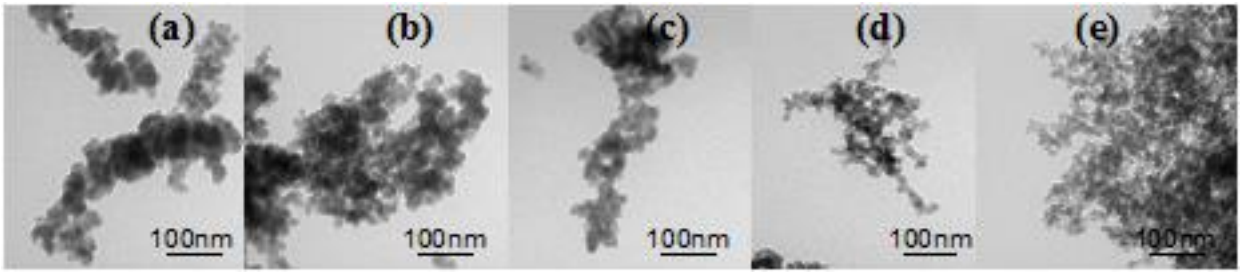

Figure 4.5: TEM images obtained from the 3-D nanostructure at repetition rates of (a) 2.1, (b) 4.2, (c) 8.4, (d) 12.6, (e) 25.2 MHz, at the constant power of 10.5 W

In Figure 4.6, the particle size distributions obtained at the repetition rates of 2.1, 4.2 and 8.4 MHz are bimodal, while 12.6 and 25.2 MHz are unimodal. Studies have shown that the mechanism that forms nanoscale particle size distributions during femtosecond laser ablation is the vapour condensation. The average particle size formed by vapour condensation is well below 100nm due to the high cooling rate of the expanding plasma [88].

The particle size distributions shown in Figure 4.6 are in nanoscale, which indicate the occurrence of the vapour condensation process during particle formation. The chances of forming bimodal distribution decreased with an increase in repetition rate.

Formation of a bimodal distribution is determined by how the particles are formed during nucleation. Previous studies have shown that the nucleation during vapour condensation can take place in two different routes, under the influence of ionized species and under the influence of neutral species. The growth rate of particles under the influence of ionized species is higher

compared to the neutral species [89]. At constant laser power, an increase in repetition rate decreases the laser fluence and thus the amount of ionized species formed in the laser plume [61]. The presence of higher amount of ionized species in the plasma due to the increase in laser fluence increases the growth of particles, whereas neutral species in the same plume grow on their normal phase. The combined effect of growth rates from these two streams could be the reason for the formation of bimodal particle size distribution. If the amount of ionized species presence in the plume is not sufficient, due to the decrease in laser fluence, the particle growth is only influenced by the neutral species, which results in the formation of unimodal distribution. This study shows that the decrease in ionized species presence in the plume could be the possible reason for switching from bimodal to unimodal particle size distribution.

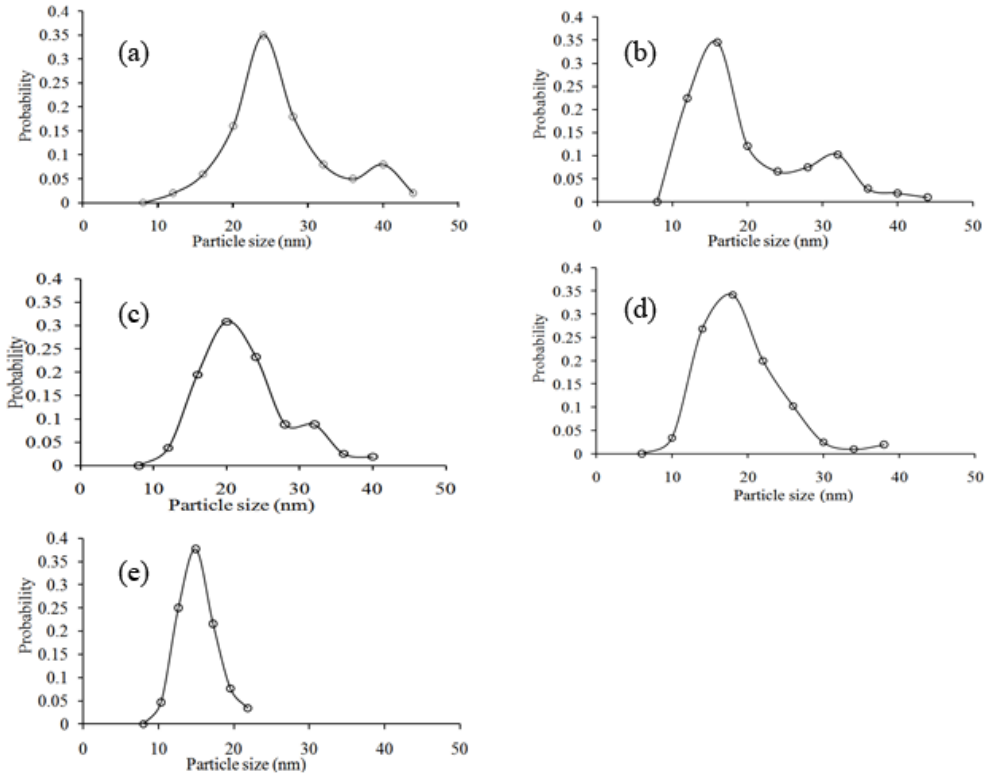

Figure 4.6: Particle size distributions obtained at the repetition rates of (a) 2.1, (b) 4.2, (c) 8.4, (d) 12.6, (e) 25.2 MHz, at the constant power of 10.5 W

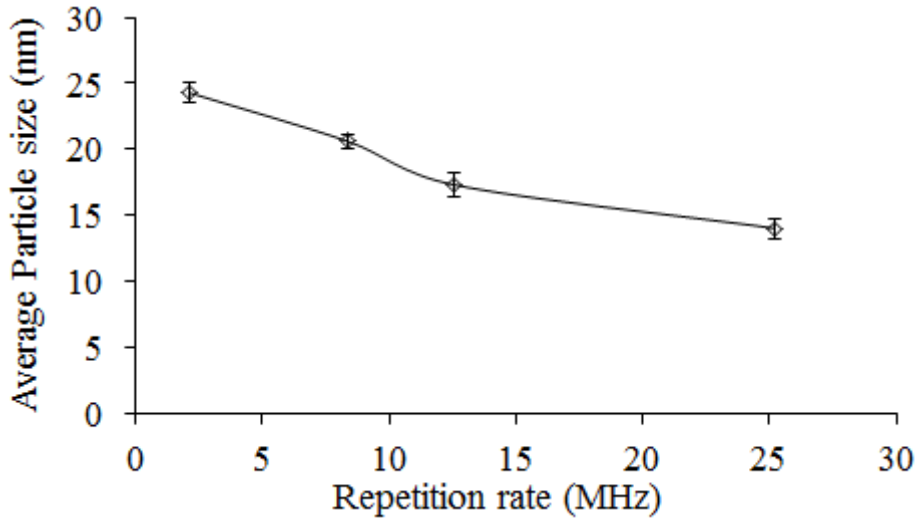

Figure 4.7: Average sizes of agglomerated vapour condensed particles obtained in the 3-D nanostructure at the constant power of 10.5 W

The average particle sizes at each repetition rate are plotted in Figure 4.7. The average particle size was obtained by adding the diameters of particles at each repetition rate and dividing by the total number of particles at that particular repetition rate. Three sets of experiments were performed for each repetition rate and the error bars show the variation in average particle size. The rate of nucleation of vapour condensed particles increases faster than linear with the amount of supersaturation. However, the rate of condensational growth of particles is approximately linear with the supersaturation. Hence, the average size of formed particles decreases with an increase in the supersaturation [82]. Furthermore, an increase in the plume temperature decreases the amount of supersaturation, which results in forming larger particles [81]. Factors that determine the plume temperature for varying repetition rates could be the laser fluence and the amount of heat accumulation due to the decrease in pulse interval. An increase in the laser fluence as well as in heat accumulation results in the increase of plume temperature [63], [90]. Laser fluence and heat accumulation have an opposite influence on plume temperature.

In Figure 4.7, the average particle size decreased with the increase in the repetition rate. At constant laser power, an increase in the repetition rate decreases the laser fluence, which decreases the plume temperature and increases the supersaturation. These changes led to a decrease in the average size of particles formed with increasing repetition rate at constant laser power. This study shows that laser fluence plays a more critical role in controlling the average particle size than the heat accumulation, when the repetition rate is increased at constant power.

4.2.3 Effects of repetition rate on the particle size distribution at a constant fluence ratio

Agglomerated particle size distributions were studied in the 3-D nanostructures for different repetition rates at the constant fluence ratio of 3.2. The study was performed with the maximum possible fluence ratio that could be obtained from our laser system to increase the chances of getting nanostructures at all repetition rates and to harvest the maximum number of agglomerated particles on those structures. Figure 4.2 (a) shows that the threshold power for repetition rate of 25.2 MHz was 3.25 W. The maximum power from our laser system is approximately 10.5 W (on the material surface). From this, the fluence ratio was taken as 3.2, and this ratio was maintained at all repetition rates. The constant fluence ratio was taken to minimize the effect of change in threshold fluence with repetition rate.

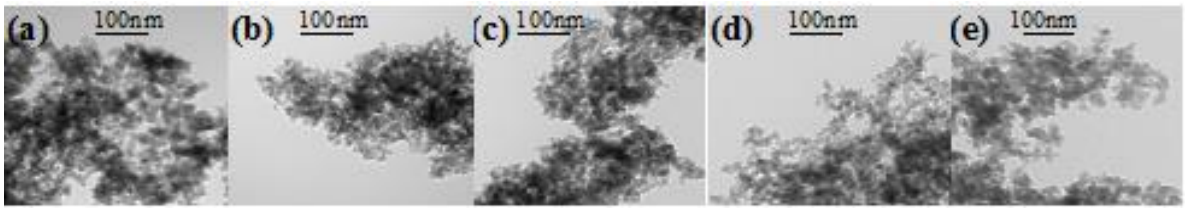

Figure 4.8: TEM images obtained from the 3-D nanostructure obtained at the repetition rates of (a) 4.2, (b) 6.3, (c) 8.4, (d) 12.6, (e) 25.2 MHz, at constant fluence ratio of 3.2

The experiments were performed to study the agglomerated particle size distributions in the 3-D nanostructures at the constant fluence ratio of 3.2 for different repetition rates. TEM images obtained at each repetition rate are shown in Figure 4.8.

In Figure 4.9, bimodal particle size distributions were obtained at 4.2 MHz and 6.3 MHz (at high laser fluence), while unimodal distributions were obtained at other repetition rates (at low laser fluence). As discussed in section 4.2.2, the reason for the formation of bimodal distribution could be the influence of ionized species during vapour condensation. The average particle size obtained at each repetition rate for constant fluence ratio of 3.2 is shown in the Figure 4.10.

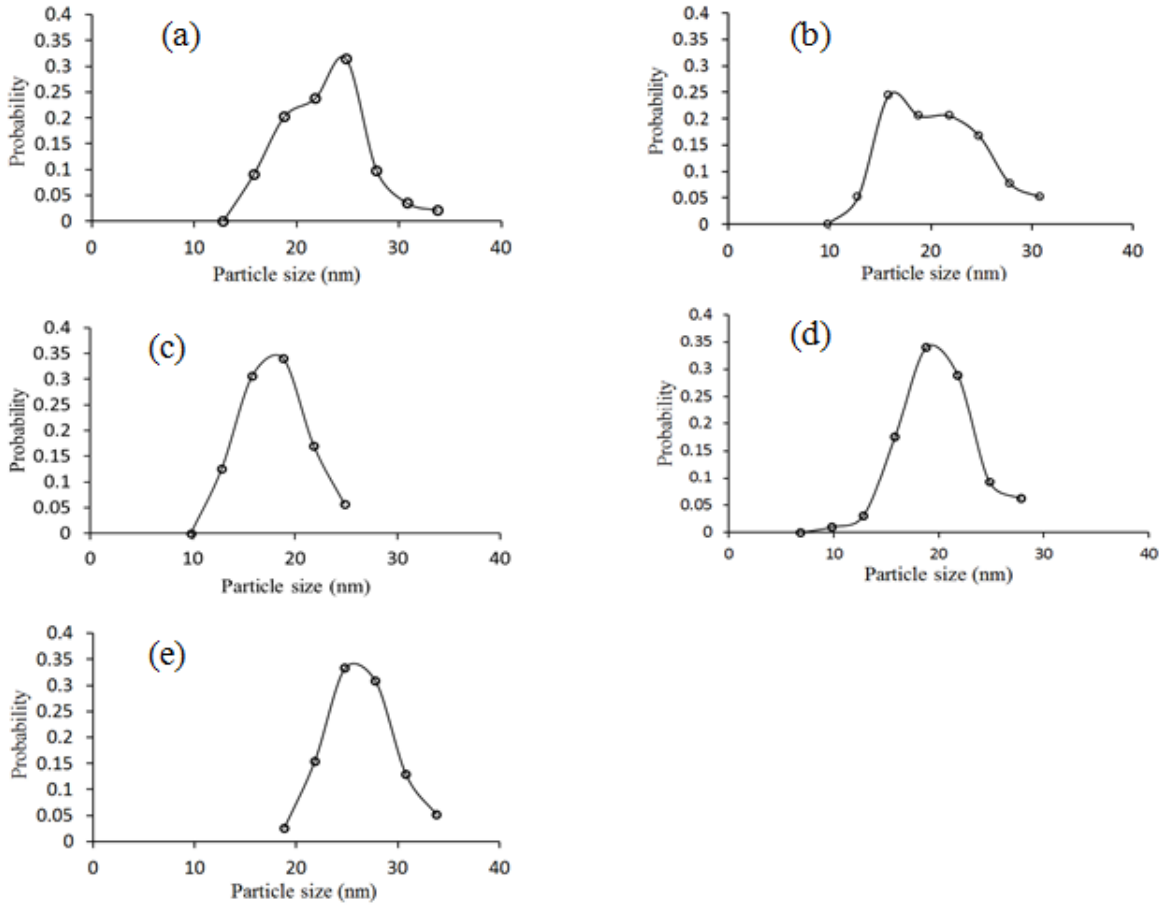

Figure 4.9: Agglomerated particle size distributions obtained at (a) 4.2, (b) 6.3, (c) 8.4, (d) 12.6, (e) 25.2 MHz during the laser ablation of aluminosilicate ceramic at constant fluence ratio of 3.2

When the repetition rate was increased from 4.2 MHz to 8.4 MHz, a decrease in the average particle size was obtained as shown in Figure 4.10. The laser fluence decreased, when the repetition rate was increased from 4.2 MHz to 8.4 MHz. Even though heat accumulation increased during this change in repetition rate, decrease in the laser fluence played a critical role in determining the average particle size in that range. When the repetition rate was increased beyond 8.4 MHz, the average particle size also increased. This change in average particle size shows that the heat accumulation could have played a major role than the laser fluence beyond 8.4 MHz.

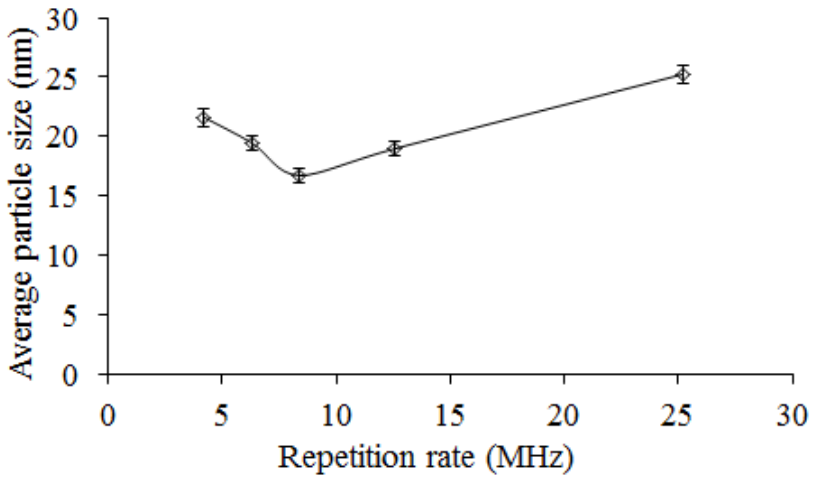

Figure 4.10: Average sizes of agglomerated particles obtained in the 3-D nanostructure obtained at constant fluence ratio of 3.2

In Figure 4.11, at constant fluence ratio, the change in laser fluence was negligible at repetition rate beyond 8.4 MHz. This further shows that the decrease in influence of laser fluence beyond 8.4 MHz at constant laser fluence ratio. The increase in repetition rate led to a decrease in cooling time between each pulse. Hence, the total pulse interaction time of both plume and target material at a given dwell time increased. Also, the applied laser power was increased with

repetition rate leading to an increase in the laser fluence. These effects resulted in an increase in plume temperature, which decreased the amount of super saturation and the nucleation rate and at the same time increased the size of formed particles.

4.3 Particle size distribution modal transition

A comparison between the effects of laser fluence on the distribution modals is shown in Figure 4.11. Bimodal distributions were obtained above the modal transition laser fluence (1.25 J/cm^2), while unimodal distributions were obtained below modal transition laser fluence, which coincides with the ionization threshold of a compound in aluminosilicate ceramic (Al_2O_3-SiO_2). These studies show that the distribution modals depend only on the laser fluence. Further, the amount of ionized species formed during laser ablation for a particular material solely depends on the laser fluence applied. This study also shows the possible influence of ionized species in the formation of bimodal distribution.

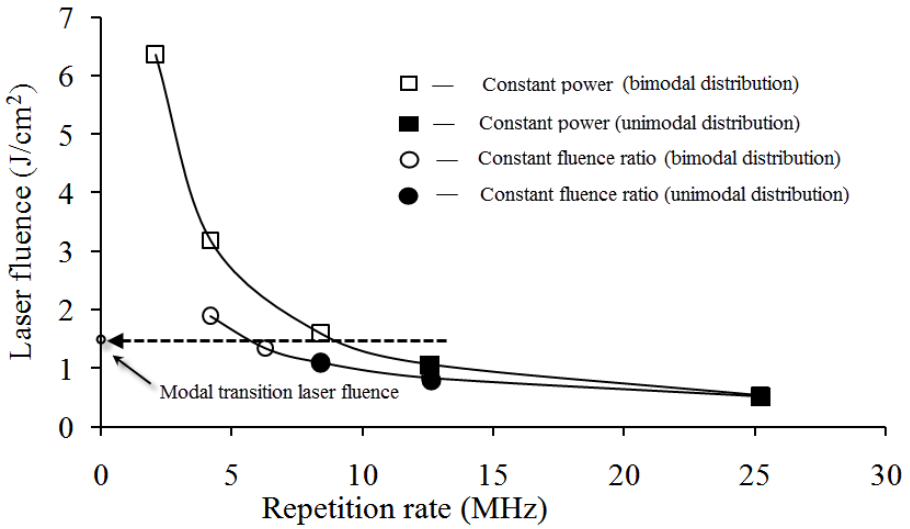

Figure 4.11: Effect of laser fluence on the distribution modals at the constant power of 10.5W and at the constant fluence ratio of 3.2

Studies performed above have also shown that the average size of agglomerated particles was influenced by the competing effects between laser fluence and heat accumulation for varying repetition rate in megahertz. At constant repetition rate, average particle size decreased with a decrease in laser fluence [54]. But in Figure 4.10, study in constant laser fluence ratio showed that the average particle size increased with increase in repetition rate (decrease in fluence) beyond 8.4 MHz. This study shows that both fluence and the repetition rate (in Mega-Hertz) have influence in determining the average sizes of particles obtained.

4.4 Summary

This chapter analyzed the effects of laser parameters (repetition rate and laser fluence) on the particle size of the 3-D nanostructures. A mechanism was proposed to predict the variation trend of nanoparticle size with laser parameters. Laser parameters affect plume temperature, pressure, and amount of supersaturation. The supersaturation then influences nucleation and growth rates of vapor-condensed nanoparticles, and thus the size of the formed nanoparticles. The suggested mechanism is not necessarily restricted for a particular material. Rather, it can be applied to femtosecond laser ablative synthesis of nanoparticles from any solid.

This analysis provides guidelines for the production of 3-D nanostructures with desired particle size. In general, low fluence and high repetition rates are required to achieve smaller particle size. However, the distribution of particle size increases at higher repetition rate. The selection of laser parameters is a trade-off between small particle size and wide particle size distribution.

An analysis was performed on the particle size distribution modals and the average particles sizes at varying megahertz repetition rates. The results showed that the particle size distributions transferred from bimodal to unimodal with the increase of repetition rate. There is a threshold laser fluence at which the particle size distribution modal transits from unimodal to bimodal. To the best of the author's knowledge, this is the first time such a threshold is reported.

Chapter 5 Ring size of particle-agglomerated 3-D nanostructures

Interconnected ring structures are characteristics of the particle-agglomerated 3-D nanoclusters produced by femtosecond laser ablation of solid targets. Particle agglomerated 3-D nanostructures were fabricated with different laser parameters, background gas, and materials. This study attempts to reveal the relations between these conditions and the ring diameter and to shed light on the formation mechanism of the ring structure.

5.1 Ring morphology

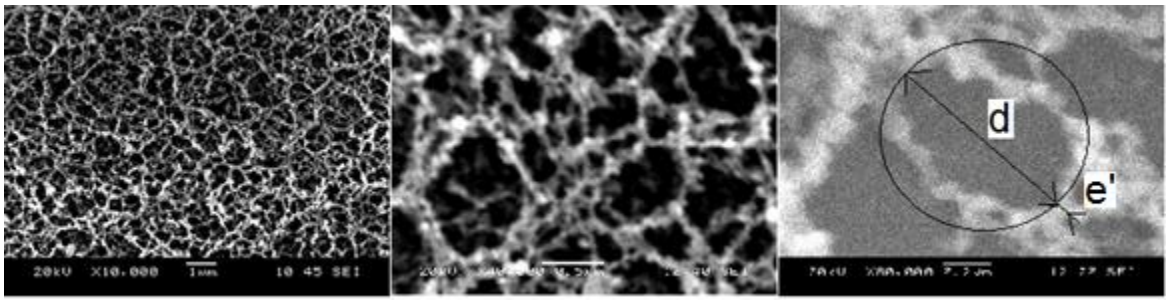

Figure 5.1: SEM images obtained by 1030 nm central wavelength femtosecond laser

The structures showed an irregular ring pattern with the overlapping of ring nanoclusters as shown in SEM images of Figure 5.1. The ring diameter (d) of the formed nanoclusters was measured using SEM images as shown in Figure 5.1. The ring diameter of a nanocluster is defined by the diameter of the smallest circle that completely inscribes the ring nanocluster. The maximum error (e´) (shown in Figure 5.1) in the ring diameter, i.e. in the size of the nanocluster, during our experiments was found to be ± 100 nm. The measured maximum error range was confirmed by the average nanocluster size obtained in section 6.3.3.2. The error in ring size refers to the possible mistakes occurred during the measuring process. Over 300 ring diameters from more than five SEM images were measured to produce each ring size distribution.

5.2 Ring formation mechanism

To explain the effect of laser parameters and the ablated materials on the formed ring nanoclusters, a structure formation mechanism is proposed. The dynamics of the species inside the plume and their interaction with an incoming laser pulse are taken as the key factors to propose a mechanism for the generation of the ring nanoclusters. The particle dynamics inside the plume during their agglomeration are essential to understand the structure formation mechanism for the zero-dimensional, nanoparticle agglomerated ring nanoclusters. Previous studies showed that the fabricated nanostructures were made out of vapour-condensed nanoparticles [47]. The ring nanocluster is made out of the agglomerated nanoparticles and the ring morphology could reflect the dynamics of the plasma species (particles, ions, atoms, or molecules) in the plume during their course of the agglomeration.

Plasma is an attractive medium for particle acceleration, which could support gigavolts of electric field per meter [91]. The possible mechanisms that could produce the excited particle acceleration inside the plasma are the relativistic plasma waves and the space-charge oscillations by the laser pulse-plasma interaction [91]. The presence of ponderomotive force, electrostatic Coloumb force, laser wake fields, and the laser plume dynamics could affect the motion of the plasma species [92–95].

A ring nanocluster formation mechanism is proposed based on the previous experimental and simulation studies performed on the laser pulse and the plasma species interaction [92], [93], [96]. The interaction of an intense laser pulse with an evolving plasma plume can give rise to a wide range of new phenomena, such as the generation of energetic electrons, ions, and acceleration of neutral atoms [91], [92], [95]. A detailed study on the directional movement of the accelerated species inside the plume is used to explain the ring nanocluster formation.

The interaction of a pulsed laser with the plume temporarily produces a quasi-free oscillatory quiver motion on an ion bound electron by the Coulomb force [92]. At a lower intensity, the atomic electrons oscillate with the same frequency of the laser light. With an increasing intensity, the species become ionized and the plasma electrons quiver with velocities close to the speed of light (c). This increases the relativistic electron mass, and the (V×B) force in equation 5.1 becomes significant [96].

When the strong laser pulses interact with the free electrons in the plasma, the electrons experience the Lorentz force (F_L), which is given in equation 5.1[96].

$$F_L = e\{E + (V \times B)\} \qquad (5.1)$$

where, e is the charge on the electron, V is the velocity of the electron, and E and B are the electric and magnetic fields in a plane of a Gaussian pulse as shown in Figure 5.2 (a). The electron oscillates along the direction of the electric field (E) with the velocity (V), as shown in Figure 5.2 (b). The V produced by E is given by equation 5.2 [96].

$$V = e\frac{E}{m\omega \cos(\omega t)} \qquad (5.2)$$

where, m is the electron mass and ω is the laser angular velocity. Under the action of a magnetic field, the electrons are accelerated in the direction of laser propagation, which is given by $(V \times B)$ in equation 5.1. The effect of these two forces is given by equation 5.1. The movement of the free electrons under these combined effects is shown in Figure 5.2 (c) [96].

To study the ring nanocluster formation, forces acting on the free electrons by the three dimensional Gaussian pulse should be known. Integration of the plane forces in equation 5.1 (in Figure 5.2 (c)) on a spatially confined Gaussian pulse field results in the formation of the ponderomotive force on the electrons, which is shown in Figure 5.2 (d) [96]. The ponderomotive force (F) can be given by equation (5.3) [97].

$$F = -\frac{e^2 \nabla E^2}{4\, m\, \omega^2} \qquad (5.3)$$

where, ∇E is the gradient of local instantaneous electric field. According to equation (5.3), ponderomotive is directly proportional to square of ∇E and inversely proportional to square of ω. Ponderomotive force is a charge dependent force, which strongly influence the force on ionized species [97].

The frequency of the laser light f can be given by equation (5.4).

$$f = \frac{c}{\lambda} \qquad (5.4)$$

where c , f ,and λ are the speed, frequency, and wavelength of the light respectively. The angular velocity and the frequency of the laser can be given by equation (5.5).

$$\omega = 2\pi f \qquad (5.5)$$

From equations (5.4) and (5.5),

$$\omega = \frac{2\pi c}{\lambda} \qquad (5.6)$$

For a propagating laser plane wave or a Gaussian beam, the local intensity I is related to the amplitude electric field, which is given by equation (5.7).

$$I = \frac{c\,\epsilon_0\,n\,|E|^2}{2} \qquad (5.7)$$

where, n is the refraction index, and ϵ_0 is the permeability in vacuum. In equation (5.3), the ponderomotive force F is directly proportional square of ∇E. From equation (5.7), an expression can be obtained for laser intensity gradient (∇I) and electric field gradient ∇E.

$$\nabla I \propto \nabla E^2 \qquad (5.8)$$

From equations (5.3) and (5.6) and expression (5.8), an expression is obtained to show the relationship between ponderomotive force with laser wavelength and intensity [96].

$$F \propto -\nabla I \,.\, \lambda^2 \qquad (5.9)$$

Expression (5.9) shows the ponderomotive force is proportional to the negative gradient of the laser intensity and the square of the wavelength. Studies showed the force on the ionized species is strongly influenced by the ponderomotive force [97]. Expression 5.10 is used to find the direction of ponderomotive force [98] in the plume.

$$c\,\tau > d_1 \qquad (5.10)$$

where, τ is the pulse duration. If expression (5.10) is satisfied, the radial component of the ponderomotive force dominates and accelerates the ions and electrons radially. During the experimental studies, the minimum pulse duration (τ) was 200 fs.

$$c\,\tau = 299{,}792{,}458\ (ms^{-1}) \times 200 \times 10^{-15}(s) = 60\mu m$$

From above calculation the value of $c\,\tau$ is greater than the laser spot size 10.5 μm. Hence, the radial component of the ponderomotive force dominates during experiment and accelerates electrons and ions radially.

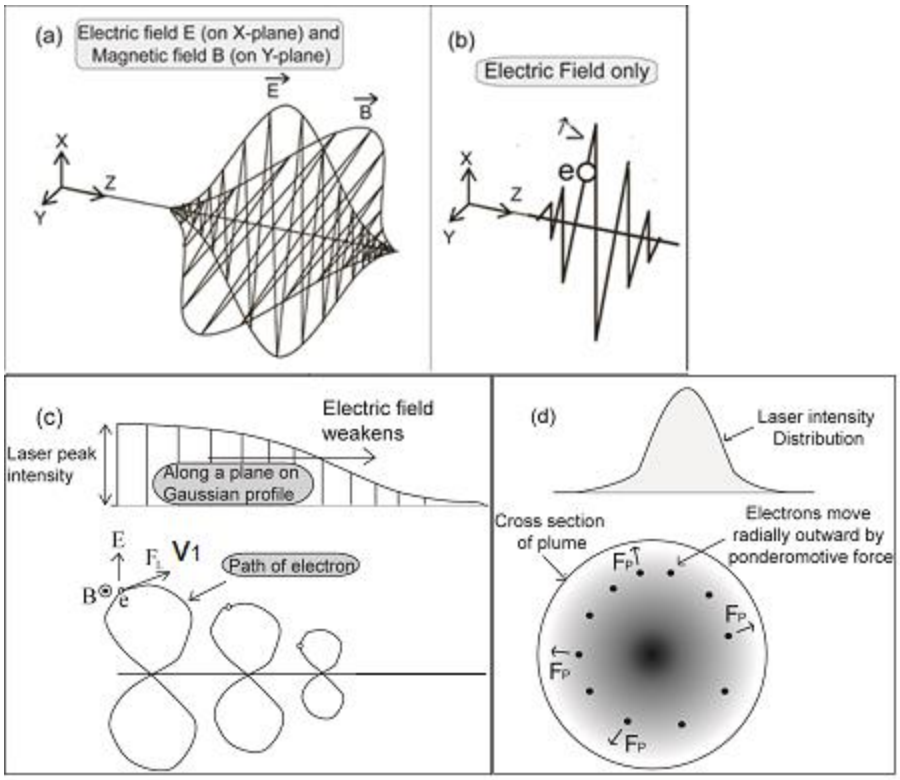

Figure 5.2: (a) Electric and magnetic fields on a plane surface of Gaussian pulse, (b) Electron movement by electric field (c) Electron movement by electric and magnetic fields on a plane surface (d) Ponderomotive force on free electrons by a Gaussian laser pulse

Figure 5.3 (a) shows the interaction of the consequent laser pulse with a formed plume. The laser intensity distribution on section A of the laser pulse marked in Figure 5.3 (a) is shown in Figure 5.3 (b). It shows the irreversible motion of the free electrons along the radial direction of the Gaussian laser profile from the optical axis by the ponderomotive force [96]. The ponderomotive force on the free electrons leads to accelerate the atoms, ionic species, and the neutral species as shown in Figure 5.3 (b) [92], [93]. Movement of neutral species becomes possible by their dynamic polarization, survival of excited states for a long time, and the quasi-free behaviour of excited electrons in a strong inhomogeneous laser field [92].

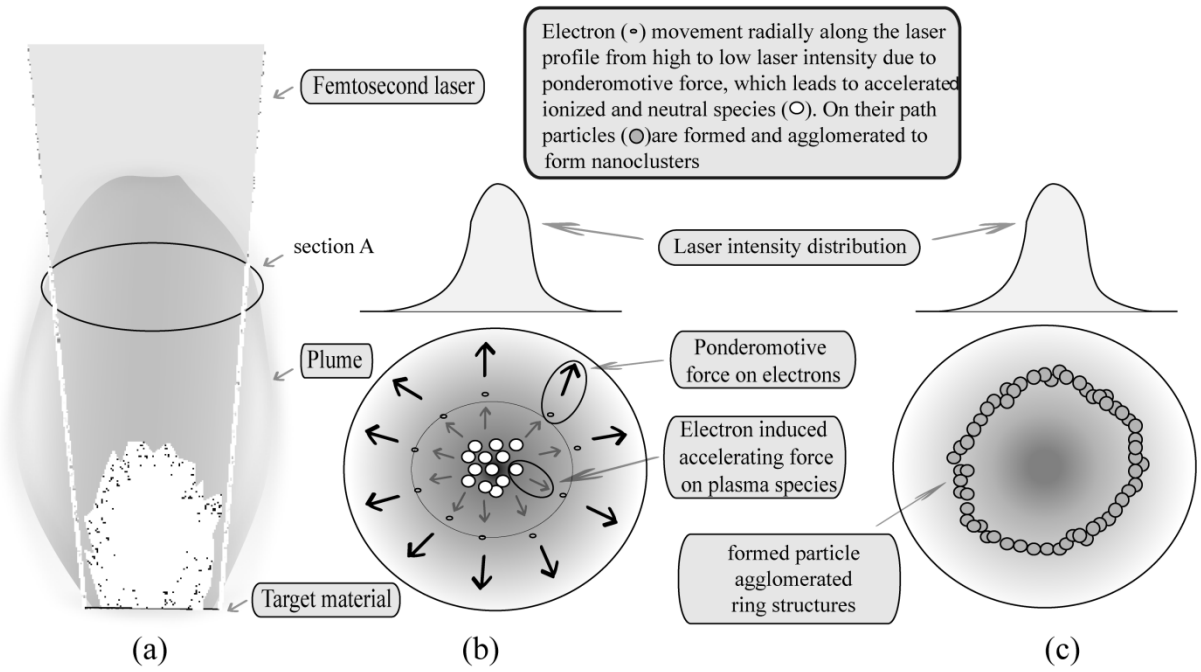

Figure 5.3: (a) Interaction of laser pulse with plume, (b) Ponderomotive force on electrons and induced accelerating force on atoms, ionic species, and neutral species on the cross section "A" (c) Formed and agglomerated nanoparticles on ring nanoclusters

There were two explanations given in two different studies for the acceleration of charged species. Firstly, motion of free electrons under the influence of ponderomotive force generates a radial current, which produces a strong magnetic field when the laser modulation frequency is close to plasma frequency. This self-generated magnetic field has an effect on the excitation of plasma waves and leads to the acceleration of charged particles [93]. Another study elaborates that the electrostatic effect between ions and electrons move the ionic species [99]. Also, the intensity-dependent force is similar to the ponderomotive force, which is proportional to the force acting on the charged species [92]. The movement of vapour species by excited plasma waves or by electrostatic effect and their agglomeration in a ring shape could be the most convincing reason for the formation of the ring nanoclusters as shown in Figure 5.3 (c). Along

their path of motion, vapour species might be condensed to form nanoparticles before their agglomeration.

The laser plasma instability due to the presence of several mechanisms is the main existing problem in analyzing the ring structure formation. Irregular ring shapes in Figure 5.1 confirm the influence of several mechanisms. The reasons for the irregular ring morphology could be distorted intensity pulse profile due to plasma shielding, ambient air flow dynamics, ionization of atmospheric air, non-uniform plasma density [93], and the location where particles are formed and agglomerated. A detailed study is performed to identify the effect of the ablated materials and the laser parameters on generated ring structures.

5.3 Experimental study on ring size

Several sets of femtosecond laser ablations were performed on different materials, such as glasses, ceramics, semiconductors, and metals, with different wavelengths, pulse energies, repetition rates, and pulse durations. Two ablation strategies were used during the wavelength study: single pulse ablation and double-wavelength double-pulse ablation. During the experiments the wavelength was kept at 1030 nm for single pulses and at 1030 and 515 nm for double pulses.

5.3.1 Effect of material properties on the ring size

Several studies performed on different materials showed that the ring size depends on the material properties. SEM images of 3-D nanostructures obtained on several different materials, such as metals, ceramics, and semiconductors, at constant laser operating conditions are shown in Figure 5.4. A ring size survey was performed on SEM images of different materials.

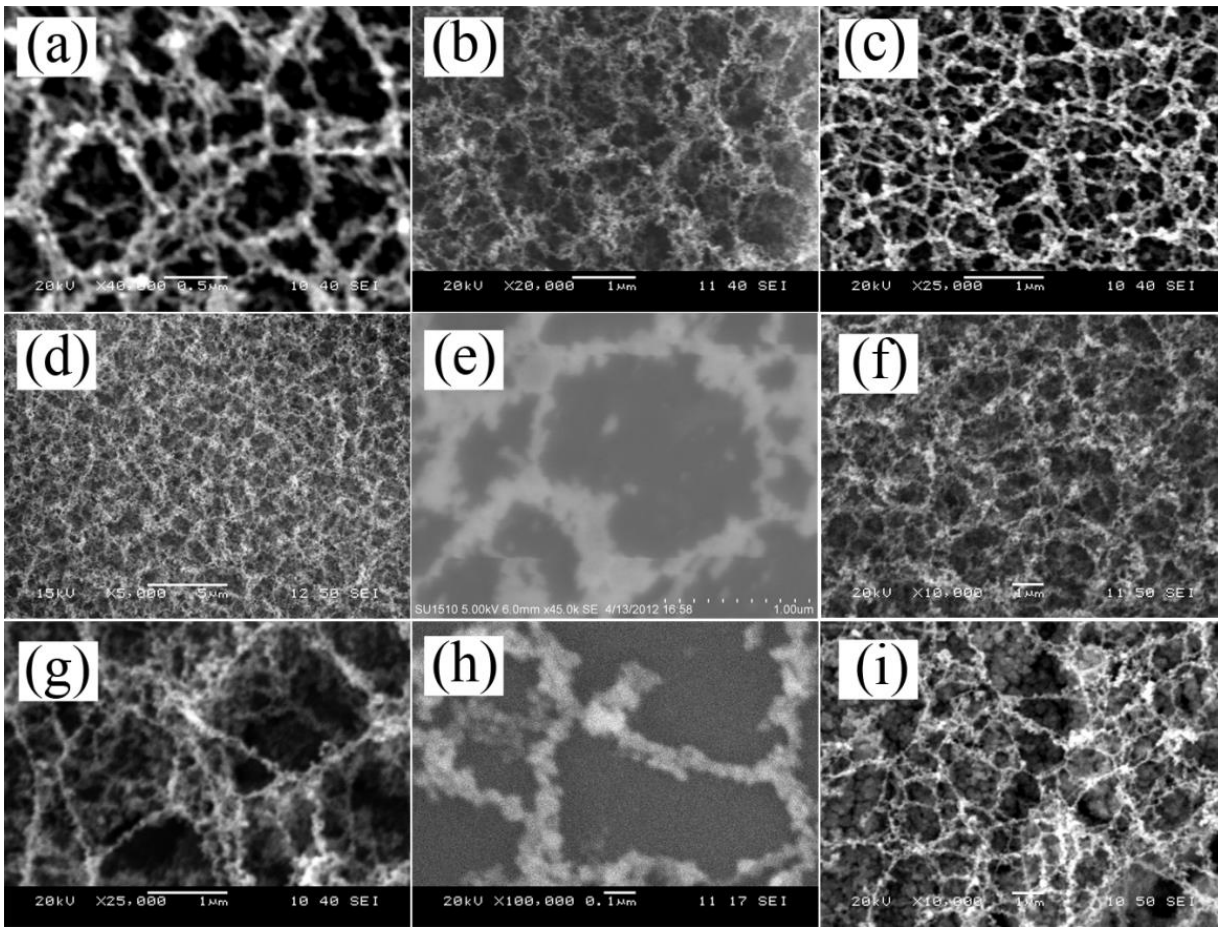

Figure 5.4: SEM images obtained for single pulses with 1030 nm central wavelength on (a) aluminosilicate ceramic, (b) aluminum, (c) glass, (d) titanium, (e) slide glass, (f) zinc ingot, (g) graphite, (h) silicon, (i) nickel

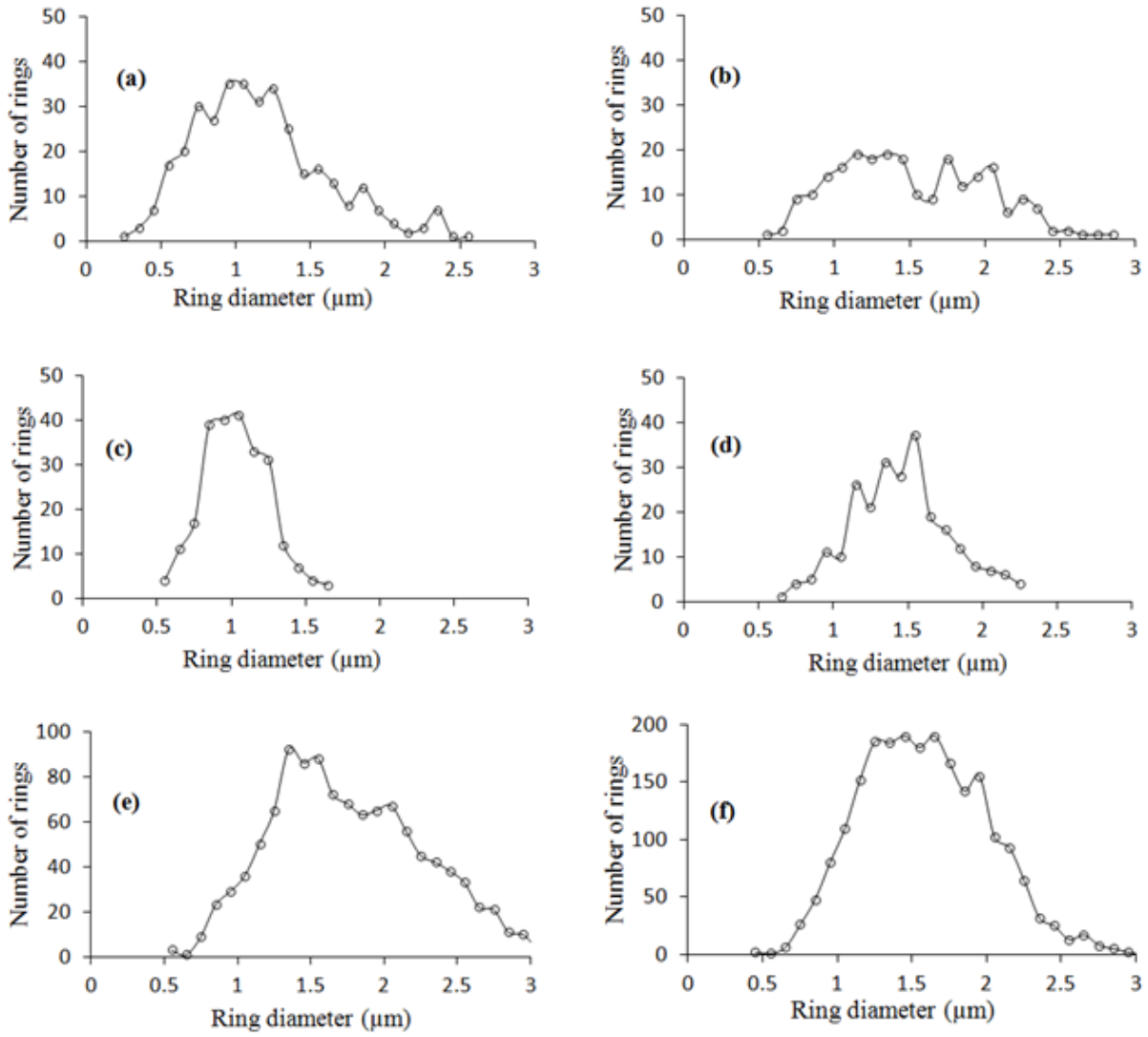

Figure 5.5: Ring size with materials (a) graphite (b) nickel (c) aluminosilicate ceramic (d) zinc ingot (e) gold (f) titanium, obtained at 11.0 W and 12.6 MHz with 1030 nm femtosecond laser

The ring size distributions obtained for different materials are shown in Figure 5.5 and Figure 5.7 (a). Large ring sizes were obtained on metals with a peak close to 1.5 µm. Ring size distributions for aluminosilicate ceramic, graphite, and silicon have a peak close to 1 µm. The ring size distributions obtained could be related to the ionization energy of species and the molecular weight of them.

Studies showed energy of the ions in the laser induced plasma increases with the charge. The electrons accelerate the ions by electrostatic interaction. The mean ion energy (Ei) transferred by electrons is given by the expression 5.11 [100].

$$Ei \approx (Z + 1)k_B T \qquad (5.11)$$

where, Z is charge multiplicity, T is the initial temperature of the plasma, and k_B is the Boltzmann's constant. Expression 5.11 shows that the energy of ions transferred by electrons is proportional to Z. The charge multiplicity increases with the amount of charge presence in the plasma. A decrease in ionization energy of species increases the amount of charges in the plume, which increases mean ion energy (Ei)in expression 5.11. An increase in ion energy (Ei) increases the travel distance of ions in plume and increases the ring size. Above explanation shows the effect of ionization energy on the size of the ring obtained.

On Table 5.1, for metals, the average ring sizes show a close relationship with ionization energies of them. Other than ionization energy, the types of bonding in materials could affect the ring size. In Table 5.1, the average ring sizes for silicon and graphite show a different values from other materials. Silicon and graphite forms covalent bonds, whereas all other materials were metals and forms ionic bonds. Previous studies showed that the density of the material is inversely proportional to the accelerated ion energy by the ponderomotive force [101]. In that study, the ponderomotive effect accelerated the species along laser direction. However, the densities of the species most probably have a same effect on the radially accelerated species. As the studies were performed in nanoscale, atomic weight or molecular weight could be a better property to relate the accelerated ion energy rather than the density.

Table 5.1: Materials used in experiments and their density, atomic weight, 1st ionization energy, and average ring obtained

Materials	Density (gcm^{-3})	Atomic weight	1^{st} Ionization energy / ($kJmol^{-1}$)	Average ring size / (μm)
Gold	19.30	196	890	1.76
Aluminum	2.70	26	580	1.94
Graphite	2.26	12	1090	1.17
Nickel	8.90	58	740	1.52
Silicon	2.33	28	790	1.08
Titanium	4.50	47	660	1.47
Zinc ingot	7.14	65	906	1.46

Decreasing molecular weight also increases the ring size. If titanium and aluminium are compared from Table 5.1, both have close ionization energies, however a noticeable variation in average ring sizes was observed among them due to varying atomic or molecular weight. A material with lower molecular weight could travel faster as well as stay longer inside the plume. This increases the chances of multi-interaction with consequent laser pulses, which increases the ring size. However, the ring sizes in Table 5.1 do not show perfectly the effect of ionization energy or atomic weight for all the materials. There are several possible reasons exist: The laser ablation process is highly dynamic and not necessarily produce an even distribution of mass inside the plume and the evaporated species change into their oxides as soon as interacting with atmosphere, hence not reasonable to compare the ring size with their initial atomic or molecular weights only.

5.3.2 Effect of wavelength on the ring size

A study was performed with silicon to verify the influence of wavelength on ring sizes. SEM images obtained on single wavelength (1030 nm) and on double wavelength (515 nm and 1030 nm) are shown in Figure 5.6. Over 2000 ring sizes from over 60 SEM images were studied to plot the ring size distributions shown in Figure 5.7.

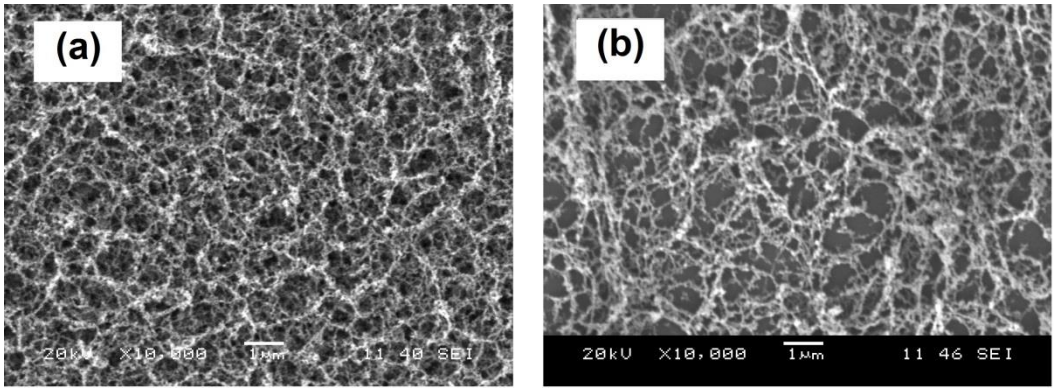

Figure 5.6: (a) 1030 nm wavelength (b) double wavelength 515 nm and 1030 nm

For single pulse with single wavelength, the peak number of rings was close to 1 µm (Figure 5.7 (a)) and for the double pulse double wavelength, a peak close to 0.525 µm (marked as '**P**') and a possible distorted peak close to 1 µm (marked as '**D.P**') were obtained (Figure 5.7 (b)).

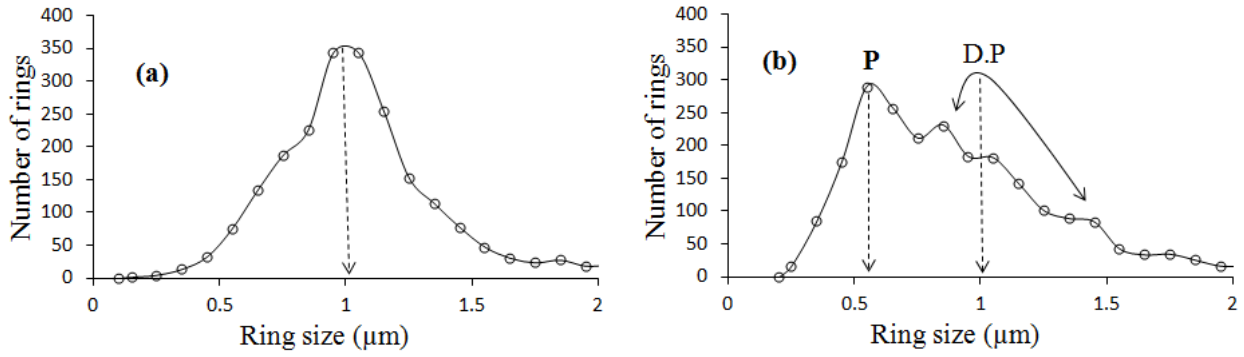

Figure 5.7: Ring size distributions with central wavelength at (a) 1030 nm and (b) 515 nm and 1030 nm

In double wavelength-double pulse, the 515 and 1030 nm pulses have a time lag of 1 picosecond and the 515 nm pulse precedes the 1030 nm. Studies have shown that the normal plume existence time is very much higher than 1 picosecond [102], [103]. Thus, when the second pulse was in action, the high strength evolving plume could have distorted the intensity profile of the incoming 1030 nm second pulse due to strong plasma shielding. This is a possible reason for the distorted peak in Figure 5.7 (b) close to 1 µm. This is a convincing evidence for the effect of laser profile and the related ponderomotive force in the formation of ring nanoclusters. Previous studies also showed that the electron acceleration caused by the ponderomotive force in an inhomogeneous field of a focused laser beam may be considerably refined by sophisticated spectral and temporal shaping of the accelerating laser beam [92].

A plasma-particle study has shown that the relativistic plasma particles or species generally travel behind the laser field only for a certain length in a certain phase of electromagnetic field. The maximum travel distance a particle could travel with respect to the laser field was given as half of the laser wavelength ($\lambda/2$) [104]. The peak ring sizes obtained for silicon in Figure 5.7 have shown a close relationship with the particle travel distance given in the above plasma-particle study. The ring diameter for peak in ring size distributions was close to the laser

wavelength. This could be obtained by the symmetrical traveling of species along the radial direction under the influence of ponderomotive force. Though presence of more than one wavelength in a Gaussian profile could have an effect on the obtained ring sizes, the dispersion in pulse wavelength is negligible when compared with obtained dispersion in ring sizes in Figure 5.7. The most convincing explanation for the variation in ring size is the distribution of ablated species inside the plume before the interaction of subsequent laser pulses. Possibly, the concentration of species is high along the core of the laser plume, which could be reflected by the maximum number of rings equivalent to laser wavelength in this study.

Further, the results in Figure 5.7 satisfy the obtained expression 5.9. i.e. the ponderomotive force increases with the increase in laser wavelength. The increased in ponderomotive force leads to increased acceleration of ionized species and results in an increased ring size.

5.3.3 Effect of pulse duration on the ring size

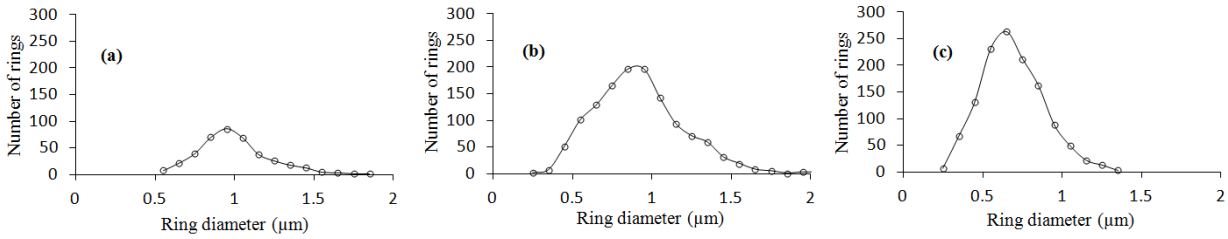

Figure 5.8: Ring size distribution obtained from SEM images of silicon at (a) 300 fs, (b) 1000 fs, (c) 5000 fs for 12.6 MHz

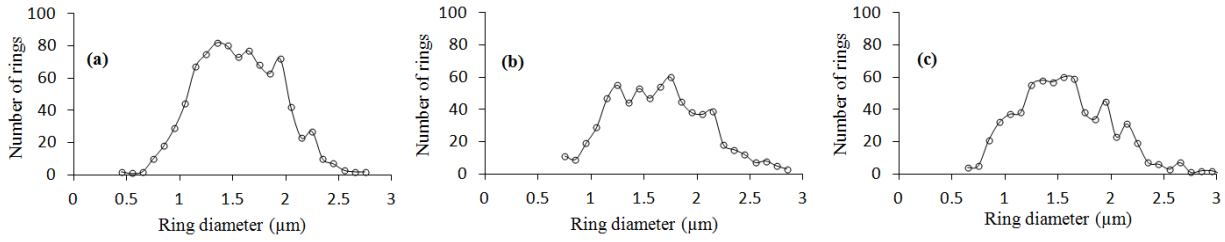

Figure 5.9: Ring size distribution obtained from SEM images of titanium at (a) 214 fs, (b) 714 fs, (c) 3571 fs for 12.6 MHz

From expression 5.9, the laser intensity gradient is related to the ponderomotive force on an electron, which is proportional to the force on plume species [92]. An increase in the pulse duration decreases the laser intensity. A decreases in laser intensity decreases the intensity gradient, which decreases the ponderomotive force. This results in the decrease in ion velocity and the formed ring size [97].

A laser-plasma interaction study showed the rate of energy deposits on a one dimensional plasma (W) can be given by equation 5.12 [100].

$$W = I\,A' \int_0^x K_v\, e^{-K_v x}\, dx \qquad (5.12)$$

Where, $A'$is the cross sectional area of the plasma, and K_v is the absorption coefficient. This shows the energy deposits on the plasma increases with an increase in the laser intensity. This increase in the energy deposit increases the charges in the plasma and also increases the forces on them. Ultimately the size of the formed ring increases with laser intensity.

Silicon shows an obvious drop in the ring size with an increase in the pulse duration (Figure 5.8). An increase in pulse duration decreases the laser intensity as well as its gradient. According to expression 5.9 and equation 5.12 the ring size decreases. Though titanium does not show an apparent drop in the ring size, it could be observed that there is a drop in the peak number of rings with an increase in the pulse duration (Figure 5.9). Again, ionization energy could be playing a key role in minimizing the effect of pulse duration. Table 5.1 shows that the first ionization energies for silicon and titanium are 790 kJ/ mol and 660 kJ/ mol. A minimum threshold of increasing pulse duration may be needed to reach the ionization energy of titanium,

to produce a change in ring size. The change in ring size with pulse duration is again material dependent.

5.3.4 Effect of repetition rate on the ring size at constant power and the pulse energy

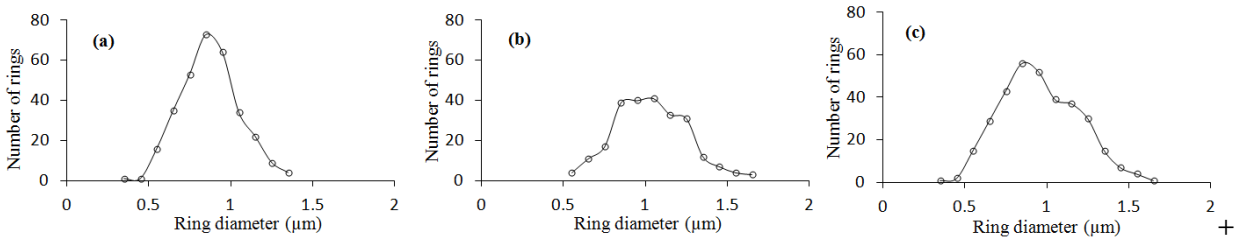

Figure 5.10: Ring size distribution obtained from SEM images of aluminosilicate ceramic for (a) 8.4 MHz (b) 12.6 MHz (c) 25.6 MHz at the constant power of 10.5 W

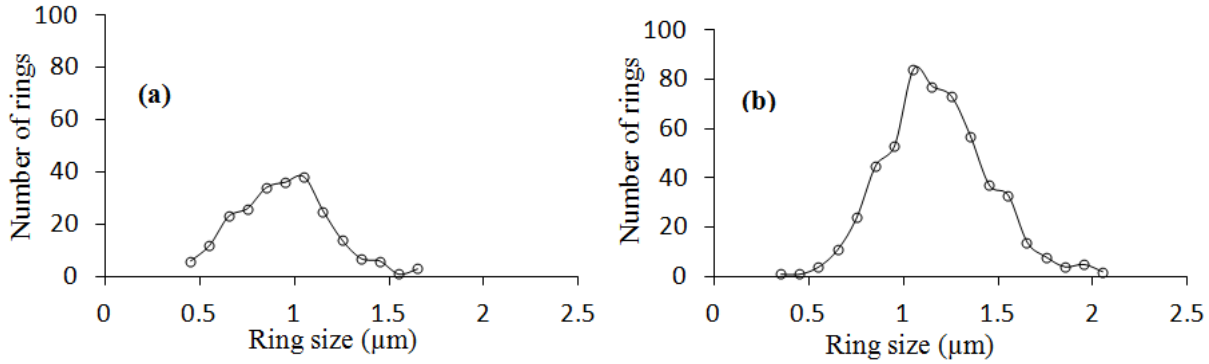

Figure 5.11: Ring size distribution obtained from SEM images of silicon for two different pulse energies where pulse energy at (a) < pulse energy at (b)

Negligible variation in ring size was observed in Figure 5.10 and 5.11. At constant power, an increase in repetition rate decreases the pulse energy and the laser intensity. From expression 5.9 and equation 5.12, the ponderomotive force on electron charges and the energy deposits on the

plasma decreases with the decrease in intensity. However, a noticeable variation in ring size was not observed in Figure 5.10 and 5.11. This could be due to that the variation in intensity was above the ionization threshold of the ceramic.

5.3.5 Effect of background gas on the ring size

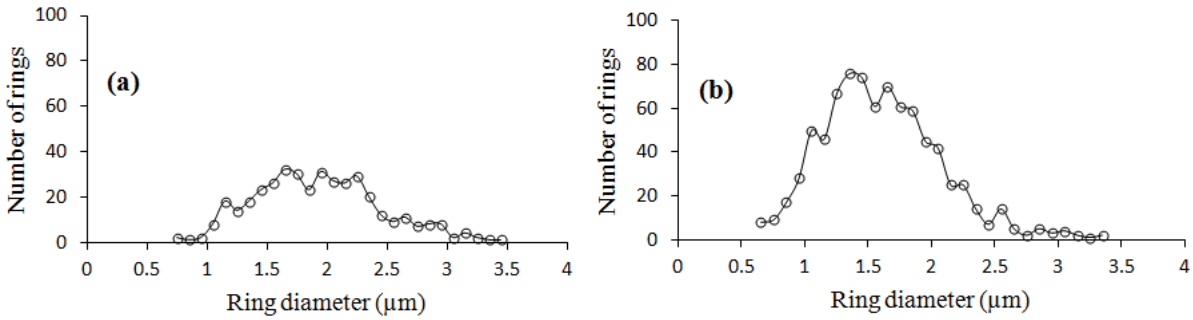

Figure 5.12: Ring size distributions obtained from SEM images of aluminum (a) without background argon gas (b) with background argon gas

A comparison study performed on aluminum with and without background gas in ambient conditions are shown in Figure 5.12. An average ring size of 1.604 µm was obtained with the presence of an additional background gas, whereas it was 1.934 µm without an additional background gas. Presence of background gas produced a drop in the formed ring size. This could be explained using a previous study performed on plasma plume, which had shown that the initial volume of the plasma (V_P) can be expressed by equation 5.13 [100].

$$V_P = v_0 \, \tau \, A \qquad (5.13)$$

Where, v_0 is the initial species velocity, τ is the laser pulse width, and A is the spot area at the target surface. The presence of the background gas can increase the compression pressure on the plume and plasma, which decreases initial volume (V_P) of the plasma

[105]. For the experiments performed, pulse width (τ) and spot size remained at constant. From equation 5.13, a decrease in V_P proportionally decreases the v_0, i.e. the velocity of the species, which decreases the size of the formed ring nanoclusters. Other possible reasons for the decrease in ring size in Figure 5.12 could be the cooling effect of background gas.

5.4 Summary

The ring size is nearly equal to wavelength of the irradiation laser beam and is independent to other laser parameters. This indicates that the laser-induced ponderomotive force on free electrons could have played a predominant role in the formation of ring structures. A detailed analysis suggests that ring size is related to the ionization energies of the ablated material and their molecular weights. Materials of heavier atoms tend to produce smaller rings. Background gas reduces ring size as well. This study provides useful guideline in tailoring the morphology of the particle-agglomerated 3-D nanostructures.

Chapter 6 Study of photon absorption by particle agglomerated 3-D nanostructures

This chapter investigates the size, morphology, and material properties of the particle agglomerated 3-D nanostructures and their influence on photon absorption. The nanostructures fabricated by three different polarized lasers (linear, circular, and elliptical) were used for this analytical study.

6.1 Experimental studies on particle size of 3-D nanostructures

A better understanding of properties of nanostructures and how they affect the photon absorption are the key factors to be considered in selecting nanomaterials for solar cells. Experiments were performed with three different polarized lasers: linear, circular, and elliptical. The laser

parameters such as power, repetition rate and dwell time, were held constant for all three polarized lasers. SEM, TEM, and XRD analyses were performed to identify the variation in morphology, particle size, and material property of the formed nanostructures, respectively. Two different spectrometers were used in analyzing the photon absorption of fabricated nanostructures. The obtained spectrums were analyzed in relation to the size, morphology, and material properties of structures.

6.2 Photon absorption studies on ablated region

The photon absorption study was performed using two different spectrometers. Working spectrum of this spectrometer is limited to visible range. Further it only detects reflected light with limited intensity {refer Figure 6.1 (a)}. However, spectrometer with UV to IR detects spectrums from UV to IR and spectrums with very high intensity.

6.2.1 Study of optical absorption by visible- spectrum spectrometer

An experimental study was performed with an Ocean Optics spectrometer to identify the photon absorption of visible light on 3-D nanostructures fabricated by different polarized ultrafast lasers and on a pure silicon wafer. This study was performed in the reflection mode of spectrometer.

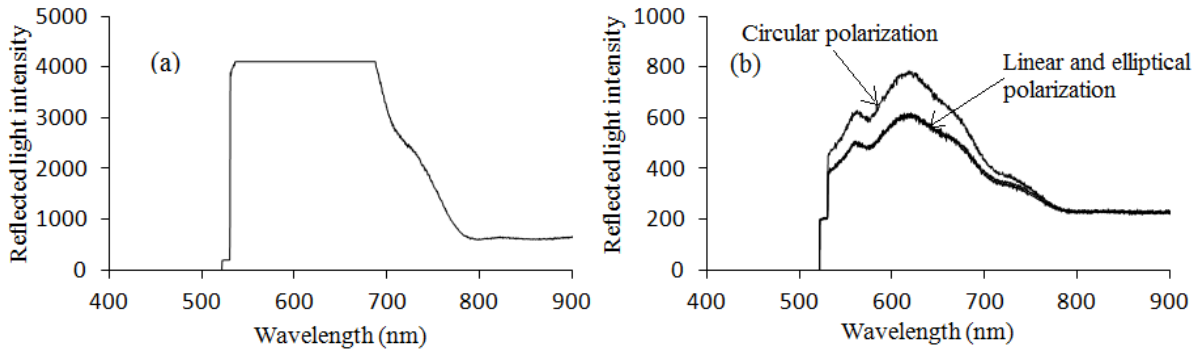

Figure 6.1: Spectrums of reflected light on (a) pure silicon wafer and (b) nanostructures fabricated by different polarized lasers

Figure 6.1 shows the spectrums of the reflected light. Figure 6.1 (a) shows the reflected spectrum obtained on a pure silicon wafer for visible light rays. The intensity of reflected rays was very high in betweem 550 nm and 680 nm, which led to saturate the spectrum. In Figure 6.1 (b), similar spectrums were obtained for structures fabricated by linear and elliptical polarized lasers, where as the intensity of spectrum obtained on structure by circular was slightly higher. These results show the variation in absorption of visible light by structures fabricated by different polarized lasers and the reflection obtained on an unablated silicon wafer.

6.2.2 Study of optical absorption by UV-IR spectrometer

A UV-IR spectrometer was used to study the absorption and reflection spectrums of ultra violet (UV), infra-red (IR), and visible light rays on the fabricated nanostructures. Three sets of lamps were used during the experiments: deuterium for UV range, halogen for visible and IR range, and combined Deuterium – Halogen for the full range from 200 nm to 1100 nm. The results obtained are shown in Figures 6.2 - 6.3. The spectrums in Figure 6.2 show a large drop in the amount of reflected light rays on the ablated region when compared with the spectrums obtained on an un-ablated silicon surface. Especially in UV range (Figures 6.2 (a) and 6.2 (c) from 250

nm to 275 nm), a maximum of ten times saving in reflected light rays was recorded on ablated region with nanostructures when compared with un-ablated silicon surface.

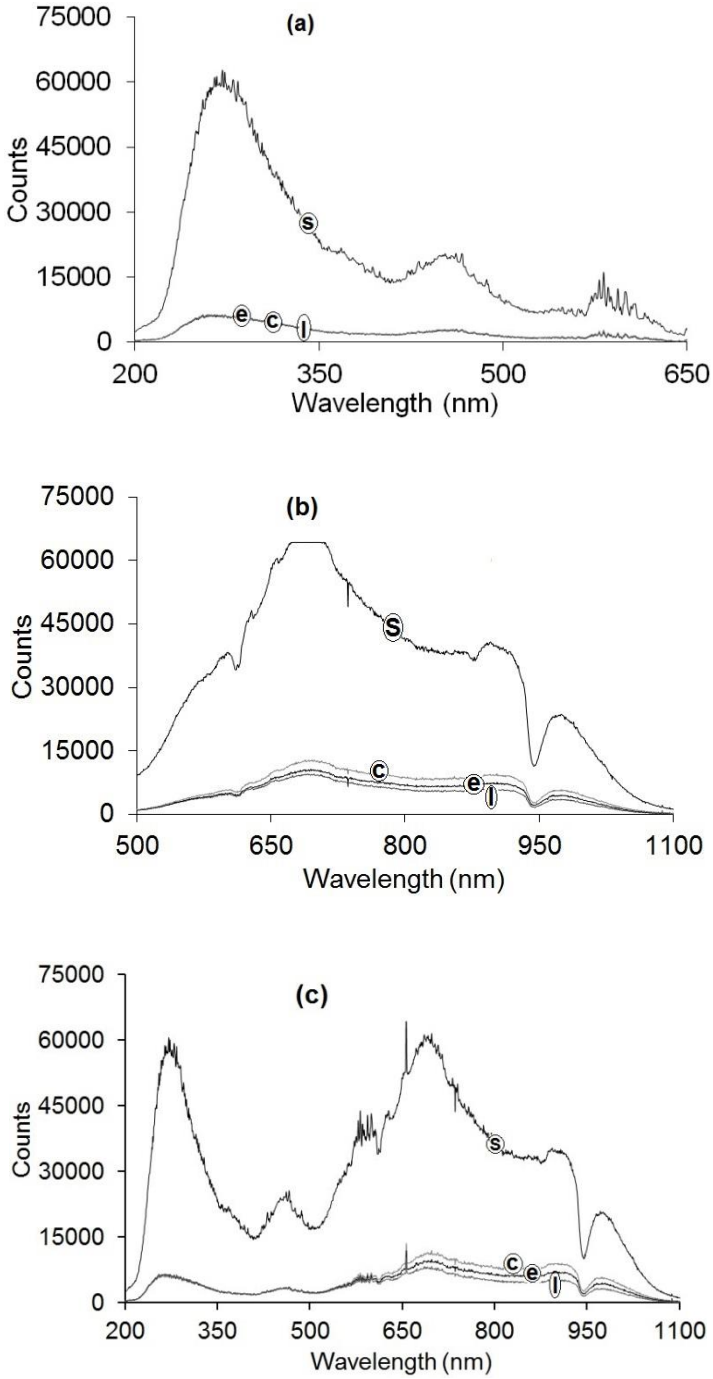

Figure 6.2: The reflected spectrums obtained on 3-D nanostructures for (a) deuterium light rays (b) halogen light rays (c) deuterium- halogen combined light rays, where c - circular polarization, e - elliptical polarization, l - linear polarization, and S - unablated silicon wafer

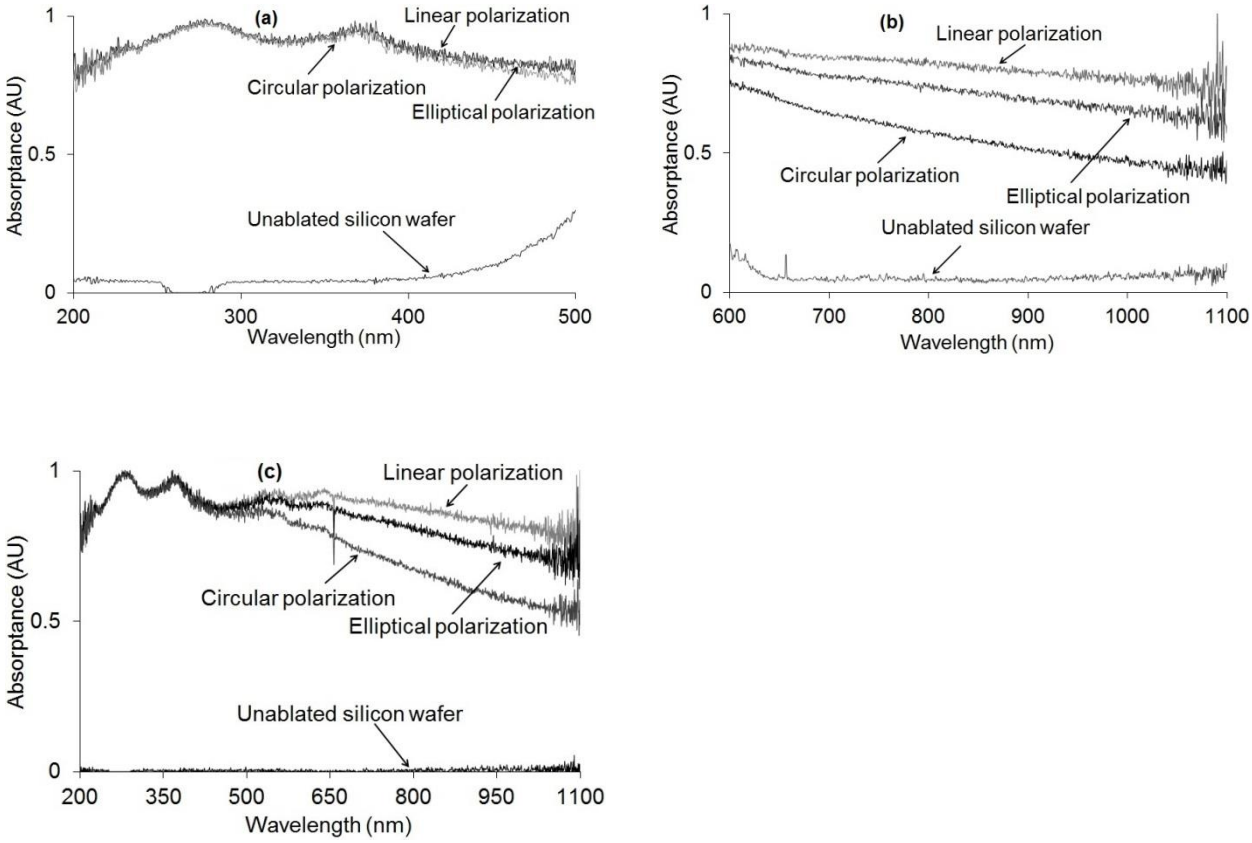

Figure 6.3: The absorption spectrums obtained on 3-D nanostructures for (a) deuterium light rays (b) halogen light rays (c) deuterium- halogen combined light rays

Figure 6.3 shows the comparisons of absorption spectrums obtained on structures fabricated by circular, linear, and elliptical polarized lasers with unablated silicon wafer for UV, IR, and visible spectrums. The ablated region with nanostructures showed highest amount of absorption for UV rays when compared with IR or visible rays. Structures by elliptical and linear polarized lasers reflected less light when compared with circular in the visible spectrum (Figure 6.2). This is further confirmed by the absorption results in Figures 6.3. The same type of results were obtained among nanostructures in IR spectrum (Figures 6.2 (b) - 6.2 (c) and Figures 6.3 (b) -

6.3 (c)), but such a variation was not observed in UV spectrum (Figures 6.2 (a) and Figures 6.3 (a)).

6.3 Structure properties and photon absorption

The influence of size, morphology, and the material phases of fabricated particle agglomerated 3-D nanostructure is analyzed below.

6.3.1 Ring size

The 3-D nanostructures fabricated by different polarized lasers have the ring morphology. The size of rings in nanostructures is expected to influence the photon absorption due to light trapping. The reflected light contains specular and diffuse rays as shown in Figure 6.4 (a) [14]. As shown in Figures 6.4 (a) - 6.4 (c), light rays can be scattered in several directions during their interaction with the rings. This is called diffused reflection. Specular reflection shows the main reflected light path through the ring size, whereas diffuse reflection also occurs at each incident angle of light.

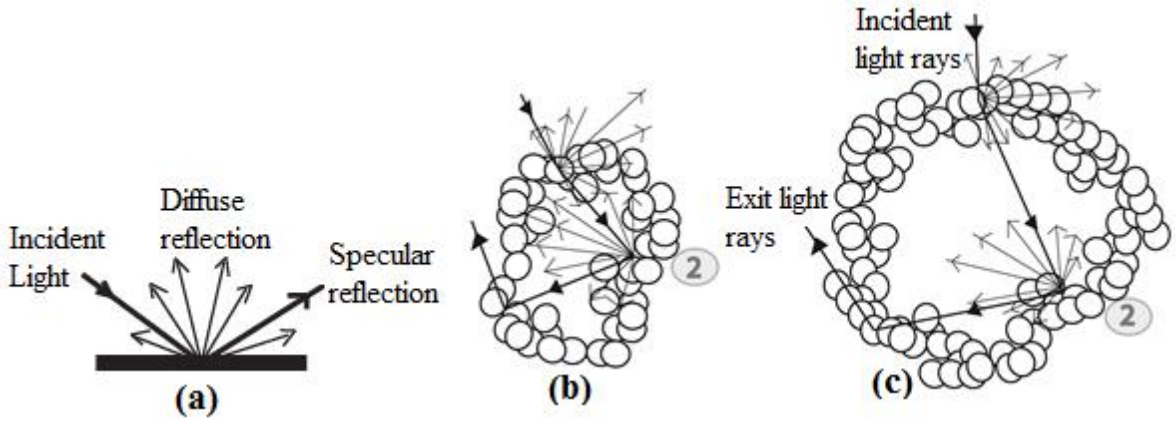

Figure 6.4: Reflected light rays on (a) surface (b) small ring (c) large ring

Decrease in ring size could also increase the surface density of the nanostructure. Therefore, chances of multi interaction of reflected light rays on the remaining portion of the same ring are increased with the decrease in the ring size, which is illustrated in Figures 6.4 (b) - 6.4 (c) (at the interaction point 2). The increased multi interaction increases the number of interaction of light rays further, which results in an enhanced light trapping inside the ring. A survey was carried out on the ring sizes of nanostructures obtained by different polarization to verify the effects of laser polarization on the distribution of ring size. The results are plotted in Figure 6.5.

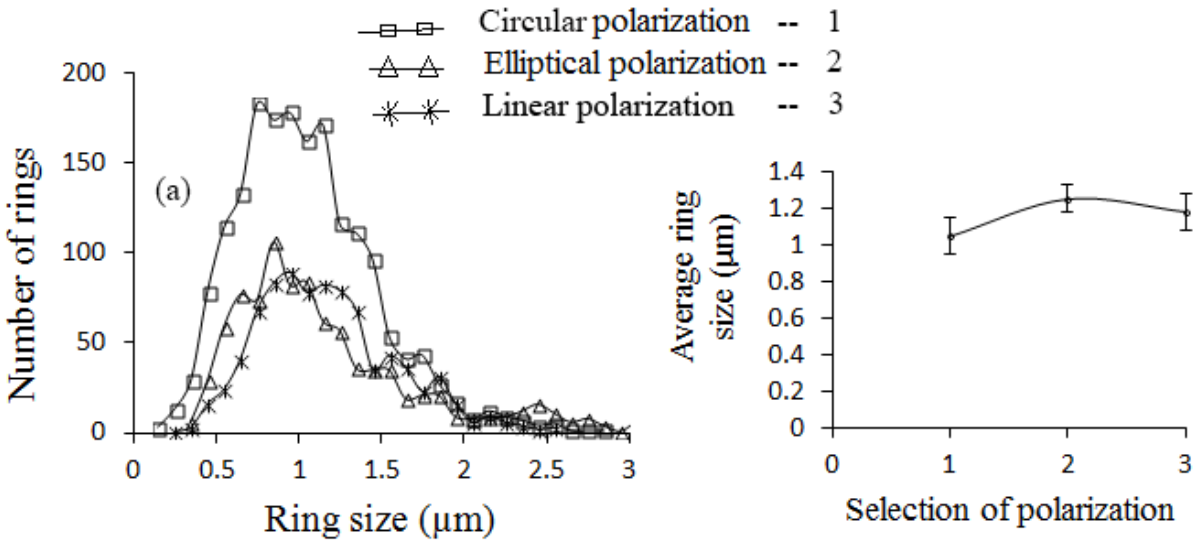

Figure 6.5: For different polarized laser (a) ring size distribution (b) average ring size

For each polarization, more than 1000 ring sizes were manually measured from a minimum of 10 SEM images and the distributions in Figure 6.5 (a) were plotted. For different polarization SEM images showed a maximum error (e) range of ± 100nm in ring size, which was greater than the variation in average ring size in Figure 6.5 (b). This shows that the variation in average ring size falls in the error range. Moreover, a similarity in ring size distributions on Figure 6.5 (a) is

feasible among different polarized laser. These results show that polarized laser has less control over the size of ring in our nanostructures. Hence under our experimental conditions, the ring size has negligible effect on absorption of photon energy by the nanostructures.

The agglomerated particles are randomly oriented. Hence the direction of reflected light is not limited to the plane of the incident ring. The reflected light also randomly oriented. Therefore depth of fabricated nanostructures has a reasonable influence in the photon absorption.

6.3.2 Depth of nanostructures

The depth of formed nanostructure could be shown as overlapping of particle agglomerated ring layers. The number of ring layers could be varied with respect to the conditions of laser ablation and the material of ablation.

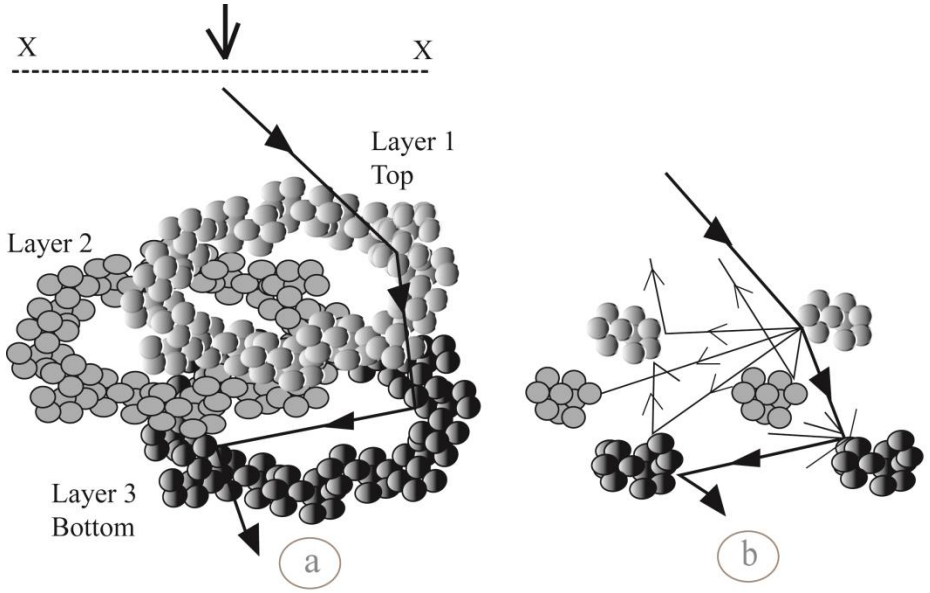

Figure 6.6: Travel of multi reflected light rays along the depth of nanostructure (a) schematic diagram of rings (b) Vertical cross section of rings on plan X-X

Figures 6.6 (a) and 6.6 (b) show a schematic diagram of 3-D nanostructures and a vertical cross section obtained on the X-X plane (shows the cross sectioned particles on opposite diametrical edges of the rings on three different layers) respectively to illustrate the path of light rays along the layers towards the depth of the structure. An incident light ray that travels through the 3-D nanostructure involves multiple reflections as shown in Figure 6.6 (b), which enhance the light trapping and the portion of the light rays could be absorbed during each interaction on the particle of the structure.

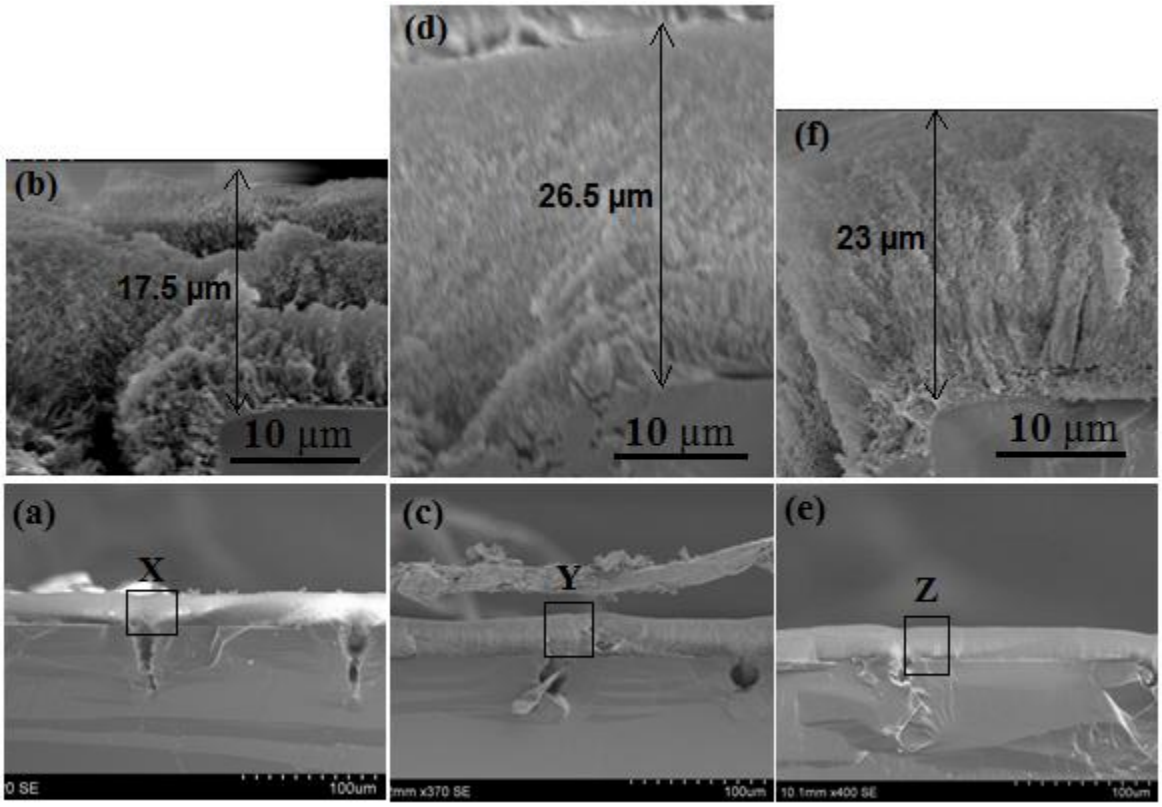

Figure 6.7: SEM images obtained on cross sections of 3-D nanostructures fabricated by different polarized lasers (a) circular, (b) zoomed image on X, (c) elliptical, (d) zoomed image on Y, (e) linear, (f) zoomed image on Z

The increase in the depth of nanostructure or the number of layers in the structure increases the number of reflections or photon trapping as well as the amount of photon absorption. A set of

experiments was performed by different polarization with same repetition rate (25.2MHz), power (11.2W at the target surface), dwell time (0.1ms), and laser scanning map. The cross sections of the fabricated nanostructures were studied under SEM to identify their depth, which are shown in Figures 6.7 (a) - 6.7 (f). The procedure involved in the preparation of cross sections was discussed in section 3.3.3.1.

Figure 6.7 shows that the elliptical and linear polarized lasers have produced a large depth of nanostructures when compared with circular polarized laser. A similarity could be noticeable between the depth of nanostructures in Figure 6.7 and the photon absorption results shown in Figures 6.2 - 6. 3. This shows that the photon absorption could be increased with the increase in the depth of nanostructures [106].

6.3.3 Size of the nanostructure

The photon absorption of nanostructure could be affected by both size of agglomerated particles and the size of the nanocluster. The methods followed to measure these sizes were discussed in section 3.3.2. Size of the nanocluster (string diameter) is determined by the size of the agglomerated particles and the number of particles agglomerated. The following sections show two techniques followed to study the size distributions of both agglomerated nanoparticles and the nanocluster string.

6.3.3.1 Agglomerated particle size

The 3-D nanostructure is made out of agglomerated nanoparticles, which increases the surface area as well as the surface roughness in nanoscale. This nanoscale morphology could also enhance the photon trapping. A particle size study was performed on the TEM images of 3-D

nanostructures obtained by different polarization. The method followed to measure particle size was given in section 3.3.2.2. The results are shown in Figure 6.8.

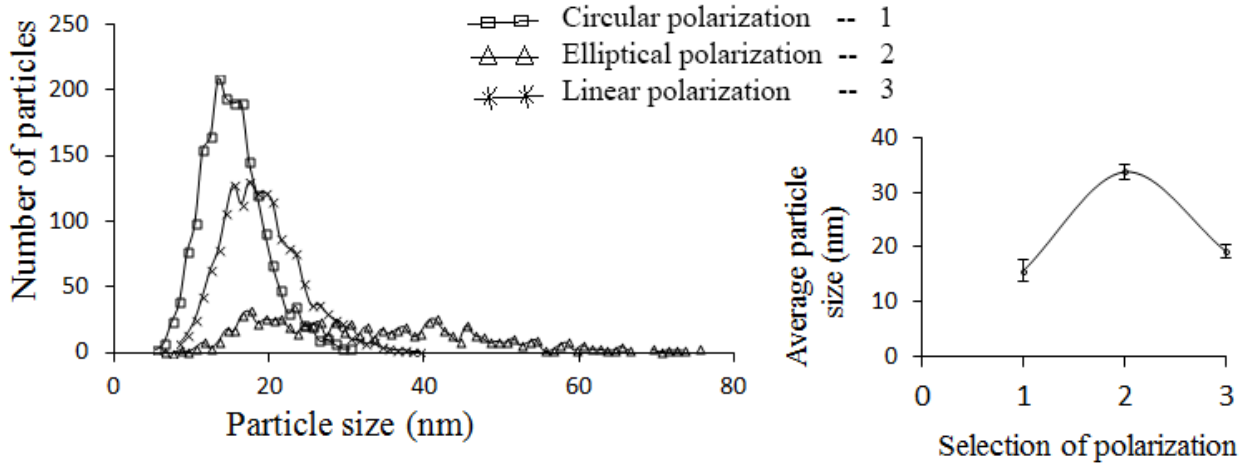

Figure 6.8: Particle size characterization studies on nanostructures fabricated by different polarized ultrafast lasers (a) Particle size distribution (b) Average particle size

Size of particles controls the absorption of photons. The effect of light absorption with particle size and the variation in intensity of light passing through the particle can be given by equation 6.1 [107].

$$I_T = Io\, e^{-\alpha L} \qquad \textbf{(6.1)}$$

Where, Io is the incident light intensity, I_T is the transmitted light intensity, L is the thickness traversed by the light, and α is the absorption coefficient. From equation 6.1, increase in L decrease the intensity of the transmitted light (I_T), i.e. absorption increases with the increase in particle size. Hence in accordance to the distribution and average of particle size in Figures 6.8 (a) - 6.8 (b), nanostructures of elliptical and linear absorb more photons than the structures of circular. These results agree with those in Figure 6.2 – 6.3.

Studies showed that the aspect ratio of nanostructure has a significant control over the light scattering especially for metal particles. For an example, the increase in the ratio of cross section to the length of a nanorod has shown a significant increase in the amount of scattered light [108]. Another study shows that the slightly elongated spherical particles produce huge variation in the scattered light, which increases and reaches a maximum and decreases eventually [109]. Though our structure is mostly from semiconductor oxides, the agglomeration of particles elongates the spherical particles along those radiuses. This should probably affect the scattering potential of the structure. Further agglomeration of smaller particles scatters better than one large particle due to increased surface area [110]. Figure 6.8 (b) shows that the average particle size was in between 15 nm – 33 nm. The agglomeration of these particles could possibly increase the scattering and photon absorption of the fabricated nanostructures.

6.3.3.2 Size of nanocluster

The size of the particle agglomerated structure was studied with nanoparticle tracking analysis. The 3-D nanostructures fabricated by linear polarized femtosecond laser were taken for the study. The structure was separated into water by an ultrasonic vibrator. The particle size concentration in the water was measured in three consequent time intervals, which are shown in Figures 6.9 (a) - 6.9 (c). It could be observed from the distributions, a drop in peak number of concentration was observed from Figure 6.9 (a) to 6.9 (b), whereas the concentration of larger particles increased slightly. This shows the continuous recombination of particles with time. Figure 6.9 (d) shows the average of particle size concentration and their standard deviation is shown in Figure 6.9 (e).

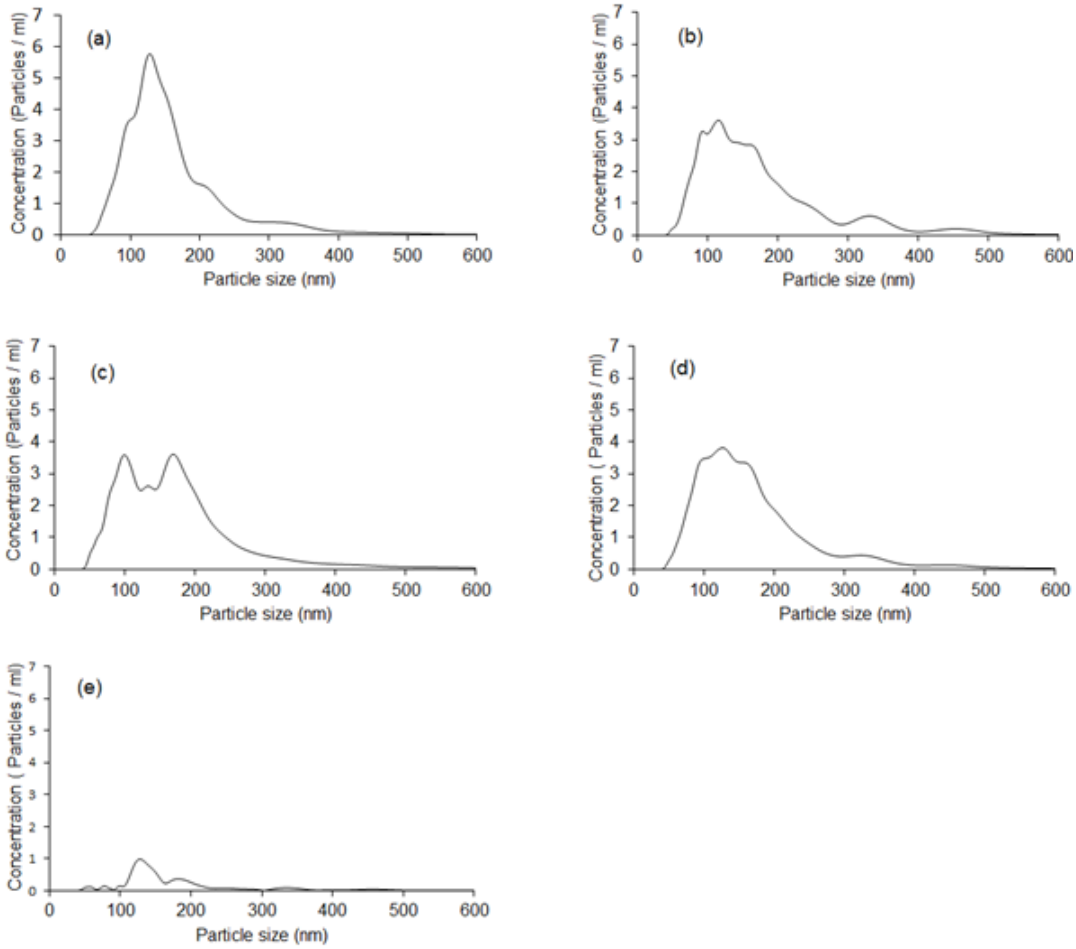

Figure 6.9: (a) to (c) Particle size concentration distributions for 3 consequent time intervals, (d) average of particle size concentration, (e) standard deviation

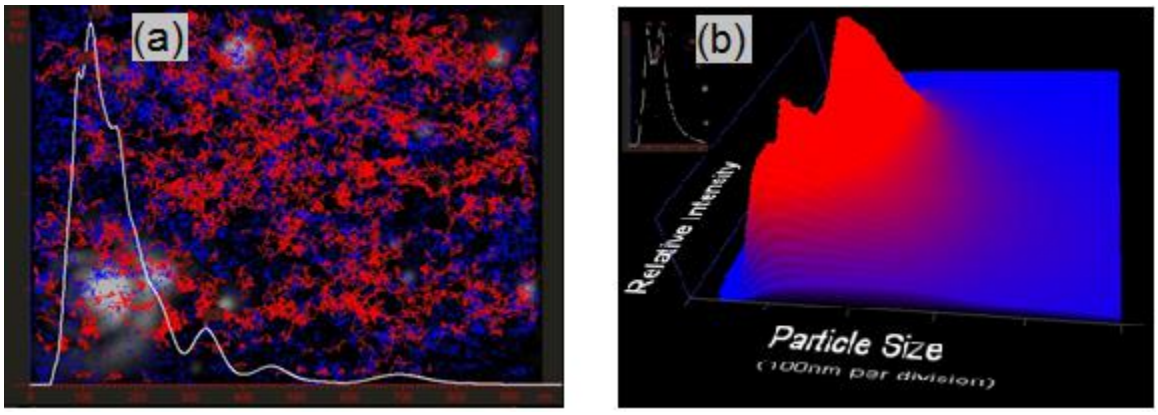

Figure 6.10: (a) Particles movement and their size intensity distribution (b) relative intensity particle size concentration obtained

Figures 6.10 (a) - 6.10 (b) show the real time movement of particles in water and their size intensity distribution curve. The absorptance spectrums in Figure 6.2 (c) and 6.3 (c) show the possible influence of the size of particle agglomerated nanostructure in photon absorption.

6.3.4 Other morphologies

Other than the thickness of nanostructure, disoriented silicon structure obtained just below the 3-D nanostructures, marked as "DS" in Figure 6.11 (a), also could affect the amount of photon absorption. The disoriented structure could be formed due to thermal induced stresses, electrostatic stresses, or thermal diffusion occurred during laser ablation.

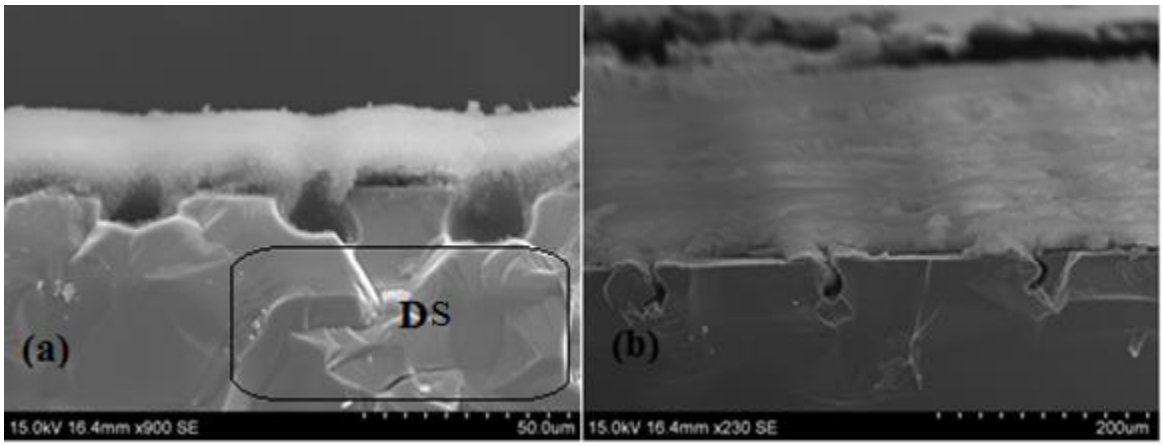

Figure 6.11: SEM images obtained on cross sections of nanostructures (a) enclosed region D shows the disoriented structure along cross section (b) Angled view of top wavy surface on nanostructure

The size of this disoriented structure could be influenced by the laser operating conditions, laser scanning map, and electro-thermal properties of the ablated materials [111]. The produced disoriented structure decreases the crystallinity of the silicon wafer in long range and increases its amorphous state, which could increase the photon absorption [111]. The wavy top surface obtained on the 3-D nanostructures, shown in Figure 6.11 (b), also increases the photon trapping, which is illustrated in Figure 6.12.

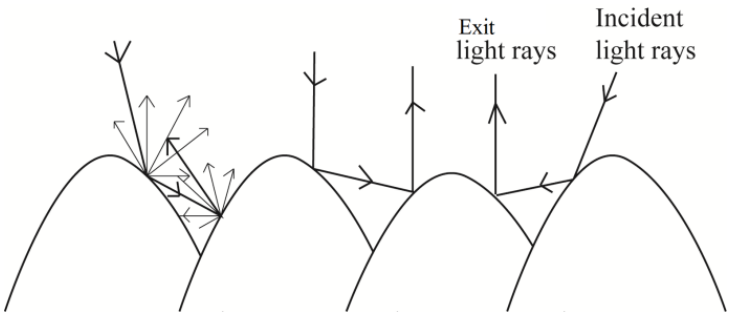

Figure 6.12: Wavy top surface of nanostructures

The incident rays reflect and interact on the very next wavy feature of the top surface. This could be considered as light trapping due to micromorphology of the structure. In this context, the top wavy surface of the structure functions as the front texture for light trapping [112]. The overlapping distance of the wavy feature could be varied by varying the laser power, dwell time or speed of ablation, and the laser scanning map.

6.3.5 Material Phases

6.3.5.1 XRD Analysis

X- ray diffraction analysis (XRD) was performed on the nanostructures fabricated by different polarization. The results obtained are shown in Figures 6.13 (a) - 6.13 (c). Four main peaks were obtained for crystalline silicon i.e. **B** - Si 111, **C**- Si 200, **D** - Si 220, and **E** - Si 311. Frames collected from samples showed that the **B** and **C** were defect peaks from the substrate (Figure 6.14). A shallow broad peak (**A**) was obtained in Figure 6.13 at the 2θ diffraction angle of 22˚ (approximately) could be from amorphous oxides on the ablated area.

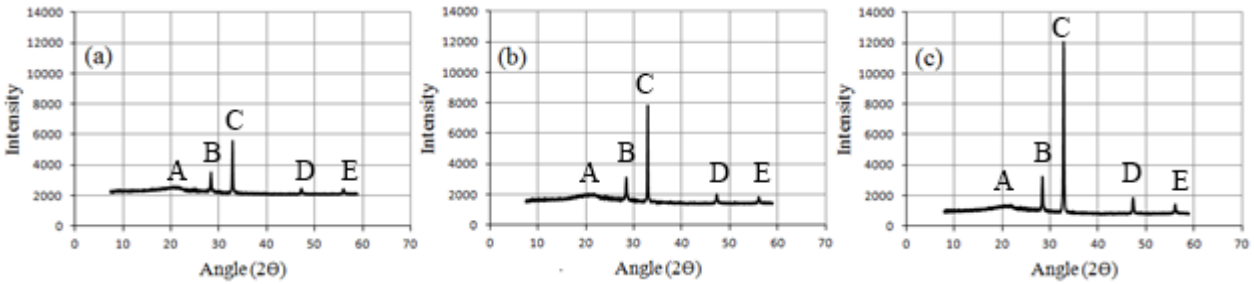

Figure 6.13: X-Ray diffraction analysis on nanostructures fabricated by different polarized lasers (a) circular (b) elliptical (c) linear

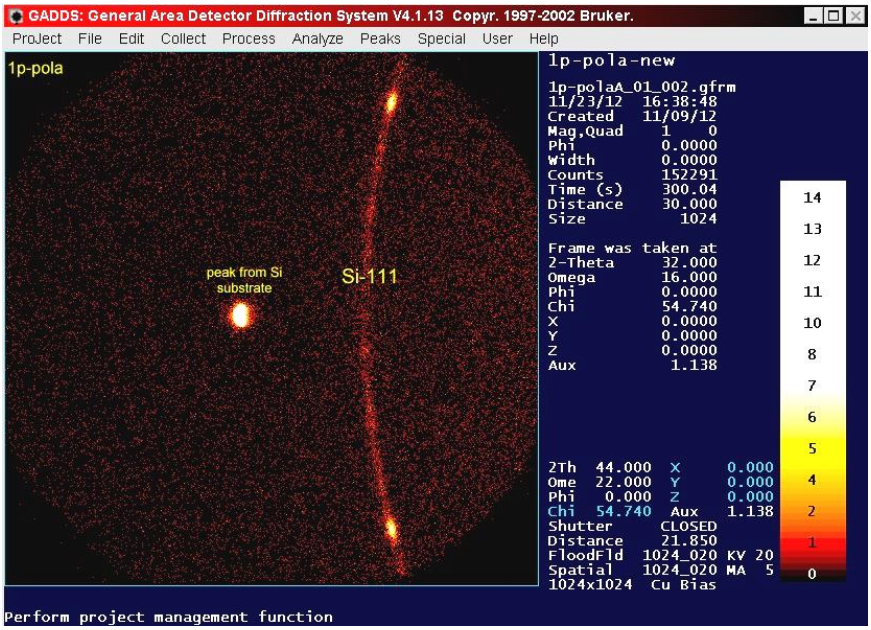

Figure 6.14: A frame collected from sample 1p-pola showing Si-111 peak and Si-200 defect peak coming from the substrate

The above XRD study shows the presence of identical phases of crystalline silicon on the fabricated nanostructures by different polarized lasers. Further, it shows the presence of amorphous phases but the ratio of their presence could not be clearly verified by the XRD analysis. Further material characterization studies were performed on the fabricated nanostructures using a scanning electron microscopy coupled with energy dispersive x-ray (SEM-EDX) to analyze the presence of elements.

6.3.5.2 SEM-EDX analysis

For the purpose of comparing the element ratios obtained on nanostructures, the SEM-EDX was performed. Figure 6.15 shows the line scans obtained along the cross sections of fabricated nanostructures by different polarized lasers. Table 6.1 shows the element ratios in nanostructures generated by circular, elliptical, and linear polarized lasers.

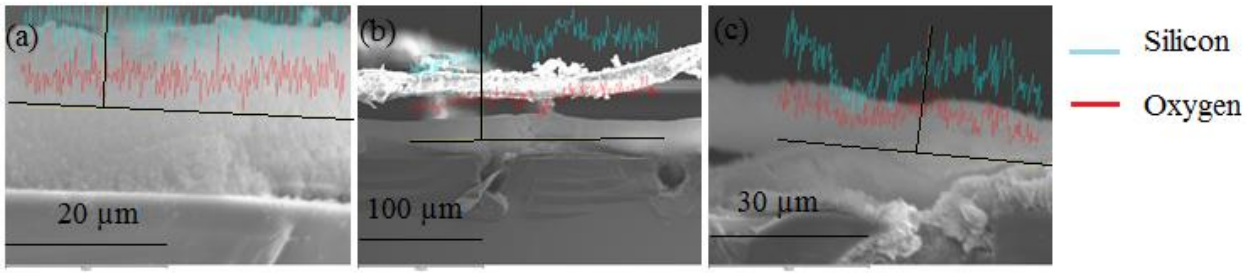

Figure 6.15: Line scan of SEM-EDX along the cross section of nanostructures by different polarized lasers (a) circular (b) elliptical (c) linear

Table 6.1: Element ratios obtained from SEM-EDX along the cross section of nanostructures by different polarized ultrafast lasers (a) circular (b) elliptical (c) linear

Polarization	Element ratio	
	Silicon	Oxygen
Circular polarization	55.32	44.68
Elliptical polarization	48.24	51.76
Linear polarization	49.61	50.39

The results in Figure 6.15 and Table 6.1 show that the presence of high ratio of oxides in the nanostructures when compared with crystalline silicon phases as shown in Figure 6.13. The oxides were amorphous and not visible in the XRD peaks. Table 6.1 shows that the nanostructures by elliptical and linear polarized lasers produced high ratio of oxides when

compared with circular. The SEM-EDX results in the Table 6.1 shows a very close relationship with the results in the Figure 6.1 - 6.3, i.e. amorphous structure absorbs high amount of photons when compared with those from crystalline.

All above studies showed the effects of micro and nano morphologies and the variation in material phases generated by different polarized lasers in light trapping and photon absorption. However the variation in photon absorption is not limited by one factor. Mostly it could be combined effects of several factors discussed above or more. With respect to these experimental results, depth of nanostructures, particle size, and formed material phases could have played key roles in determining the absorption of light.

6.4 Summary

This study showed the unique micro and nano morphologies of fabricated particle agglomerated 3-D nanostructures in enhancing the photon absorption. Nanostructures were fabricated with different polarized ultrafast lasers i.e. elliptical, circular, and linear. These nanostructures were studied under the spectrometer for visible light absorption. Identical distributions of reflected light with varying intensity were produced along wavelength on the nanostructures. Compared with other reported nanostructures, the particle agglomerated 3-D nanostructure show a broad absorption spectrum, from 200 nm 1100nm. Silicon nanomaterials usually demonstrate increased absorption in the visible spectrum, while Titanium dioxide nanomaterial only capable of harvest UV light. The broad bandwidth of the particle agglomerated 3-D nanostructure has the potential of providing higher photovoltaic efficiency.

Particle size, ring size and other morphology characteristics of the particle agglomerated 3-D nanostructures, all play a role in determining the light absorptance. Nanostructures by linear and elliptical polarized lasers showed increase in visible light absorption within the range of 550 nm - 750 nm than those from circular polarized. The measurement studies performed on images of nanostructures fabricated with different polarized lasers showed that the particle size and depth of nanostructure influenced the photon absorption. XRD and SEM-EDX studies performed on nanostructures showed that the presence of amorphous phase oxides could also influence the photon absorption. Further the presence of top wavy surface and the amorphous state of material just below the nanostructures could help to increase the solar absorption through photon trapping.

Chapter 7 Summary and Contributions

This thesis reported an in-depth study of the particle-agglomerated 3-D nanostructures generated by femtosecond laser ablative synthesis. The morphology of the nanostructure is strongly related to the laser parameter. The particle-agglomerated 3-D nanostructures demonstrated strong absorption in the spectrum of 200 - 1100 nm, which imply its potential application in photovoltaic applications. The absorptance is found to be strongly dependent on the dimensions and morphology of the particle-agglomerated 3-D nanostructures.

Nanostructures attracted tremendous research interest for their potentials in the mass production of low-cost solar cells. Silicon and titanium are the two most investigated materials for this purpose. Silicon-based nanostructures show high absorptance in the visible spectrum of sun light. On the other hand, titanium based nanostructures are investigated for their high absorptance in the UV range. They can be used as an additional light harvest material to broaden the absorption spectrum of a solar cell. In contrast, the particle-agglomerated 3-D nanostructures synthesized by femtosecond laser ablation of solid targets demonstrated strong absorption in the

spectrum of 200 - 1100 nm. The broad absorption spectrum implies high photovoltaic conversion efficiency.

Vapor condensation is the main mechanism responsible for the formation of the nanoparticles agglomerated 3-D nanostructures. The particle size is less than 100 nm and the nanoparticles assemble into chains and rings that are interconnected and intertwined. An explanation model was formed to predict the size of agglomerated particles in the 3-D nanostructures, through an experimental-analytical study. It is found that average size of nanoparticles varies with repetition rates and fluence ratio. Particle size distribution follows either a unimodal or a bimodal, dependent on the fluency of the laser irradiation. There is a model transition fluence, at which the distribution model transits from unimodal to bimodal.

A mechanism was suggested to explain the formation of ring nanocluster based on the laser pulse-plume interaction and its influence on dynamics of plume species. It was found that the size of the ring is approximately equal to the wavelength of the incident laser beam. The results in wavelength studies confirm the presence of ponderomotive force in the ring generation. Ring size also showed a close relationship with other laser parameters: pulse duration, pulse energy, and repetition rate. An increase in the pulse duration led to decrease the formed ring size. An increase in pulse energy led to increase the ring size. All these experiments proved the presence of a laser intensity dependent force that controls the ring size. Several sets of experiments were performed on metals, alloys, semiconductors, ceramics, and glasses to verify the influence of material properties, laser parameters, and the background gas on the ring size. The material properties, i.e. ionization energy and molecular weight of the ablated material, showed a close relationship with ring size. An increase in the ionization energy and molecular weight led to decrease the ring size. The presence of a background gas reduces ring size. The additional

cooling and the added atmosphere pressure on the plume species slow down the particle motion, therefore, a smaller ring size.

Photon absorption characteristics of the nanoparicle-agglomerated 3-D nanostructures were studied in relation to the particle size and ring sizes. An increase in particle size increases the photon absorption, whereas a decrease in ring size increases the photon trapping through increased number of interactions of light with structure. Further, the property of vast particle size distribution in structure and the agglomerated structure size help to increase the broadband of the photon absorption.

Many attributes contribute to the enhancement of the light absorption. The nanostructure contains diverse particle size. The presence of broad range of particle size increases bandwidth (efficiency across wavelength spectrum) of the absorption. The ring structure is made out of nanoscale agglomerated particles. The agglomerated particles functions as the self-scattering agent to the structure. Therefore it is not necessary to use an additional scattering agent to increase the photon absorption. The agglomeration of particles gives an elongated spherical morphology to the particles. It enhances the scattering property of the structure and increases the photon absorption in nanosolar cells. The top surface of the fabricated nanostructure has a wavy morphology, which increases the interaction of reflected light on the structure and the amount of photon absorbed.

The 3D nanostructure showed a minimum absorption of 0.75 A.U. in the bandwidth from UV to IR. To the best of the author's knowledge, it is a very competitive absorption rate compared with the previous nanostructures used in photovoltaic conversion. The 3D nanostructure is easy to

fabricate. The photon absorption property of the structure can be modified by particle and ring sizes, which can be altered by adjusting laser parameters.

The main contributions of this research thesis are highlighted as follows:

1. Formed an explanation to predict particle size in 3-D nanostructures
2. Identified the unimodal to bimodal transition of particle size distributions
3. Proposed a mechanism for the ring nanocluster formation and identified the factors determine the ring size
4. Proposed and verified properties of 3-D nanostructures influencing the photon absorption

The possible future works that could be performed from the experimental results obtained in this research are as follows:

1. Formation of an empirical formula to predict the particle size and ring size with laser parameters
2. Optimization of structure morphologies to enhance the photon absorption
3. In depth analysis of effect of each structure morphologies, for an example agglomerated particles, and their effect on photon absorption

Appendix A

List of Publications (Refereed Journals)

1) "Effect of mega-hertz repetition rate on the agglomerated particle size of femtosecond synthesized nanostructures", Mugunthan Sivayoganathan, Bo Tan, and Krishnan Venkatakrishnan, Optical Materials Express, Vol. 2, Issue 8, pp. 987-995 (2012). Doi: 10.1364/OME.2.000987.

2) "Synthesis of crystalline and amorphous, particle-agglomerated 3-D nanostructures of Al and Si oxides by femtosecond laser and the prediction of these particle sizes", Mugunthan Sivayoganathan, Bo Tan, and Krishnan Venkatakrishnan, Nanoscale Research Letters, Vol. 7, Issue 1, (2012). Doi: 10.1186/1556-276X-7-619

3) "Formation of ring-patterned nanoclusters by laser–plume interaction", Mugunthan Sivayoganathan, Bo Tan, and Krishnan Venkatakrishnan, Journal of Nanoparticle Research Letters, Vol. 15, Issue 1386, (2013). Doi: 10.1007/s11051-012-1386-3.

Summary of experimental Results

Table A. 1: Experimental results on particle size

Fluence ratio = 3.2 , Dwell time = 0.1 ms		Laser power = 10.5 W, Dwell time = 0.1 ms		repetition rate = 25.2 MHz, Dwell time = 0.1 ms	
Repetition rate / (MHz)	Average particle size / (nm)	Repetition rate / (MHz)	Average particle size / (nm)	Fluence ratio	Average particle size / (nm)
4.2	21.75	2.1	24	1.6	10.62
6.3	19.1	8.4	20.5	2	13.51
8.4	17	12.6	17.1	2.4	17.61
12.6	18.51	25.2	12.52	2.8	18.56
25.2	24.51	-	-	3.2	19.35

Table A. 2: Experimental data on ring size

Silicon						Titanium	
12.6 MHz, 10.5 W, 0.1 ms				Laser power = 10.5 W, Dwell time = 0.1 ms		12.6 MHz, 10.5 W, 0.1 ms	
Pulse duration / (fs)	Peak ring size / (nm)	wavelength / (nm)	peak ring size / (nm)	Repetition rate / (MHz)	peak ring size / (nm)	Pulse duration / (fs)	peak ring size / (nm)
300	950	1030	1020	8.4	930	214	1505
1000	850	1030 and 515	525 and 1030 (distorted)	12.6	1010	714	1528
5000	700	-	-	25.2	950	3571	1501

Reference

[1] P. Yang, K. Kawasaki, M. Ando, and N. Murase, "Au/SiO 2/QD core/shell/shell nanostructures with plasmonic-enhanced photoluminescence," *Journal of Nanoparticle Research*, vol. 14, no. 9, pp. 1–11, 2012.

[2] G. Sagarzazu, K. Inoue, M. Saruyama, M. Sakamoto, T. Teranishi, S. Masuo, and N. Tamai, "Ultrafast dynamics and single particle spectroscopy of Au–CdSe nanorods," *Physical Chemistry Chemical Physics*, vol. 15, no. 6, p. 2141, 2013.

[3] S. Ameen, M. S. Akhtar, H.-K. Seo, Y. S. Kim, and H. S. Shin, "Influence of Sn doping on ZnO nanostructures from nanoparticles to spindle shape and their photoelectrochemical properties for dye sensitized solar cells," *Chemical Engineering Journal*, 2012.

[4] J. Conradt, J. Sartor, C. Thiele, F. Maier-Flaig, J. Fallert, H. Kalt, R. Schneider, M. Fotouhi, P. Pfundstein, and V. Zibat, "Catalyst-Free Growth of Zinc Oxide Nanorod Arrays on Sputtered Aluminum-Doped Zinc Oxide for Photovoltaic Applications," *The Journal of Physical Chemistry C*, vol. 115, no. 9, pp. 3539–3543, 2011.

[5] P. Atienzar, T. Ishwara, B. N. Illy, M. P. Ryan, B. C. O'Regan, J. R. Durrant, and J. Nelson, "Control of photocurrent generation in polymer/ZnO nanorod solar cells by using a solution-processed TiO2 overlayer," *The Journal of Physical Chemistry Letters*, vol. 1, no. 4, pp. 708–713, 2010.

[6] G. Jimenez-Cadena, E. Comini, M. Ferroni, A. Vomiero, and G. Sberveglieri, "Synthesis of different ZnO nanostructures by modified PVD process and potential use for dye-sensitized solar cells," *Materials Chemistry and Physics*, vol. 124, no. 1, pp. 694–698, 2010.

[7] A. Prasad, "Functional zinc oxide nanostructures for electronic and energy applications," 2011.

[8] A. Kongkanand, K. Tvrdy, K. Takechi, M. Kuno, and P. V. Kamat, "Quantum dot solar cells. Tuning photoresponse through size and shape control of CdSe-TiO2 architecture," *Journal of the American Chemical Society*, vol. 130, no. 12, pp. 4007–4015, 2008.

[9] S. Dayal, N. Kopidakis, D. C. Olson, D. S. Ginley, and G. Rumbles, "Photovoltaic devices with a low band gap polymer and CdSe nanostructures exceeding 3% efficiency," *Nano letters*, vol. 10, no. 1, pp. 239–242, 2009.

[10] B. Farrow and P. V. Kamat, "CdSe quantum dot sensitized solar cells. Shuttling electrons through stacked carbon nanocups," *Journal of the American Chemical Society*, vol. 131, no. 31, pp. 11124–11131, 2009.

[11] L. Zhang, Y. Jia, S. Wang, Z. Li, C. Ji, J. Wei, H. Zhu, K. Wang, D. Wu, and E. Shi, "Carbon nanotube and CdSe nanobelt Schottky junction solar cells," *Nano letters*, vol. 10, no. 9, pp. 3583–3589, 2010.

[12] B. M. Kayes, H. A. Atwater, and N. S. Lewis, "Comparison of the device physics principles of planar and radial< equation> pn</equation> junction nanorod solar cells," *Journal of Applied Physics*, vol. 97, no. 11, pp. 114302–114302, 2005.
[13] J. H. Lee, J. H. Park, J. S. Kim, D. Y. Lee, and K. Cho, "High efficiency polymer solar cells with wet deposited plasmonic gold nanodots," *Organic Electronics*, vol. 10, no. 3, pp. 416–420, 2009.
[14] E. Moulin, J. Sukmanowski, P. Luo, R. Carius, F. X. Royer, and H. Stiebig, "Improved light absorption in thin-film silicon solar cells by integration of silver nanoparticles," *Journal of Non-Crystalline Solids*, vol. 354, no. 19, pp. 2488–2491, 2008.
[15] A. M. Funde, N. A. Bakr, D. K. Kamble, R. R. Hawaldar, D. P. Amalnerkar, and S. R. Jadkar, "Influence of hydrogen dilution on structural, electrical and optical properties of hydrogenated nanocrystalline silicon (nc-Si: H) thin films prepared by plasma enhanced chemical vapour deposition (PE-CVD)," *Solar Energy Materials and Solar Cells*, vol. 92, no. 10, pp. 1217–1223, 2008.
[16] J. D. Holmes, K. P. Johnston, R. C. Doty, and B. A. Korgel, "Control of thickness and orientation of solution-grown silicon nanowires," *Science*, vol. 287, no. 5457, pp. 1471–1473, 2000.
[17] E. Garnett and P. Yang, "Light trapping in silicon nanowire solar cells," *Nano letters*, vol. 10, no. 3, pp. 1082–1087, 2010.
[18] W. Wang, S. Wu, K. Reinhardt, Y. Lu, and S. Chen, "Broadband light absorption enhancement in thin-film silicon solar cells," *Nano letters*, vol. 10, no. 6, pp. 2012–2018, 2010.
[19] O. Gunawan, K. Wang, B. Fallahazad, Y. Zhang, E. Tutuc, and S. Guha, "High performance wire-array silicon solar cells," *Progress in Photovoltaics: Research and Applications*, vol. 19, no. 3, pp. 307–312, 2011.
[20] Y. A. Akimov, K. Ostrikov, and E. P. Li, "Surface plasmon enhancement of optical absorption in thin-film silicon solar cells," *Plasmonics*, vol. 4, no. 2, pp. 107–113, 2009.
[21] M. A. Green, K. Emery, Y. Hishikawa, W. Warta, and E. D. Dunlop, "Solar cell efficiency tables (version 39)," *Progress in Photovoltaics: Research and Applications*, vol. 20, no. 1, pp. 12–20, 2012.
[22] J. Zhu, J.-N. Ding, and L.-Q. Guo, "A new silicon nanowire arrays solar cell based on gradient optical gaps nanometre thin film," *International Journal of Materials and Structural Integrity*, vol. 6, no. 2, pp. 297–308, 2012.
[23] J. Zhu, Z. Yu, G. F. Burkhard, C.-M. Hsu, S. T. Connor, Y. Xu, Q. Wang, M. McGehee, S. Fan, and Y. Cui, "Optical absorption enhancement in amorphous silicon nanowire and nanocone arrays," *Nano Letters*, vol. 9, no. 1, pp. 279–282, 2008.
[24] B. O'Donnell, L. Yu, M. Foldyna, and P. Roca i Cabarrocas, "Silicon nanowire solar cells grown by PECVD," *Journal of Non-Crystalline Solids*, 2011.
[25] S. Bu, X. Li, L. Wen, X. Zeng, Y. Zhao, W. Wang, and Y. Wang, "Optical and electrical simulations of two-junction III-V nanowires on Si solar cell," *Applied Physics Letters*, vol. 102, no. 3, pp. 031106–031106, 2013.
[26] X. Xie, X. Zeng, P. Yang, C. Wang, and Q. Wang, "< i> In situ</i> formation of indium catalysts to synthesize crystalline silicon nanowires on flexible stainless steel substrates by PECVD," *Journal of Crystal Growth*, 2012.
[27] R. Ren, Y. Guo, and R. Zhu, "Design of plasmonic back reflector for silicon nanowire decorated solar cell."

[28] T.-W. Ho and F. C.-N. Hong, “A Reliable Method to Grow Ordered-Arrays of Silicon Nanowires by a Novel Ramp-Cooling Process,” *Applied Surface Science*, 2012.
[29] L. Li, K.-Q. Peng, B. Hu, X. Wang, Y. Hu, X.-L. Wu, and S.-T. Lee, “Broadband optical absorption enhancement in silicon nanofunnel arrays for photovoltaic applications,” *Applied Physics Letters*, vol. 100, no. 22, pp. 223902–223902, 2012.
[30] S.-F. Leung, M. Yu, Q. Lin, K. Kwon, K.-L. Ching, L. Gu, K. Yu, and Z. Fan, “Efficient Photon Capturing with Ordered Three-Dimensional Nanowell Arrays,” *Nano letters*, vol. 12, no. 7, pp. 3682–3689, 2012.
[31] K. X. Wang, Z. Yu, V. Liu, Y. Cui, and S. Fan, “Absorption enhancement in ultrathin crystalline silicon solar cells with antireflection and light-trapping nanocone gratings,” *Nano letters*, vol. 12, no. 3, pp. 1616–1619, 2012.
[32] A. Mavrokefalos, S. E. Han, S. Yerci, M. S. Branham, and G. Chen, “Efficient Light Trapping in Inverted Nanopyramid Thin Crystalline Silicon Membranes for Solar Cell Applications,” *Nano letters*, vol. 12, no. 6, pp. 2792–2796, 2012.
[33] S. E. Han and G. Chen, “Toward the Lambertian limit of light trapping in thin nanostructured silicon solar cells,” *Nano letters*, vol. 10, no. 11, pp. 4692–4696, 2010.
[34] O. K. Varghese, M. Paulose, and C. A. Grimes, “Long vertically aligned titania nanotubes on transparent conducting oxide for highly efficient solar cells,” *Nature nanotechnology*, vol. 4, no. 9, pp. 592–597, 2009.
[35] C. H. Chen, J. Shieh, S. M. Hsieh, C. L. Kuo, and H. Y. Liao, “Architecture, optical absorption, and photocurrent response of oxygen-deficient mixed-phase titania nanostructures,” *Acta Materialia*, 2012.
[36] R. Zhang, A. A. Elzatahry, S. S. Al-Deyab, and D. Zhao, “Mesoporous titania: From synthesis to application,” *Nano Today*, 2012.
[37] G. Edman Jonsson, H. Fredriksson, R. Sellappan, and D. Chakarov, “Nanostructures for enhanced light absorption in solar energy devices,” *International Journal of Photoenergy*, vol. 2011, 2011.
[38] Y. Mao, W. Li, X. Sun, Y. Ma, J. Xia, Y. Zhao, X. Lu, J. Gan, Z. Liu, and J. Chen, “Room-temperature ferromagnetism in hierarchically branched MoO3 nanostructures,” *CrystEngComm*, vol. 14, no. 4, pp. 1419–1424, 2012.
[39] T. Mokari, P. Rukenstein, I. Jen-La Plante, M. Diab, E. Chockler, K. Flomin, and B. Moshofsky, “Selective Growth of Metal Sulfide Tips onto Cadmium Chalcogenide Nanostructures,” *CrystEngComm*, 2012.
[40] D. M. Eisele, C. W. Cone, E. A. Bloemsma, S. M. Vlaming, C. G. F. van der Kwaak, R. J. Silbey, M. G. Bawendi, J. Knoester, J. P. Rabe, and D. V. Bout, “Utilizing redox-chemistry to elucidate the nature of exciton transitions in supramolecular dye nanotubes,” *Nature Chemistry*, 2012.
[41] M. Sivakumar, K. Venkatakrishnan, and B. Tan, “Characterization of MHz pulse repetition rate femtosecond laser-irradiated gold-coated silicon surfaces,” *Nanoscale research letters*, vol. 6, no. 1, pp. 1–5, 2011.
[42] M. Sivakumar, K. Venkatakrishnan, and B. Tan, “Study of metallic fibrous nanoparticle aggregate produced using femtosecond laser radiation under ambient conditions,” *Nanotechnology*, vol. 21, no. 22, p. 225601, 2010.
[43] B. Tan and K. Venkatakrishnan, “Synthesis of fibrous nanoparticle aggregates by femtosecond laser ablation in air,” *Optics express*, vol. 17, no. 2, pp. 1064–1069, 2009.

[44] H. Selvaraj, B. Tan, and K. Venkatakrishnan, "Synthesis of nanofiber-filled polydimethylsiloxane using ultrafast laser irradiation," *Journal of Polymer Research*, vol. 18, no. 6, pp. 1659–1665, 2011.
[45] A. S. Mahmood, K. Venkatakrishnan, B. Tan, and M. Alubiady, "Effect of laser parameters and assist gas on spectral response of silicon fibrous nanostructure," *Journal of Applied Physics*, vol. 108, no. 9, pp. 094327–094327, 2010.
[46] A. S. Mahmood, "Fibrous nanomaterials for enhanced light absorption and its application in photovoltaic energy conversion," Ph.D., Ryerson University, Canada, 2012.
[47] B. Tan and K. Venkatakrishnan, "Synthesis of fibrous nanoparticle aggregates by femtosecond laser ablation in air," *Optics express*, vol. 17, no. 2, pp. 1064–1069, 2009.
[48] Y.-L. Wang, W. Xu, Y. Zhou, L.-Z. Chu, and G.-S. Fu, "Influence of pulse repetition rate on the average size of silicon nanoparticles deposited by laser ablation," *Laser and Particle Beams*, vol. 25, no. 01, pp. 9–13, 2007.
[49] M. Sivayoganathan, B. Tan, and K. Venkatakrishnan, "Effect of mega-hertz repetition rate on the agglomerated particle size of femtosecond synthesized nanostructures," *Optical Materials Express*, vol. 2, no. 8, pp. 987–995, 2012.
[50] M. Sivayoganathan, B. Tan, and K. Venkatakrishnan, "Formation of ring-patterned nanoclusters by laser–plume interaction," *Journal of Nanoparticle Research*, vol. 15, no. 1, pp. 1–9, 2013.
[51] C. Samarasekera, B. Tan, and K. Venkatakrishnan, "Flower-like Na2O nanotip synthesis via femtosecond laser ablation of glass," *Nanoscale research letters*, vol. 7, no. 1, p. 404, 2012.
[52] M. Sivakumar, B. Tan, and K. Venkatakrishnan, "Synthesis of TiO2 nanoscale rods with MHz femtosecond laser irradiation of single crystal surface and characterisation," 2011.
[53] K. Venkatakrishnan, D. Vipparty, and B. Tan, "Nanofibre fabrication by femtosecond laser ablation of silica glass," *Optics express*, vol. 19, no. 17, pp. 15770–15776, 2011.
[54] M. Vitiello, S. Amoruso, C. Altucci, C. De Lisio, and X. Wang, "The emission of atoms and nanoparticles during femtosecond laser ablation of gold," *Applied surface science*, vol. 248, no. 1, pp. 163–166, 2005.
[55] G. Ausanio, S. Amoruso, A. C. Barone, R. Bruzzese, V. Iannotti, L. Lanotte, and M. Vitiello, "Production of nanoparticles of different materials by means of ultrashort laser pulses," *Applied surface science*, vol. 252, no. 13, pp. 4678–4684, 2006.
[56] S. Eliezer, N. Eliaz, E. Grossman, D. Fisher, I. Gouzman, Z. Henis, S. Pecker, Y. Horovitz, M. Fraenkel, and S. Maman, "Synthesis of nanoparticles with femtosecond laser pulses," *Physical Review B*, vol. 69, no. 14, p. 144119, 2004.
[57] Chunyi Liu, "A study of particle generation during laser ablation with applications," Doctor of Philosophy, University of Califonia, Berkeley, 2005.
[58] D. Bleiner, "Mathematical modelling of laser-induced particulate formation in direct solid microanalysis," *Spectrochimica Acta Part B: Atomic Spectroscopy*, vol. 60, no. 1, pp. 49–64, 2005.
[59] E. G. Gamaly, N. R. Madsen, A. V. Rode, and D. Golberg, "Formation of Nanoclusters in Expanding Laser Plume," *International Journal of Nanoscience*, vol. 9, no. 04, pp. 371–375, 2010.
[60] K. Kelton and A. L. Greer, *Nucleation in condensed matter: applications in materials and biology*, vol. 15. Pergamon, 2010.

[61] M. S. Tillack, D. W. Blair, and S. S. Harilal, "The effect of ionization on cluster formation in laser ablation plumes," *Nanotechnology*, vol. 15, no. 3, p. 390, 2004.
[62] W. Marine, L. Patrone, B. Luk'Yanchuk, and M. Sentis, "Strategy of nanocluster and nanostructure synthesis by conventional pulsed laser ablation," *Applied surface science*, vol. 154, pp. 345–352, 2000.
[63] V. Piñon and D. Anglos, "Optical emission studies of plasma induced by single and double femtosecond laser pulses," *Spectrochimica Acta Part B: Atomic Spectroscopy*, vol. 64, no. 10, pp. 950–960, 2009.
[64] S. H. Kim, I.-B. Sohn, and S. Jeong, "Ablation characteristics of aluminum oxide and nitride ceramics during femtosecond laser micromachining," *Applied Surface Science*, vol. 255, no. 24, pp. 9717–9720, 2009.
[65] A. Miotello and P. M. Ossi, *Laser-surface interactions for new materials production*, vol. 130. Springer, 2010.
[66] J. H. Yoo, O. V. Borisov, X. Mao, and R. E. Russo, "Existence of phase explosion during laser ablation and its effects on inductively coupled plasma-mass spectroscopy," *Analytical chemistry*, vol. 73, no. 10, pp. 2288–2293, 2001.
[67] R. Kelly and A. Miotello, "Comments on explosive mechanisms of laser sputtering," *Applied Surface Science*, vol. 96, pp. 205–215, 1996.
[68] A. Miotello and R. Kelly, "Critical assessment of thermal models for laser sputtering at high fluences," *Applied Physics Letters*, vol. 67, no. 24, pp. 3535–3537, 1995.
[69] A. Miotello and R. Kelly, "Laser-induced phase explosion: new physical problems when a condensed phase approaches the thermodynamic critical temperature," *Applied Physics A: Materials Science & Processing*, vol. 69, no. 7, pp. 67–73, 1999.
[70] R. Stoian, A. Rosenfeld, D. Ashkenasi, I. V. Hertel, N. M. Bulgakova, and E. E. B. Campbell, "Surface charging and impulsive ion ejection during ultrashort pulsed laser ablation," *Physical review letters*, vol. 88, no. 9, p. 097603, 2002.
[71] R. Stoian, D. Ashkenasi, A. Rosenfeld, and E. E. B. Campbell, "Coulomb explosion in ultrashort pulsed laser ablation of Al_2O_3" *Physical Review B*, vol. 62, no. 19, p. 13167, 2000.
[72] Z. Yan, R. Bao, Y. Huang, A. N. Caruso, S. B. Qadri, C. Z. Dinu, and D. B. Chrisey, "Excimer laser production, assembly, sintering, and fragmentation of novel fullerene-like permalloy particles in liquid," *The Journal of Physical Chemistry C*, vol. 114, no. 9, pp. 3869–3873, 2010.
[73] F. Mafuné, J. Kohno, Y. Takeda, and T. Kondow, "Dissociation and aggregation of gold nanoparticles under laser irradiation," *The Journal of Physical Chemistry B*, vol. 105, no. 38, pp. 9050–9056, 2001.
[74] M. B. Agranat, S. I. Anisimov, S. I. Ashitkov, V. V. Zhakhovskii, N. A. Inogamov, K. Nishihara, Y. V. Petrov, V. E. Fortov, and V. A. Khokhlov, "Dynamics of plume and crater formation after action of femtosecond laser pulse," *Applied surface science*, vol. 253, no. 15, pp. 6276–6282, 2007.
[75] A. S. Mahmood, M. Sivakumar, K. Venkatakrishnan, and B. Tan, "Enhancement in optical absorption of silicon fibrous nanostructure produced using femtosecond laser ablation," *Applied Physics Letters*, vol. 95, no. 3, pp. 034107–034107, 2009.
[76] A. Kiani, K. Venkatakrishnan, and B. Tan, "Micro/nano scale amorphization of silicon by femtosecond laser irradiation," *Optics Express*, vol. 17, no. 19, pp. 16518–16526, 2009.

[77] F. Brygo, C. Dutouquet, F. Le Guern, R. Oltra, A. Semerok, and J. M. Weulersse, “Laser fluence, repetition rate and pulse duration effects on paint ablation,” *Applied surface science*, vol. 252, no. 6, pp. 2131–2138, 2006.
[78] B. Tan, A. Dalili, and K. Venkatakrishnan, “High repetition rate femtosecond laser nano-machining of thin films,” *Applied Physics A: Materials Science & Processing*, vol. 95, no. 2, pp. 537–545, 2009.
[79] K. Y. Park and H. J. Jeong, “Effect of temperature on particle size for vapor-phase synthesis of Ultrafine Iron particles,” *Korean Journal of Chemical Engineering*, vol. 16, no. 1, pp. 64–68, 1999.
[80] H. Lihavainen, Y. Viisanen, and M. Kulmala, “Homogeneous nucleation of n-pentanol in a laminar flow diffusion chamber,” *The Journal of Chemical Physics*, vol. 114, p. 10031, 2001.
[81] Andres R, *In Nucleation*. New York: , 1969.
[82] Fuchs NA, Sutugin AGN, *Highly dispersed Aerosols*. London: Ann Arbor Science, 1970.
[83] C.-H. Hung, M. J. Krasnopoler, and J. L. Katz, “Condensation of a supersaturated vapor. VIII. The homogeneous nucleation of n-nonane,” *The Journal of Chemical Physics*, vol. 90, no. 3, pp. 1856–1865, 1989.
[84] G. Tani, A. Fortunato, L. Orazi, and G. Cuccolini, “Laser ablation simulation for copper,” *International Journal of Nanomanufacturing*, vol. 3, no. 3, pp. 279–294, 2009.
[85] R. J. Weber, J. J. Marti, P. H. McMurry, F. L. Eisele, D. J. Tanner, and A. Jefferson, “Measured atmospheric new particle formation rates: Implications for nucleation mechanisms,” *Chemical Engineering Communications*, vol. 151, no. 1, pp. 53–64, 1996.
[86] K. F. Kelton and A. L. Greer, “Test of classical nucleation theory in a condensed system,” *Physical Review B*, vol. 38, no. 14, p. 10089, 1988.
[87] V. Talanquer, “A new phenomenological approach to gas–liquid nucleation based on the scaling properties of the critical nucleus,” *The Journal of chemical physics*, vol. 106, p. 9957, 1997.
[88] J. Koch, A. Von Bohlen, R. Hergenröder, and K. Niemax, “Particle size distributions and compositions of aerosols produced by near-IR femto-and nanosecond laser ablation of brass,” *Journal of Analytical Atomic Spectrometry*, vol. 19, no. 2, pp. 267–272, 2004.
[89] F. Yu and R. P. Turco, “Ultrafine aerosol formation via ion-mediated nucleation,” *Geophys. Res. Lett*, vol. 27, pp. 883–886, 2000.
[90] S. Eaton, H. Zhang, P. Herman, F. Yoshino, L. Shah, J. Bovatsek, and A. Arai, “Heat accumulation effects in femtosecond laser-written waveguides with variable repetition rate,” *Optics Express*, vol. 13, no. 12, pp. 4708–4716, 2005.
[91] V. Malka, S. Fritzler, E. Lefebvre, M.-M. Aleonard, F. Burgy, J.-P. Chambaret, J.-F. Chemin, K. Krushelnick, G. Malka, and S. P. D. Mangles, “Electron acceleration by a wake field forced by an intense ultrashort laser pulse,” *Science*, vol. 298, no. 5598, pp. 1596–1600, 2002.
[92] U. Eichmann, T. Nubbemeyer, H. Rottke, and W. Sandner, “Acceleration of neutral atoms in strong short-pulse laser fields,” *Nature*, vol. 461, no. 7268, pp. 1261–1264, 2009.
[93] A. Kumar, “Ponderomotively-generated magnetic field in a relativistic gaussian amplitude modulated laser filament in an inhomogeneous plasma,” *Physica Scripta*, vol. 71, no. 2, p. 204, 2006.
[94] S. Corde and K. T. Phuoc, “Plasma wave undulator for laser-accelerated electrons,” *arXiv preprint arXiv:1104.2186*, 2011.

[95] T. Tajima and J. M. Dawson, “Laser electron accelerator,” *Physical Review Letters*, vol. 43, no. 4, pp. 267–270, 1979.
[96] H. Schwoerer, “Particle acceleration with lasers,” *South African Journal of Science*, vol. 104, no. 7–8, pp. 299–304, 2008.
[97] E. G. Gamaly, “The ponderomotive force in an overdense, absorbing, dispersive plasma, caused by an intense laser–matter interaction,” *Physics of Fluids B: Plasma Physics*, vol. 5, p. 3765, 1993.
[98] G. S. Sarkisov, V. Y. Bychenkov, V. N. Novikov, V. T. Tikhonchuk, A. Maksimchuk, S.-Y. Chen, R. Wagner, G. Mourou, and D. Umstadter, “Self-focusing, channel formation, and high-energy ion generation in interaction of an intense short laser pulse with a He jet,” *Physical Review E*, vol. 59, no. 6, p. 7042, 1999.
[99] D. Umstadter, “Relativistic laser–plasma interactions,” *Journal of Physics D: Applied Physics*, vol. 36, no. 8, p. R151, 2003.
[100] N. Kumar, S. Dash, A. K. Tyagi, and B. Raj, “Dynamics of plasma expansion in the pulsed laser material interaction,” in *Sadhana (Academy Proceedings in Engineering Sciences)*, 2010, vol. 35, pp. 493–511.
[101] H. Habara, R. Kodama, Y. Sentoku, N. Izumi, Y. Kitagawa, K. A. Tanaka, K. Mima, and T. Yamanaka, “Fast ion acceleration in ultraintense laser interactions with an overdense plasma,” *Physical Review E*, vol. 69, no. 3, p. 036407, 2004.
[102] S. S. Harilal, C. V. Bindhu, M. S. Tillack, F. Najmabadi, and A. C. Gaeris, “Internal structure and expansion dynamics of laser ablation plumes into ambient gases,” *Journal of Applied Physics*, vol. 93, no. 5, pp. 2380–2388, 2003.
[103] Y. Okano, K. Oguri, T. Nishikawa, and H. Nakano, “Observation of femtosecond-laser-induced ablation plumes of aluminum using space-and time-resolved soft x-ray absorption spectroscopy,” *Applied physics letters*, vol. 89, no. 22, pp. 221502–221502, 2006.
[104] M. O. Scully and M. S. Zubairy, “Simple laser accelerator: Optics and particle dynamics,” *Physical Review A*, vol. 44, no. 4, p. 2656, 1991.
[105] T. Wu, X. Wang, H. Lu, and P. Lu, “Debris mitigation power of various buffer gases for CO2 laser produced tin plasmas,” *Journal of Physics D: Applied Physics*, vol. 45, no. 47, p. 475203, 2012.
[106] S. Jeong, S. Wang, and Y. Cui, “Nanoscale photon management in silicon solar cells,” *Journal of Vacuum Science & Technology A: Vacuum, Surfaces, and Films*, vol. 30, no. 6, pp. 060801–060801, 2012.
[107] “Absorption and Emission Basics,” in *Introductory Nanoscience*, Garland Science, Taylor & Francis Group, 2012, p. 73.
[108] C. J. Orendorff, L. Gearheart, N. R. Jana, and C. J. Murphy, “Aspect ratio dependence on surface enhanced Raman scattering using silver and gold nanorod substrates,” *Physical Chemistry Chemical Physics*, vol. 8, no. 1, pp. 165–170, 2006.
[109] K.-S. Lee and M. A. El-Sayed, “Dependence of the enhanced optical scattering efficiency relative to that of absorption for gold metal nanorods on aspect ratio, size, end-cap shape, and medium refractive index,” *The Journal of Physical Chemistry B*, vol. 109, no. 43, pp. 20331–20338, 2005.
[110] J. Ferber and J. Luther, “Computer simulations of light scattering and absorption in dye-sensitized solar cells,” *Solar Energy Materials and Solar Cells*, vol. 54, no. 1, pp. 265–275, 1998.

[111] A. Kiani, K. Venkatakrishnan, and B. Tan, "Enhancement of the optical absorption of thin-film of amorphorized silicon for photovoltaic energy conversion," *Solar Energy*, vol. 85, no. 9, pp. 1817–1823, 2011.
[112] L. Müller-Meskamp, Y. H. Kim, T. Roch, S. Hofmann, R. Scholz, S. Eckardt, K. Leo, and A. F. Lasagni, "Efficiency enhancement of organic solar cells by fabricating periodic surface textures using direct laser interference patterning," *Advanced Materials*, 2012.

Glossaries

List of Acronyms

BBO Beta Barium borate

CCD Charge Coupled Device

DSSC Dye Sensitive Solar Cell

EDX Energy Dispersive X-ray

HWCVD Hot Wire Chemical Vapour Deposition

IR Infrared

NP Nanoparticle

RIE Reactive Ion Etching

SEM Scanning Electron Microscope

SHG Second Harmonic Generation

TEM Transmission Electron Microscope

UV Ultraviolet

XRD X-Ray Diffraction

List of Symbols

Mathematics

A Area of laser spot

A' Cross sectional area of plasma

B Magnetic field

c Speed of light

d Particle size

$\mathbf{d_1}$ Laser spot diameter

D Diameter of laser beam

e Charge on the electron

e´ Error in ring size

E Electric field

∇E Electric field gradient

Ei Mean ion energy

F Frequency of laser

FL Lorentz force

F Ponderomotive force

F´ Focal length of lens

$\mathbf{F_0}$ Focal length of scanner lens

I Laser intensity

$\mathbf{I_T}$ Transmitted light intensity

Io Incident light intensity

∇I Laser intensity gradient

$\mathbf{k_B}$ Boltzmann's constant

kv Absorption coefficient

L Thickness traversed by the light

m Electron mass

n Refraction index

T Temperature

V, $\mathbf{V_1}$ Velocity of the electron

Vp Volume of plasma

Vo Velocity of charged species

W Rate of energy deposit

Z Charge multiplicity

Greek

α Absorption coefficient

λ Wavelength

ω Laser frequency

$\boldsymbol{\varepsilon_0}$ Permeability in vacuum

τ Pulse duration

Chemical Elements and Compounds

Ag	Silver
Al	Aluminum
Au	Gold
CdS	Cadmium Sulfide
CdSe	Cadmium Selenide
Cu	Copper
GaAs	Gallium Arsenide
H	Hydrogen
MoO_3	Molybdenum Oxide
PbS	Lead Sulfide
Si	Silicon
SiO_2	Silicon Dioxide
Sn	Tin
TiO_2	Titanium Dioxide
Yb	Ytterbium
Zn	Zinc